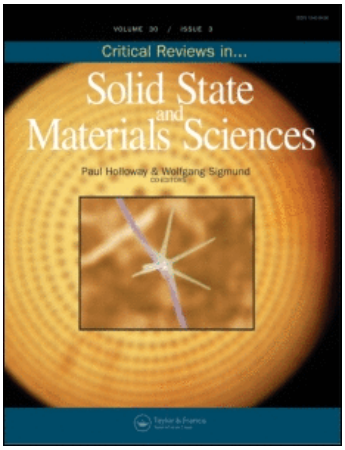


**Critical Reviews in Solid State and Materials Sciences**
Publication details, including instructions for authors and subscription information:
http://www.informaworld.com/smpp/title~content=t713610945

# One-Dimensional Group III-Nitrides: Growth, Properties, and Applications in Nanosensing and Nano-Optoelectronics

Surojit Chattopadhyay[a]; Abhijit Ganguly[b]; Kuei-Hsien Chen[bc]; Li-Chyong Chen[b]
[a] Institute of Biophotonics, National Yang Ming University, Taipei, Taiwan [b] Center for Condensed Matter Sciences, National Taiwan University, Taipei, Taiwan [c] Institute of Atomic and Molecular Sciences, Academia Sinica, Taipei, Taiwan

Online publication date: 04 December 2009

**To cite this Article** Chattopadhyay, Surojit , Ganguly, Abhijit , Chen, Kuei-Hsien and Chen, Li-Chyong(2009) 'One-Dimensional Group III-Nitrides: Growth, Properties, and Applications in Nanosensing and Nano-Optoelectronics', Critical Reviews in Solid State and Materials Sciences, 34: 3, 224 — 279
**To link to this Article: DOI:** 10.1080/10408430903352082
**URL:** http://dx.doi.org/10.1080/10408430903352082

Critical Reviews in Solid State and Materials Sciences, 34:224–279, 2009

ISSN: 1040-8436 print / 1547-6561 online
DOI: 10.1080/10408430903352082

Taylor & Francis
Taylor & Francis Group

# One-Dimensional Group III-Nitrides: Growth, Properties, and Applications in Nanosensing and Nano-Optoelectronics

**Surojit Chattopadhyay,[1,*] Abhijit Ganguly,[2] Kuei-Hsien Chen,[2,3] and Li-Chyong Chen[2,*]**

[1]*Institute of Biophotonics, National Yang Ming University, Taipei 112, Taiwan*
[2]*Center for Condensed Matter Sciences, National Taiwan University, Taipei 106, Taiwan*
[3]*Institute of Atomic and Molecular Sciences, Academia Sinica, Taipei 106, Taiwan*



**This review will give a brief introduction to the growth and characterization methods of both binary and ternary compounds, in particular those exhibiting one-dimensionality, of the family to orient the readers about the material system to be discussed. A section will deal with the size and shape selection in group III nitride nanomaterials with a stress on intriguing morphologies such as nanowires, nanotips, and nanobelts. Complex structures, such as hierarchical and core-shell structures, will be introduced. Optical, electrical, and mechanical property, such as hardness, will be discussed in a greater detail, distinguishing the bulk from the nano wherever possible. Available models of electrical conduction and photoconduction in nanomaterials and their dependence on the actual size of the objects will be presented and compared. Optical properties of ensemble and single nanostructures, wherever possible, will be addressed in detail. The section on application will focus mainly on the sensor applications, including chemical sensors, gas sensors, and biosensors, with a thrust on DNA sensing. Because popular applications such as light-emitting diodes (LEDs) and field effect transistors (FETs) have already been reviewed extensively, only major contributions to this field—for example, nano-LEDs—will be discussed. Some recent advances in the group III-nitride materials family will be presented that will indicate future directions of research in this area.**

**Keywords** GaN, AIN, InN, nanostructures, nano-sensing, nano-optoelectronics

## Table of Contents



*E-mail: sur@ym.edu.tw, chenlc@ntu.edu.tw

## 1. INTRODUCTION

Group III-nitride semiconductors have been pivotal in technology enrichment, especially in the optoelectronics field. The vast potential for this group of semiconductors is not fully realized in terms of resultant devices apart from the light-emitting diodes (LED). However, the process set into motion some 70 years ago to produce gallium nitride (GaN),[1] an important member of this class of semiconductors, is still evolving. The simple growth of GaN during 1932–1938,[1,2] by passing ammonia ($NH_3$) over hot gallium, to study its crystal structure and lattice constants was followed by its photoluminescence (PL) property[3] 20 years later. Large area growth of GaN was demonstrated another 10 years later.[4] The pace of development or understanding of the material quickened with zinc (Zn) doping producing the first blue LED in 1972.[5] The subject needed no further encouragement. Applications of the material or at least its potential were soon reported for field effect transistors (FET), bipolar transistors, phototransistors, thyristors, LEDs,[6,7] laser diodes (LD),[8] ultraviolet (UV) and X-ray detectors, memory devices, piezoelectronics, surface acoustic wave (SAW) generators, and so on. This is only a part of the story in a sense that indium nitride (InN), aluminum nitride (AlN), and boron nitride (BN) materials were also developed simultaneously, although at a different rate. Among these, AlN and BN also fall in the ceramic category and nanostructures of both have been reported. Although AlN nanostructures will be discussed in this article, the readers are referred to the literature for BN nanostructures, especially nanotubes and nanocones.[9–11]

The emergence of the materials and physics in the nanodimension also saw hectic activity involving the group III-nitride semiconductors, because the distinctive features of nanodimension lay in optoelectronics, for which the group III-nitrides are the front runners.

## 2. OBJECTIVE

Exhaustive reviews are available on different aspects of the group III-nitride materials, including their growth and properties.[12–17] Here, we will only present a brief summary of these basic aspects as background information. However, complex structures that may require some additional knowledge will be introduced. Key technical advancements related to the size and shape selection in this class of nanomaterials will be outlined with property comparison in the bulk and the nanoscale. In the applications part, although breakthrough techniques in LED and FETs will be reviewed, sensor applications will be highlighted. An exhaustive review of literature material is not intended; only the basic concepts or ideas will be introduced, with examples and illustrations as far as practicable.

## 3. SYNTHESIS OF BINARY GROUP III-NITRIDE NANOSTRUCTURES

### 3.1. Confined Chemical Reaction (Template-Based Methods)

Templates offer confined nanometer-scale space for chemical reactions. Templates, for the synthesis of nanostructures, can be categorized broadly into two groups: (1) hard and (2) soft templates. Hard templates constitute the inorganic mesoporous materials such as zeolites, anodic aluminum oxide (AAO), polymer membranes, carbon nanotubes (CNTs), and so on. Soft templates, on the other hand, include liquid crystals, surfactant assemblies, vesicles, micelles, and so on. However, most synthesis of group III-nitride materials was carried out in hard templates. GaN nanowires (NWs) were prepared using a CNT template that confines the reaction of volatile oxides within its nanodimensions.[18] A reaction of gallium oxide ($Ga_2O$) with $NH_3$ produced GaNNW with similar radial and longitudinal dimensions as that of the template, in this case, CNT, used. In the presence of CNT and at 900–1,000°C, the following reactions occurred, sequentially, to produce GaNNW:

$$Ga_2O_3(s) + 4Ga(l) \rightarrow 3Ga_2O\ (g) \quad [1]$$

$$2Ga_2O\ (g) + C\ (s) + 4NH_3\ (g) \rightarrow 4GaN\ (s) + H_2O\ (g) + CO\ (g) + 5H_2\ (g) \quad [2]$$

However, in the absence of CNT, only GaN powders were produced following the reaction

$$Ga_2O\ (g) + 2NH_3\ (g) \rightarrow 2GaN\ (s) + H_2O\ (g) + 2H_2\ (g) \quad [3]$$

This underlined the importance of the CNT template in carrying out confined reactions to synthesize desired products.

AlNNWs were similarly generated using Al and aluminum oxide ($Al_2O_3$) powders at 950–1,200°C.[19,20] The temperature required to reduce $Al_2O_3$ in the presence of Al or C via the following reactions [4] and [5],

$$Al_2O_3\ (s) + 2C\ (s) \rightarrow Al_2O\ (g) + 2CO\ (g) \quad [4]$$

$$Al_2O_3\ (s) + 4Al\ (s) \rightarrow 3Al_2O\ (g) \quad [5]$$

comes from the highly exothermic reaction [6] that produces substantial local heating to promote reactions [4] and [5].

$$2Al\ (s) + 2NH_3\ (g) \rightarrow 2AlN\ (s) + 3H_2\ (g) \quad [6]$$

Reaction [6] proceeds at 950°C. After the reduction of $Al_2O_3$ is complete, the AlNNWs can be synthesized from the following reaction:

$$2Al_2O\ (g) + C\ (s) + 4NH_3\ (g) \rightarrow 4AlN\ (s) + CO\ (g) + H_2O\ (g) + 5H_2\ (g) \quad [7]$$

The temperature required for the above reactions to occur is around 950°C, but that is considerably lower than the 1,700°C used for the production of AlN by the carbothermal reduction and nitridation methods.[21]

Another important template for this kind of nanomaterial growth is the AAO. The AAO possesses hexagonal pores or channels with nearly monodispersed dimensions of 10–200 nm as diameter and several tens of micrometers as length. This kind of AAO template is suitable for the growth of an ordered array of 1D nanomaterial. A direct reaction of metallic Ga under flowing $NH_3$ at a temperature above 900°C in the presence of the AAO template resulted in GaNNWs[22] along the channels of the AAO following the reaction:

$$2Ga\ (g) + 2NH_3\ (g) \rightarrow 2GaN\ (s) + 3H_2\ (g) \quad [8]$$

At high reaction temperatures, when the reaction rate is also high, the efficiency of the template, in general, is lost. For example, Al and $NH_3$ would react directly to form AlN fibers of larger diameters exceeding that of the template pores or channels.[23] Isolation of the product after removing the template and still maintaining the orientation alignment is not possible and that limits the use of the templates.

### 3.2. Catalyst-Assisted Growth

The metal catalyst–assisted growth is widely known as the vapor–liquid–solid (VLS) growth first proposed for the growth of whiskers by Wagner and Ellis.[24] It is basically a chemical vapor deposition (CVD) method driven in the presence of a catalyst that can accelerate the rate of a reaction, without itself taking any part in the reaction. Most semiconductor nanomaterials of the group III-nitrides class are synthesized by this technique. The basic principle is to heat a foil or powder of the group III metal such as Ga, In, or Al (source) in the presence of nitrogen ($N_2$) or $NH_3$ at temperatures suitable for vaporization of the source and dissociation of the nitriding gas. Transition metal and their oxides were found to be efficient catalysts for the precipitation of the group III-nitride material from a molten state of the catalyst droplet supersaturated with the metal vapor. The easiest form of catalyst used is a thin film of the transition metal (Fe, Ni, Co) or its oxides on the substrate used. These can be patterned by lithographic processes to obtain selected area growth of the group III-nitride material.[25] The catalyst can also be dispersed on the substrate in solution form starting with the catalytic metal nitrate or metal complexes including ferrocenes and phthalocyanines.[26] Upon reduction, these solutions will leave catalyst particles dispersed on the substrate to be used in subsequent growth of the nitride material. Because the catalytic particle size is a rough measure of the dimension of the target nanomaterial that grows, the former dictates the size distribution, specific or distributed, of the latter. The length of the 1D nanomaterial, however, depends on the reaction time and reactant flux. However, the choice of catalyst remains of utmost importance. A schematic of the VLS process is shown in Figure 1.

Although most of the CVD processes involving catalysts followed the VLS route, there are some that followed the solution–liquid–solid (SLS) path.[27,28] Notably, InNNWs and InN nanorods (NRs) were grown by this process.[29] A narrow process temperature window is available for the growth of InN

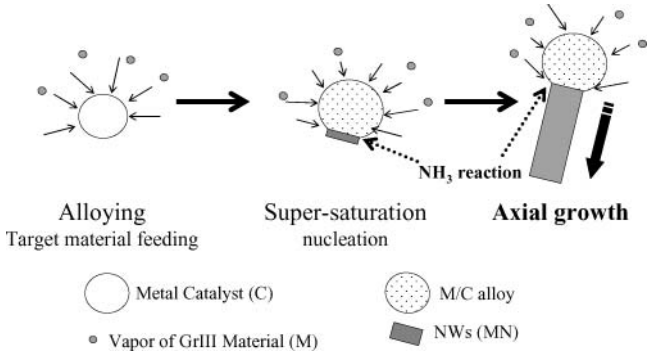


FIG. 1. A schematic representation of the vapor–liquid–solid (VLS) growth mode.

by the VLS process because the dissociation of the reactant gas and the product, InN, occur at similar temperatures. The SLS method overcomes this problem and can grow InN below 250°C. Azido-indium precursors used in this technique are $i\text{Pr}_2\text{InN}_3$ and $t\text{Bu}_2\text{InN}_3$. Thermolysis of the above precursors with 1,1-dimethylhydrazine, $\text{H}_2\text{NNMe}_2$, produced InN crystallites. Thermolysis of $i\text{Pr}_2\text{InN}_3$ in the presence of diisopropylbenzene and $\text{H}_2\text{NNMe}_2$ produced InN crystallites at 203°C. Apart from its role as a hydrogen donor, $\text{H}_2\text{NNMe}_2$, also plays an important role to generate metallic In that was found at the tip of the InN fibers. This liquid indium cluster provides the energetically favored site to aid in precursor absorption and decomposition, along with lattice reconstruction during the growth.

### 3.3. Vapor Solid Growth

When purity of products is a concern, the template or catalyst-assisted growth is often undesirable because the removal of the catalyst and template are by no means a trivial job. The vapor–solid (VS) growth can be of assistance here.[30] VS growth relies on the vapor phase transport of the precursors to the deposition zone. Adsorption, diffusion, desorption, and subsequent deposition follow, giving rise to the growth. The catalyst is no longer controlling the process or the resultant morphology of the material here, as we saw in the VLS case; instead, it is the diffusion coefficient and surface migration of the adatoms that is doing the job. The adsorption and ultimate bonding of the adatoms on the growth surface are dependent on the availability of dangling bonds on the surface. Hence, the rate of VS growth is crystalline orientation dependent. Anisotropy in growth is hence a consequence of the density of dangling bonds available at each crystalline face.

#### *3.3.1. Direct*

A nice demonstration of a direct VS growth is available for AlN nanostructures grown from Al vapors in the presence of $\text{NH}_3$.[31,32] The reaction was carried out in a horizontal tube furnace and the products were collected on metal-coated or uncoated silicon substrates. AlN nanostructures ranging from nanotips to tapered rods to perfect rods were grown only as a function of the growth temperature (Figure 2). In this case the metal catalyst could not be traced anywhere in the nanotip and the nanotips could be fabricated even without the assistance of the catalyst, indicating a VS process. The use of the metal, however, produced an enhanced and uniform morphology.

Similarly, GaNNWs and GaNNRs have been produced by the direct reaction of Ga and $\text{NH}_3$, where the growth temperature dictated the diameter of the wires.[33,34] In general, the diameters increased with increase in growth temperature and $\text{NH}_3$ flow rate.

As a special addition to this category of growth, let us discuss a new technique called the *energetic neutral atom beam lithography epitaxy* (ENABLE), which allows growing group III-nitride films at relatively low temperatures.[35] These thin films are mostly grown on single-or nanocrystalline substrates or cores. Moderate deposition conditions are often required for thin-film overcoats on nanocrystals such that the crystalline property of the substrate is not adversely affected by a high deposition temperature or pressure used. Semiconducting nitride films can be grown at <500°C without the use of organometallic precursors. A beam of neutral N atoms with tunable energies in the range of 0.5–5.0 eV (50–500 kJ/mol) is used to react with electron beam–evaporated Ga atoms at the substrate site. The N and Ga react via a nonthermal surface chemical reaction, which is a key to the process. Materials such as GaN thin films grown by this process have structural quality equivalent to those produced by metalorganic CVD (MOCVD).

#### *3.3.2. Oxide Assisted*

Unlike the hexagonal crystals of group III-nitrides obtained in the VS or VLS processes, the oxide-assisted growth produced cubic or zinc blende structures of the group III-nitride materials, such as GaN.[36] Here, laser ablation of GaN targets containing about 25 mol.% of $\text{Ga}_2\text{O}_3$ at 1,000°C produced GaNNWs, whereas pure GaN targets did not yield the NWs. The growth of the GaNNWs is believed to obey the following pathway: (1) decomposition of GaN into constituent atoms by the high-energy laser impact, (2) released Ga reacting with $\text{Ga}_2\text{O}_3$ in the target to produce $\text{Ga}_2\text{O}$, (3) $\text{Ga}_2\text{O}$ vapors and N are transported to the growth zone by the carrier gas, (4) $\text{Ga}_2\text{O}$ and N react in the following manner to produce GaN:

$$3\text{Ga}_2\text{O} + 4\text{N} \rightarrow 4\text{GaN} + \text{Ga}_2\text{O}_3 \qquad [9]$$

Large-scale synthesis of InNNWs was demonstrated using a thermal CVD of In metal and $\text{In}_2\text{O}_3$ powders under flowing $\text{NH}_3$ at 700°C.[37] The pathway to achieve the InNNWs is similar to that in the case of GaNNWs. Here, molten In reacting with $\text{In}_2\text{O}_3$ produces $\text{In}_2\text{O}$ vapors, which then reacts with $\text{NH}_3$ to deposit the solid InNNWs on the substrate following

$$\text{In}_2\text{O(g)} + 2\text{NH}_3\text{(g)} \rightarrow 2\text{InN(s)} + \text{H}_2\text{O(g)} + 2\text{H}_2\text{(g)} \qquad [10]$$

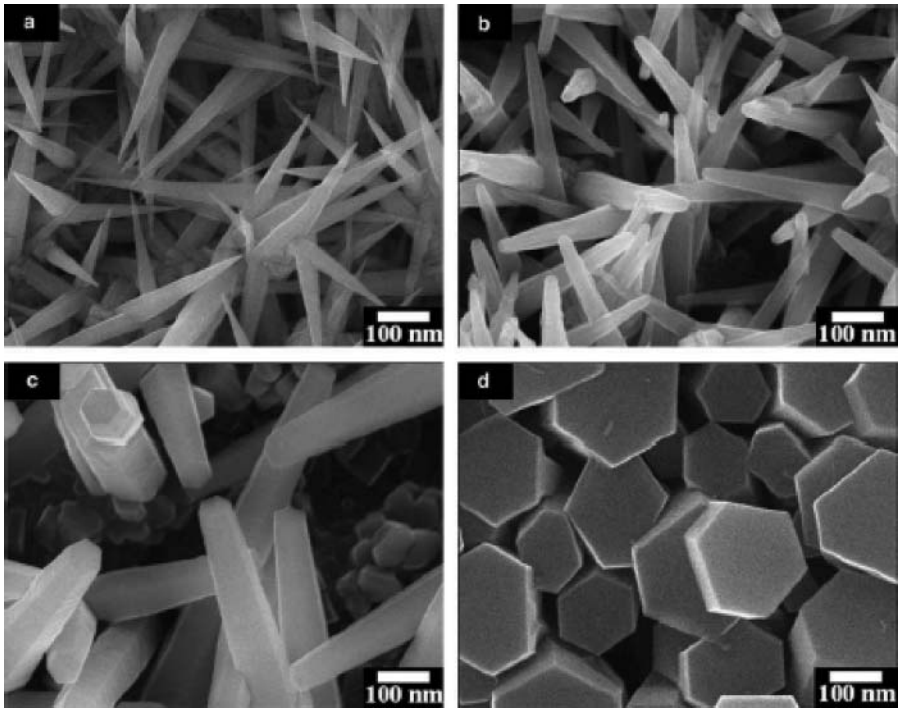


FIG. 2. Scanning electron micrographs (SEM) showing morphology evolution of AlN nanostructures grown by thermal CVD at different growth temperatures: (a) nanotips at 950°C, (b) truncated nanotips at 1,000°C, (c) tapered nanorods at 1,100°C, and (d) perfect nanorods at 1,200°C. (Reprinted with permission from Shi et al.[32] Copyright 2006 Elsevier.)



*3.3.3. Chloride Assisted*

The presence of a chloride salt of a group III metal can accelerate reactions leading to nanoparticle or NWs of the metal nitride under suitable conditions. For example, nanocrystalline Al metal reacting with $N_2$ at 1,000–1,100°C will produce AlNNWs or equiaxed AlN nanoparticles (NPs).[38,39] However, the presence of $AlCl_3$ promotes the growth of AlNNWs instead of the AlNNPs. The yield of AlNNWs increased from 50 to 90% as the $AlCl_3$ was increased from 10 to 90 wt.% in the reaction. Relatively long NWs (>30 $\mu$m) with small diameters (20–100 nm) resulted from this process. The nonreactive $AlCl_3$ is believed to be the source for reactive AlCl(g) and $AlCl_2$(g), which reacts with the N-species forming the AlN at the high reaction temperatures. This suggests that although the AlN equiaxed NPs grew from a liquid-phase Al, the AlNNWs grew from Al vapors where $AlCl_3$ acts as the vapor transport agent and supplier of the volatile mono- and dichlorides. Rapid heating was, however, necessary to dissociate $AlCl_3$ before nitridation actually occurred.

*3.3.4. Combustion*

This process relies on the uniform heating of the reactants to their ignition temperature, triggering simultaneous reaction throughout the zone. Micrometer-size Al powders reacting with AlN diluent and 3 wt.% of $MgCl_2$ powder, as the vapor transport agent, produced AlNNWs with large diameters, >100 nm, and extraordinarily long length of ~2 mm.[40,41] Submicrometer-size Al powders with ammonium fluoride and ammonium chloride ($NH_4Cl$, 26 mol.%) as the solid $N_2$ source and diluent also produced AlNNWs. In the latter case, ammonium halides broke down to $NH_3$ and HX (X = Cl or F) at ~400°C.[41] These components reacting with Al form intermediate products and finally AlN(s), HX, and $NH_3$.

*3.3.5. Sublimation*

GaN powders obtained from gaseous reactions constitute the starting material for the production of GaNNRs through the sublimation process.[42] These powders were ball-milled with hardened agate balls for 18 h to result in 60–200 nm spherical particles of GaN. Heating these particles at 930°C for several hours under flowing $NH_3$ resulted in GaNNRs with diameters of 10–45 nm. The milling process was indispensable for the GaNNR growth. The particle surface was rendered unstable, allowing sublimation at high temperatures, and subsequent condensation into NRs.

### 3.4. Reactive Ion Etching

Reactive ion etching (RIE) provides a classic example of the top-down approach for the formation of nanostructures. Here, micrometer thick films grown on suitable substrates form the

starting material to be etched. Yu et al. produced GaNNRs of controllable diameters and densities using inductively coupled plasma RIE (ICP-RIE) on MOCVD-produced GaN epi-film on sapphire (001) substrates.[43] The ICP is composed of Ar and Cl in the flow ratio of 5:2. The etching is crucially dependent on the chamber pressure and could result in GaNNRs only at pressures exceeding ~3 mTorr. GaNNRs density increased and diameters decreased as the chamber pressure was increased. Typically, for an etching time of 2 min, the NR density increased from $10^8$ to $3 \times 10^{10}$ $cm^{-2}$ and the diameter decreased from 100 to <50 nm as the pressure was increased from 10 to 30 mTorr. However, the density and diameter of the NRs depend heavily on the ease of etching of the starting material, which again is a function of the quality of the starting material. In other words, the starting film may have a large density of defects, such as dislocations, to the tune of $10^8$ to $10^9$ $cm^{-2}$, which favors the Ga-N bond dissociation and production of nearly defect-free NRs of similar densities.

## 4. SIZE, SHAPE, AND ORIENTATION CONTROL OF GROUP III-NITRIDE NANOMATERIALS

With the basic information on growth mechanism and defect information in place, we may discuss the size and shape control in 1D nanomaterials. As discussed, the VLS process forms one of the major growth modes of 1D nanomaterial where a catalyst is chosen such that (1) it is in the liquid phase at the growth temperature and (2) it does not form a solid solution with the nanostructure being precipitated out. This metal droplet serves as the preferential site for gas-phase precursor adsorption. In the VLS growth mode one can control the size of the 1D nanostructure by (1) catalyst particle size, (2) flux of reactants, (3) reaction time, and (4) precursor source. Although the catalyst particle size cannot be used to predict the specific diameters of the VLS grown 1D nanostructure, a trend can be predicted. For example, GaNNWs grown on gold (Au) NPs of different sizes clearly show an increase in GaNNW diameter as the AuNP size is increased.[44] However, instances where the catalyst particle size can be either smaller or bigger than the resulting diameters of the 1D nanostructure do exist. But a larger catalyst particle will usually produce a larger diameter nanostructure. The control of catalyst particle size and their distribution is essential for the size distribution of the nanostructures (Figure 3). The process temperatures for nanostructure preparation are generally high, which allows for considerable self- and surface diffusion. This may result in severe agglomeration of the catalyst particles during the heating process. Introduction of a diffusion barrier material with the catalyst will prevent such agglomerations. Pursuing such ideas, GaNNWs were prepared from Co, Ni, Fe catalysts using $TiO_2$ as a diffusion barrier matrix.[45] Similarly, $Fe_2O_3$ catalysts supported on $Al_2O_3$ matrix were used to produce GaNNW.[46] The presence of $SiO_2$ was believed to reduce the melting of the $Fe_2O_3$ catalyst and aid the reaction between Ga and $NH_3$.[46] The presence of $Al_2O_3$ led to the reduction of the diameter of the GaNNWs to 10–50 nm compared

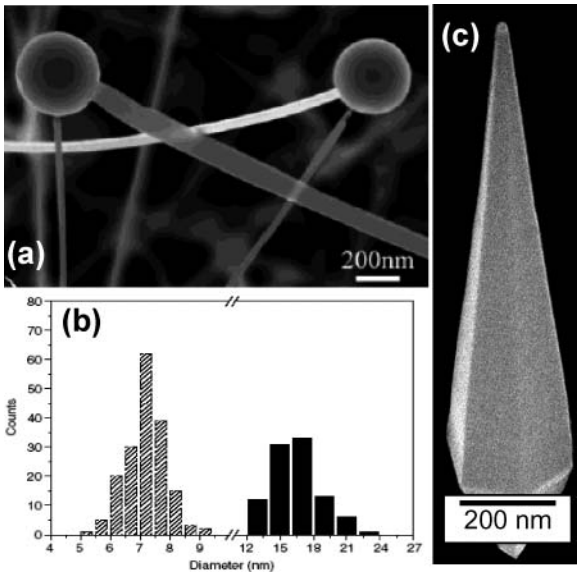


FIG. 3. SEM image of nanostructures with catalyst particles at the end: (a) ZnO nanowire and nanobelt of different size sharing the same Sn catalyst particle. (Reprinted with permission from Ding et al.[49] Copyright 2004 American Chemical Society.) (b) Diameter distribution of GaN nanowire (black bars) growing on gold nanoparticles (hatched bars). (Reprinted with permission from Kuo et al.[44] Copyright 2006 Institute of Physics.) (c) InN nanotip with a catalyst at the tip. (Reprinted with permission from Shi et al.[53] Copyright 2005 American Institute of Physics.)

to 80–200 nm using $Fe_2O_3$ alone. The catalyst preparation is an elaborate affair and can affect the size of the nanostructure dramatically.

The diameters of the 1D nanostructures were strong functions of the reactant flux.[26] NWs synthesized by the thermal CVD technique using a horizontal quartz tube in a furnace showed smaller size NW when the separation between the metal (Ga, Al, In) source and the substrate increased. In this technique the Ga metal source is kept in a boat upstream and the catalyst-coated substrate in another boat downstream, with respect to the flow of $NH_3$. The diameters of the GaNNWs were 50–150 nm when the boats were 1 cm apart and then reduced to 20–50 nm when they were 10 cm apart. The reduction of the NW diameter with increasing separation between the boats was probably due to the depletion of reactants at the catalyst site as a result of poor vapor transport in the tube.

The effect of the total reaction time was also seen to influence the 1D nanomaterial size.[26] Other deposition conditions being the same, the variation of only the deposition or reaction time can modify the morphology of the GaNNW prepared by the thermal CVD technique. At a low reaction time <3 h, short GaNNRs with diameters of several hundred nanometers were produced, which increased in length and decreased in diameter to produce GaNNW as the time increased to 3–12 h. Over this reaction time GaN bulk crystals were observed.

The observation of NW diameter reduction due to a depletion of reactants[26] at the catalyst site indicates the usefulness of gaseous or liquid precursors instead of a solid inorganic one as used in the work.[47] Ga metal having a low vapor pressure of $\sim 10^{-4}$ Torr at 900°C can be substituted with an organic source such as Ga dimethylamide ($Ga_2[N(CH_3)_2]_6$)[47] or Ga acatylacetonate (($(CH_3COCHCOCH_3)_3Ga$)[48] for the formation of GaNNWs. In the latter case GaNNWs can be grown at a lower temperature of 620°C because Ga acetylacetonate decomposes at a lower temperature of 196°C. GaNNWs of 15- to 60-nm diameters and lengths of several tens of micrometers can be formed.

The shape control of 1D nanostructures, in general, is more complicated and intriguing. Which morphology among wire, tube, tip, or belt is selected during a growth process remains a question, the answer to which may lie in the energetics of the process. Opposed to the popular belief that the catalyst being in liquid state does not influence the NW crystalline structure, Y, Ding et al.[49] showed in a model ZnO system that it does. Although the local temperature may exceed the melting point of bulk tin, a region of order or partial crystallinity exists at the interface of the tin catalyst and the growing ZnONW. The crystallographic orientation of the growing NW will select the least lattice mismatch structure between itself and what exists at the interface to grow. A single tin particle can produce ZnONWs and nanobelts (NBs) of different sizes (Figure 3) and growing along [0002] for the former and [01$\bar{1}$0] and [2$\bar{1}\bar{1}$0] for the latter. The NWs and NBs have different crystalline orientation relationships with the tin particle. The crystalline orientation of the tin particle may select the growth direction of the NWs and NBs depending on the least lattice mismatch. The completeness of this argument is debatable and may or may not extend to the group III-nitrides case. This is because the difference in orientation selectivity may have something to do with the minimization of surface energy. For instance, the close-packed planes (002) might be the preferred belt surface for the case of NBs. Lattice mismatch is a major factor for epitaxial films where a large area of interface is concerned. Even so, there is some tolerance of accommodating a mismatched interface. For NWs and NBs, the interface between the catalyst and wire/belt is relatively small. The interfacial energy is probably negligible in comparison to the surface energy of NWs/NBs.

Single-crystalline InNNBs were reported on Au-coated silicon substrates by using a guided-stream thermal CVD process at a temperature of 560°C (Figure 4).[50] The $NH_3$ gas was delivered in the reaction zone by a separate coaxial quartz tube that opened at the substrate held at the center of the outer quartz tube (Figure 5). This variation of the conventional thermal CVD was responsible for the NB formation, without which it produced InNNWs and InNNRs.[51] This again proves that the reactant flux and temperature gradient along the growth zone can help select the shape of the nanostructure produced. However, the production of the NBs is again governed by energetics of the

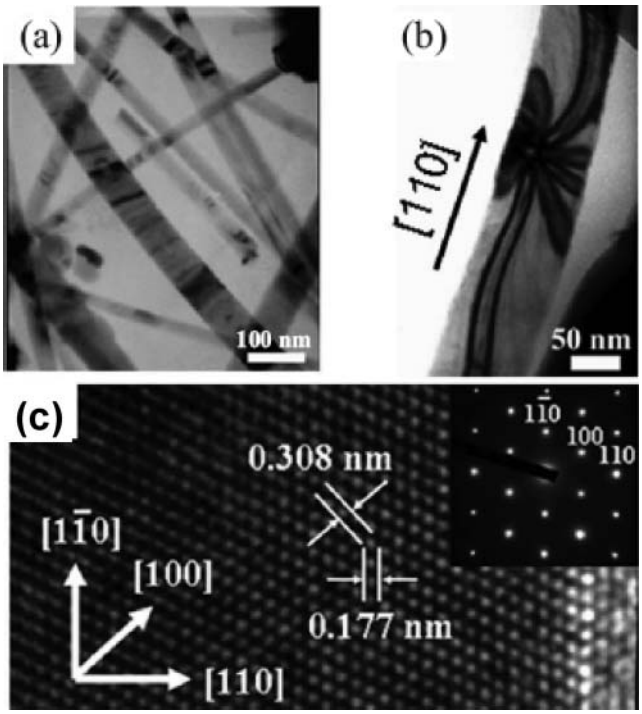


FIG. 4. (a) and (b) Low-magnification TEM images of InN nanobelts. (c) High-resolution TEM image of the InN nanobelt growing along [110] and corresponding SAED pattern. (Reprinted with permission from Hu et al.[50] Copyright 2006 Wiley-VCH Verlag GmbH & CoKG.)

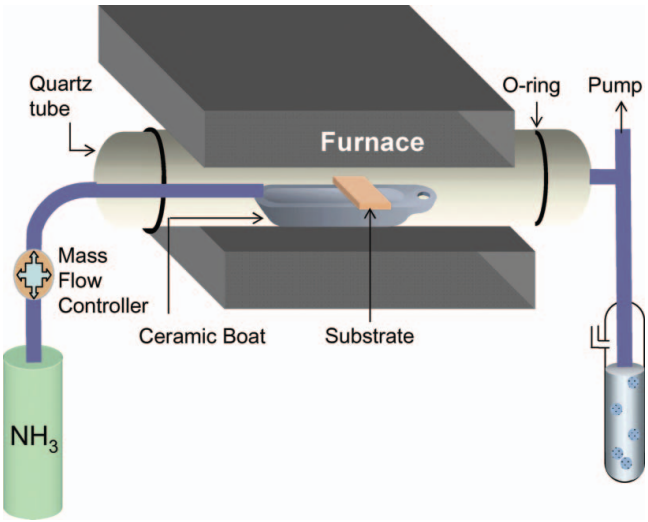


FIG. 5. Schematic diagram of the guided stream thermal chemical vapor deposition (GSTCVD) system showing a modified delivery of the $NH_3$ right over the source metal position. Conventional TCVD systems have the $NH_3$ delivered at the entrance of the quartz tube.

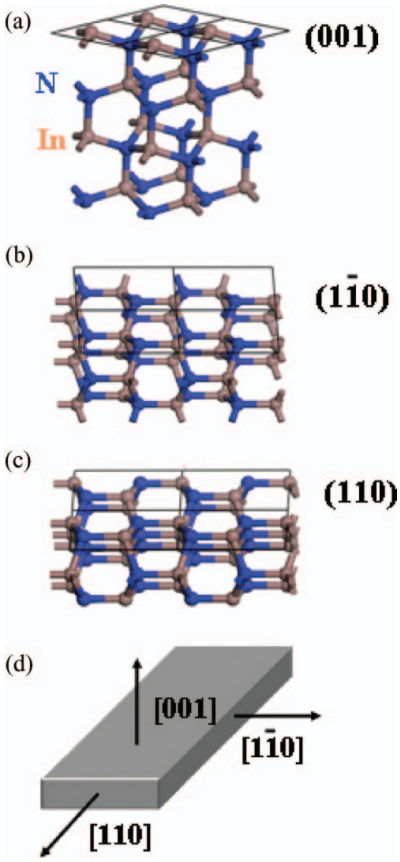


FIG. 6. Unit cell model of h-InN constructed using CERIUS2 software: (a) (001), (b) (1$\bar{1}$0), and (c) (110). (d) Schematic diagram of the nanobelt crystallographic directions. (Reprinted with permission from Hu et al.[50] Copyright 2006 Wiley-VCH Verlag GmbH & CoKG.)

process as discussed previously for the tin-ZnO NBs system. In this case, the growth direction and the enclosing facets of the belts are [110], ±(001), and ±(1$\bar{1}$0), respectively. This can be explained in terms of surface energy ($\gamma$) and growth kinetics.[52] Unit cells of InN along [110], [001], and [1$\bar{1}$0] were constructed using the CERIUS2 software package (Accelrys Software Inc., CA, USA) where the cleaved planes correspond to the structure of the NB as shown (Figure 6). The number of broken bonds per unit cell along the three directions is 4, 1, and 2, respectively, indicating number of broken bonds per unit area on the crystal plane to be 1.14 nm$^{-2}$ for (110), 0.92 nm$^{-2}$ for (001), and 0.99 nm$^{-2}$ for (1$\bar{1}$0). This indicates that $\gamma_{(001)} < \gamma_{(1\bar{1}0)} < \gamma_{(110)}$ and that (110) have the highest growth rate followed by (1$\bar{1}$0) and (001), the latter two forming the width and thickness of the belt.

InN nanotips (NTs) were reported by the MOCVD process[53,54] that grew on Au-coated quartz substrates via the VLS route by the reaction of tri-methyl indium (TMIn) and $NH_3$ at a temperature of 550°C. Analogous to the radius that characterizes a wire or tube, the apex angle characterizes a tip. For InNNTs a distribution of apex angles was observed. Apex angles as low as 3 degrees and as high as 54 degrees were observed (Figure 7) with a frequency distribution as shown in Figure 8.[54]

Interestingly, AlNNTs grown by thermal CVD by a VS process using Al powders and $NH_3$ at a temperature of 950°C only exhibited an apex angle of 18 degrees and showed no distribution.[31,54] The AlNNTs were ~1 $\mu$m in length and 200 nm in base diameters. It is not clear at this moment whether the growth process was responsible for the marked distinction in the dispersion of the apex angles in AlNNTs and InNNTs. Upon close inspection of the AlNNTs by electron microscopy it was observed that the slant surface of the NT is not continuous but actually stepped in nature (Figure 9).[54] That is, hexagonal platelets of AlN of diminishing size were stacked on top of each other (Figures 9a, 9b) as growth proceeded along the [002] direction.[32]

The hexagonal close-packed structures have the highest number of dangling bonds on the metal polarity surface, either [001] or [00$\bar{1}$] direction, so the growth rate is highest along that direction. The lateral growth in the AlNNTs, which are orthogonal to the above directions, is comparatively prohibited. This is more so at temperatures of 950°C, because it was observed that for AlN that increasing the growth temperature destroyed the tip shape and NRs were produced at 1200°C. There was a systematic variation in the shape of the AlN nanostructure as the growth temperature increased from 950°C. As the growth temperature was increased (1,000°C), the stepped nature of the slant surface was smoothed out and some rounding of the apex was observed. With further increase in the growth temperature, tapered NRs were observed instead of NTs. The hexagonal cross section was still maintained, but the morphology resembled a shape as if the tip has been truncated and the stepped nature fully smoothed out. At 1,200°C, perfect AlNNRs with hexagonal cross section were observed (Figure 10).

This is believed to be a diffusion-limited process because of the observed temperature activation. Diffusion of the impinging precursors as a function of temperature is the key to the morphology evolution.[32] The increase in growth temperature also saw thickening of the nanostructures perpendicular to the growth direction, whereby the NTs and NRs are the smallest and the widest at the base, respectively. This is expected because the diffusion length of the precursors on the growing surface is higher at higher temperatures. The VS growth in this case is a layer-by-layer growth, with growth islands demarcated significantly from each other along the growth direction at lower temperatures creating the stepped morphology. The impinging precursors did not have sufficient energy at lower temperatures to move down a step to the lower island due to the presence of the Ehrlich-Schoebel (ES) barrier[55,56] present at the edges. The smoothening of the stepped nature occured at higher temperatures when the impinging precursors overcame the ES barrier to contribute to the growth in a direction perpendicular to the axis. In short, the ES barrier restricted the lateral growth at low temperatures and produced thin NTs, whereas at higher

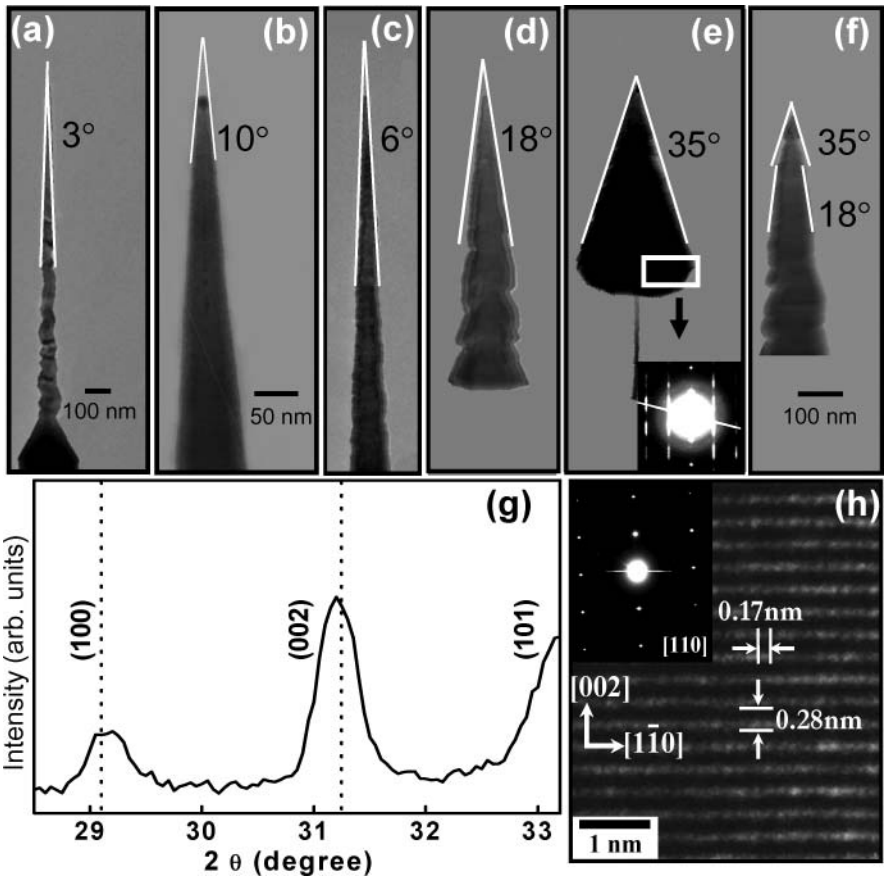


FIG. 7. (a)–(f) TEM of InN nanotips showing different apex angles; inset in (e) shows the electron diffraction of the marked area in (e); same scale bar for (c)–(f) shown in (f); (g) XRD pattern of the nanotips with the dotted lines marking the bulk InN position for reference; (h) HRTEM image of the narrow apex angle InN nanotip, with inset showing the diffraction pattern. (Reprinted with permission from Chattopadhyay et al.[54] Copyright 2006 American Institute of Physics.)



temperatures the lateral growth was promoted, giving thicker NRs. This is a very good example of shape selection by growth temperature only in a VS process.

The apex angle determination was achieved by the platelet stacking model. A step height ($h$) and step spacing ($\lambda$) were defined from the microscopic evidence of the AlNNTs (Figure 9c). Both the step height and spacing must be some integer multiples of the lattice spacing along the axial growth direction [002] and the lateral direction of [1$\bar{1}$0]. The apex angle, $\varphi$, is then defined as

$$\tan\left(\frac{\varphi}{2}\right) = \frac{\lambda}{h} = \frac{n_1 \times d_{(1\bar{1}0)}}{n_2 \times d_{(001)}} = \frac{n_1}{n_2} \times D \qquad [11]$$

where $d_{(hkl)}$ represents the interplanar spacings. For a particular material the ratio of the interplanar spacing is a constant $D$. Hence, the $\varphi$ of an NT of that material is only a function of the $n_1/n_2$ ratio. For AlNNTs, this ratio was found to be 0.2857, which generated $\varphi \sim 18$ degrees. For AlNNTs, $h$ exhibited a distribution but $\lambda$ only had values of 1 or 2 lattice units (Figure 9d). Following this platelet stacking formulation, a set of $\varphi$ could be generated for the InNNTs described above. Each $\varphi$ calculated using Equation [11] matches the experimental result shown in Figure 8. The rationale behind the generation of particular slant surfaces that defined the tip is again minimization of the surface energy. It has been shown in AlN that the slant surfaces are actually non-growth surfaces having a mimimum number of dangling bonds, unlike the growth plane along the axial direction of the NT.[31] Atomic arrangements in an AlN crystal showing the nongrowth stable surfaces of (221), (1$\bar{1}$1), and (1$\bar{1}$2), making angles of 9, 29, and 47 degrees, respectively, with the $c$-direction of [0001] are depicted in Figure 11.

Orientation control in one-dimensional nanostructures is a challenging issue. Growth of epitaxial III-N films, which might assist in orientation control of NWs or NRs, were difficult due to lack of lattice matched substrates. However, sapphire (001) substrates were used for the growth of GaN (001). On one of these substrates, oriented GaNNRs were produced.[57] GaN thin film grown on sapphire substrates was patterned with a 5 $\mu$m $\times$ 5 $\mu$m nickel square mesh. A chlorine and Ar plasma was used to etch the exposed GaN in an inductively coupled plasma

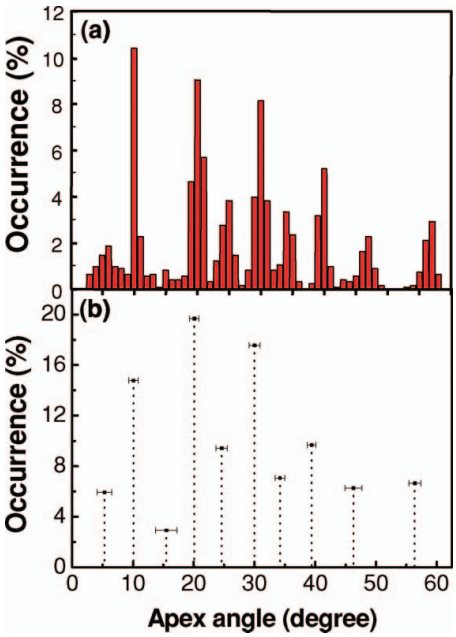


FIG. 8. (a) Histogram of occurrence (%) of InN nanotips with different apex angles; (b) averaged distribution centered at observed peaks in apex angles shown in (a). (Reprinted with permission from Chattopadhyay et al.[54] Copyright 2006 American Institute of Physics.)

system for 10 min. The residual nickel was removed by a mixture of nitric and hydrochloric acid (1:3 volume ratio), thus leaving square trenches of the GaN (001) on the sapphire substrates. A coating of Au (catalyst) was deposited on this to assist in the VLS growth of NWs at 850°C for 3 h. Interestingly, GaNNRs grew perpendicular to the sidewalls of the GaN film and parallel to the substrate as if to bridge the trenches between the square posts on which Ni was deposited. Sometimes, two parallel sets of GaNNRs grew from the sidewalls of the GaN film, which is along [100], making an angle of 60 degrees between them. These two sets of GaNNRs grew along [100] and [$1\bar{1}0$]. These directions are equivalent for the hexagonal symmetry and include an angle of 60 degrees between them. An epitaxial relationship between the substrate and the GaNNRs was evident from the directionality of the growth.

Kuykendall et al.[58] gave a nice demonstration of the substrate's crystalline orientation controlling the growth direction of the GaNNWs growing on them. They used (100) $\gamma$-$LiAlO_2$ and (111) MgO substrates to grow GaNNWs by a metal-initiated MOCVD process using tri-methyl gallium (TMGa) and $NH_3$ as the Ga and $N_2$ source, respectively. The logic behind the critical selection of the $LiAlO_2$ and MgO substrates lay essentially in both the symmetry and lattice match with that of the material to be grown, in this case GaN. The oxygen sublattice in the (100) plane of $\gamma$–$LiAlO_2$ has a twofold symmetry matching with the (100) plane of $h$-GaN. The lattice constants $a = 5.17$ Å and $c = 6.28$ Å of $\gamma$-$LiAlO_2$ match closely with the lattice constants $c = 5.19$ Å and $2a = 6.38$ Å of GaN, respectively. Again, the threefold symmetry of the (111) MgO and its 2.98 Å interatomic spacing matches with the threefold symmetry of (001) plane of GaN and the $a = 3.19$ Å lattice constant. Indeed, the growth directions of the GaNNWs were found to be [$1\bar{1}0$] and [001] on the (100) $\gamma$-$LiAlO_2$ (Figures 12a, 12c) and (111) MgO (Figures 12b, 12d) substrates, respectively. The X-ray diffraction (XRD) data (Figures 12e, 12f) clearly show the preferred orientation of the GaNNWs grown on $\gamma$-$LiAlO_2$ and MgO with peaks for the (100) and (002) planes, which corresponds to the orthogonal [$1\bar{1}0$] and (002) growth directions, respectively.

## 5. HIERARCHICAL, CORE-SHELL, AND COMPLEX NANOSTRUCTURES

Hierarchical nanostructures are simply a sequential multistage growth of nanostructures, one following the other. Complex assemblies of nanomaterials can be achieved using this strategy. Oxide-based systems, particularly ZnO, have demonstrated two-, four-, and eightfold symmetric hierarchical structures.[59] This category of nanostructures is an ideal system for the demonstration of homo- and heterojunctions that carries tremendous device potential. Fabrication of such homo- and heterojunctions in the GaN system has been reported.[60] Here, nanoribbons of $Ga_2O_3$ were first fabricated using Ni catalyst on an Si substrate in a CVD system. Evaporated Ga reacted with water vapors brought about by passing Ar through water in a horizontal tube reactor held at 950°C for 2 h. The $Ga_2O_3$ nanoribbons formed on the Si substrate were heated in a horizontal quartz tube held inside a furnace at 950°C for 3 h under a 10 sccm flow of $NH_3$. The white $Ga_2O_3$ nanoribbons were reduced to yellowish GaNNWs. For the homojunctions, GaNNRs were fabricated on the GaNNWs. The starting GaNNWs were coated with a thin layer (~5 nm) of Au by ion beam sputtering deposition for a further catalytic CVD process. These Au-coated GaNNWs on the Si substrate were then loaded inside the horizontal reactor, which carried at its center the molten Ga as the source precursor. The temperature inside the reactor was ramped up to 850°C under flowing $NH_3$ and kept for 3 h. Branches of GaNNRs were formed on the starting GaNNWs, yielding a brush-like structure with two- and fourfold symmetries (Figure 13a). Three (4S, 4M, and 4M*[1]; Figures 13b–13d) and one (2S) subsymmetry (Figure 13e) were observed for the fourfold and twofold major symmetry, respectively.

For the heterojunctions, InNNRs were grown on the starting GaNNWs. Here, the Au-coated GaNNWs on Si substrate were put on the BN heater held inside a vertical tube reactor that did not have a furnace. This is basically an MOCVD system with tri-methyl indium (TMI) being the indium precursor carried by 1 sccm of pure $N_2$ gas. Another 200 sccm of $N_2$ was introduced for efficient flow. Another 1,000 sccm of $NH_3$ was then mixed with TMI and introduced on the substrate held at 500°C. Again, brush-like InNNWs were formed on the GaNNWs (Figure 13g).

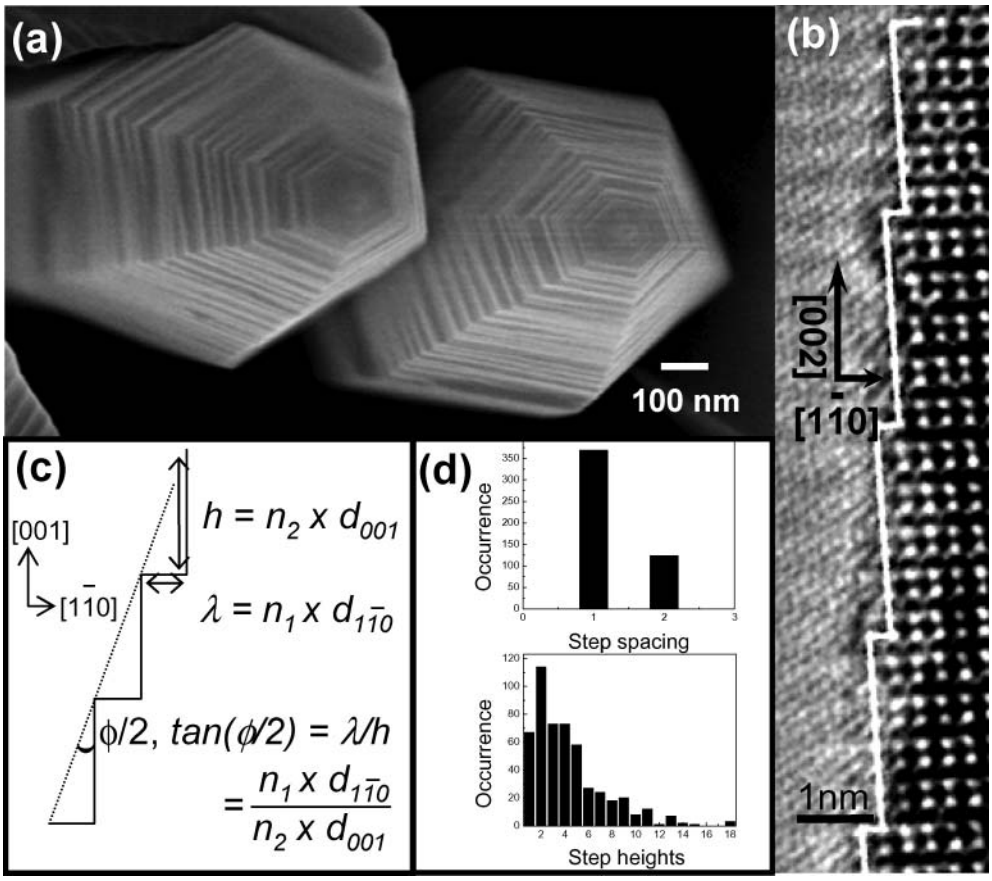


FIG. 9. (a) Top-view SEM image of AlNNTs showing the hexagonal platelet stacking; (b) HRTEM image of the surface of the nanotip depicting the stepped edge morphology; (c) schematic of the platelet stacking model; (d) distribution of step spacing (top) and step heights (bottom) in units of $d_{[1\bar{1}0]}$ and $d_{[001]}$, respectively. (Reprinted with permission from Chattopadhyay et al.[54] Copyright 2006 American Institute of Physics.)

Hierarchical structures involving InNNWs on InNNBs can also be formed. The growth strategy is a similar two-stage process. First, the InNNBs were formed on Si substrates by an Au-catalyzed CVD process in an MOCVD reactor at 540°C. Next, these InNNBs were coated with Au again for further growth of the InNNW again at 540°C. Brush-like structures were formed on the parent InNNBs (Figure 13f).

Another member of the complex morphological group is the core-shell structure. Here, a shell of a certain material is growing on another material that constitutes the core. Generally, systems with contrasting bandgaps form a nice material to study optical properties. The property of the whole core-shell structure varies depending on the nature of each layer but is predominantly dictated by the shell if it is thick. In other cases, a thin shell is used to passivate the surface and consequently enhance the optical property of the thick core.

Core-shell structures of GaN and GaP demonstrate a system with contrasting bandgaps of 3.39 eV for the former and 2.3 eV for the latter. GaN and GaP also have contrasting bandgap natures, direct and indirect, respectively. Core-shell nanostructures have been reported with both $h-$GaN and cubic GaP serving as the core and shell.[61] GaN@GaPNWs, where GaP is the shell, were prepared by the thermal CVD technique discussed previously in Section 3.3.1 and detailed later in Section 7. Here, GaNNWs were prepared on an Si substrate from the reaction of Ga and $NH_3$ at 950°C in the presence of iron phthalocyanine. The substrate with the GaNNWs was then transferred to another horizontal reactor carrying a boat with Ga, $Ga_2O_3$, and red phosphor. The temperature in the reaction zone was raised to 1,000°C for 30 min under flowing Ar gas to obtain the GaP shell (Figure 14a). Similarly, for the fabrication of GaP@GaN core-shell structure, the GaPNWs were first fabricated from the reaction of molten Ga, red phosphor, and iron phthalocyanine at 1,000°C for 30 min. Then the GaPNWs were introduced in another reactor containing Ga and $Ga_2O_3$ and heated to 950°C for 3 h under flowing $NH_3$. This resulted in the GaN shell (Figure 14b). The temperature and time of reaction are crucial for the formation of the shell. Typically, the shell is around 4–20 nm in thickness, whereas the core is around 10–100 nm in diameter. High resolution transmission electron microscope (HRTEM)

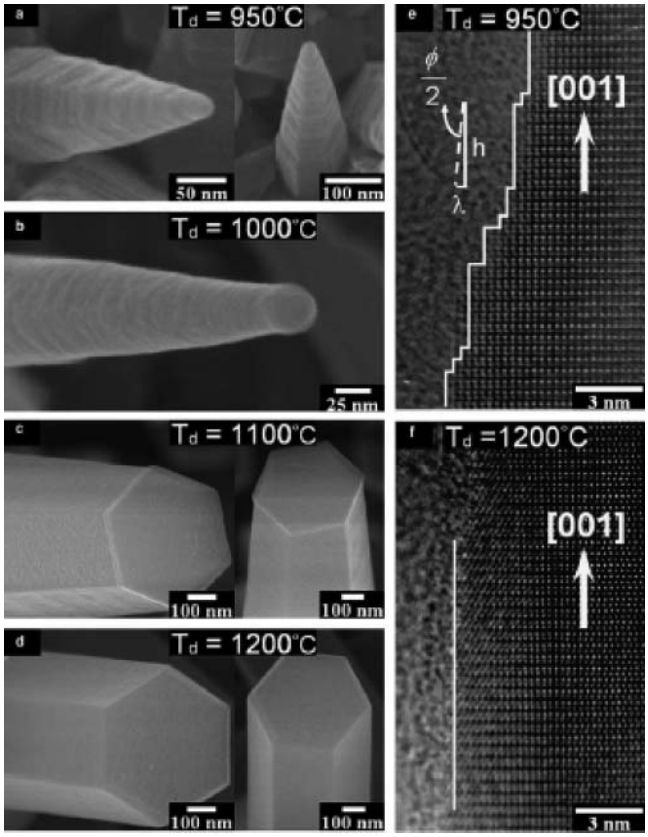


FIG. 10. (a)–(d) HRSEM images of AlN nanostructures produced at different growth temperatures; (e) HRTEM image of the edge of the AlN nanotip showing the step edges, including the step heights ($h$) and step spacing ($\lambda$); a schematic aiding in the semi-apex angle ($\phi/2$) is also shown; (f) HRTEM image of the edge of the AlN nanorod showing uniform diameter without the tapering and step edges as in (e). (Reprinted with permission from Shi et al.[32] Copyright 2006 Elsevier.)

studies reveal a misfit dislocation loop at the interface of the core and shell (Figure 14b).

Other complex NW structures, such as the barcode ones, were also fabricated to study the photon confinement effects. These NWs are made of alternating materials, say InAs and InP,[62] of controlled thicknesses that resembles the barcode for identifying customer commodities. Such structures have also been obtained in the group III-nitride system.[63] GaN quantum discs embedded in aluminum gallium nitride (AlGaN) nanocolumns with good crystalline quality and high luminescence efficiency were self-organized on AlN-buffered silicon (111) substrates by plasma-assisted Molecular Beam Epitaxy (MBE) (PAMBE) under nitrogen-rich conditions (Figure 15a). The $N_2$-rich environments were required to reduce Ga mobility on the substrate and nucleate the nanocolumn growth. The growth temperature was 760°C. The 2- and 4-nm-thick GaN quantum discs were incorporated in the AlGaN nanocolumn, with AlGaN spacer thickness of ~10 nm, by simply shutting of the Al flux for different lengths of time during the growth of the AlGaN nanocolumn.[63] The AlGaN nanocolumns were 30–150 nm in diameter. The corresponding PL spectrum of the GaN quantum disc embedded AlGaN nanocolumn is shown in Figure 15b. The PL spectrum clearly shows three peaks at 3.5, 3.62, and 3.81 eV (Figure 15b). The strong 3.81 eV PL peak originates from the matrix of the AlGaN nanocolumn and the Al content has been estimated to be $20 \pm 1\%$ from the PL peak position. The emission at 3.62 and 3.51 eV was attributed to two confined hole states of GaN quantum dots (QD). The emission energies could be tuned and show a blue shift with decreasing quantum disc thickness. However, at low disc thicknesses (e.g., 2 nm), only one quantum confined hole state is sustained.

The same group then reported the self-assembled growth of AlGaN/GaN nanocavities with active GaN quantum discs embedded in the AlGaN nanocolumn as discussed before.[64] The difference for the nanocavities is that the nanocolumn is cladded on the top and bottom by AlN/GaN-distributed Bragg reflectors (DBR; Figure 15c). The nanocavity was achieved by the AlN/GaN cladding such that their thickness obeys $n_i d_i = \lambda/4$, where $\lambda$ is the emission wavelength from the active GaN quantum discs, and $d_i$ is the GaN quantum disc thickness. Five GaN quantum discs of 3 nm thickness were incorporated in the AlGaN nanocolumn and cladded with the DBRs (Figure 15d). Six and 11 periods of AlN/GaN (32/40 nm) bilayer cladding were applied at the top and bottom of the active region to give reflectivities (R) of 50 and 90%, respectively. Extended defects and cracks in the sample are avoided by lattice and thermal relaxation at the sample–substrate interface and the DBR built-in strain is released through the high surface area of the nanocolumn structure. However, the growth of the nanocavity is highly complicated, with disorder introduced during the DBR growth that enhances the nanocolumn diameter, which could ultimately coalesce two nanocolumns. The nonoptimized DBR growth conditions that destroy its periodicity will in fact affect the optical properties of such complex nanocavity structures made from group III-nitride systems.

## 6. SYNTHESIS OF TERNARY GROUP III-NITRIDE SEMICONDUCTORS

Ternary group III-nitride systems are studied for the interesting tunable emission that it could generate (Figure 16). For example, indium gallium nitride (InGaN) has been the active layer for most high-brightness LED devices reported so far. The intrinsic bandgap of AlN could be reduced systematically with increasing Ga incorporation in the network.[65] $Al_xGa_{1-x}N$/GaN heterostructures formed by radio-frequency plasma-assisted MBE exhibited a two-dimensional electron gas (2DEG) system also.[66] The electron mobility of the $Al_xGa_{1-x}N$/GaN heterostructure was found to decrease with increasing Al content and thickness of the $Al_xGa_{1-x}N$ layer. However, a high electron mobility of 51,700 $cm^2$/Vs was achieved at 13 K using a 16-nm layer of $Al_{0.09}Ga_{0.91}N$. In short, both optical and electrical properties could be tuned in the ternary systems that make it so attractive for recent advances in optoelectronics.

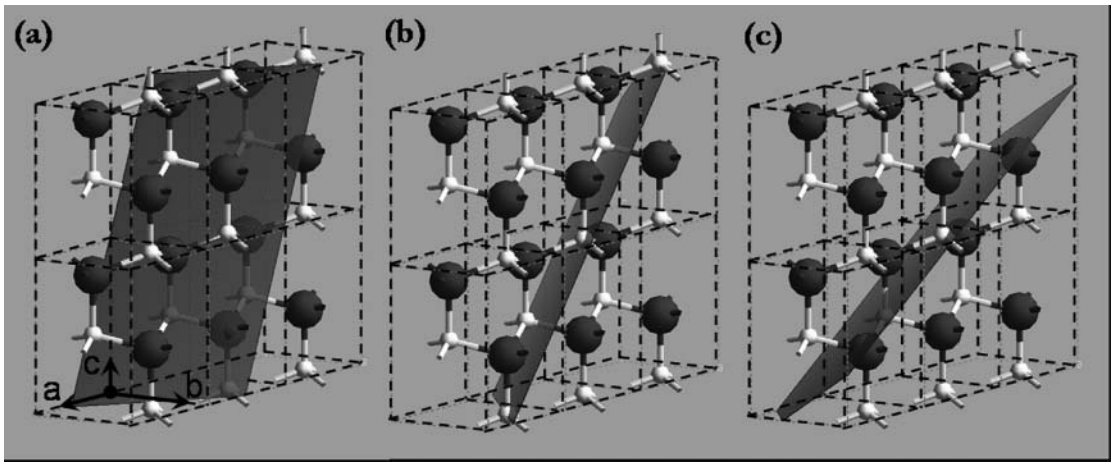


FIG. 11. Atomic arrangement in an AlN crystal showing the stable nongrowth surfaces of (a) (221), (b) $(1\bar{1}1)$, and (c) $(1\bar{1}2)$ making angles of 81, 61, and 43 degrees, respectively, with the basal plane. The *c*-axis shown in the figure is the [001] direction. (Reprinted with permission from Shi et al.[31] Copyright 2005 Wiley-VCH Verlag GmbH & CoKG.)



There has been a recent report on the growth of AlGaNNWs by the MOCVD technique.[67] Tri-methyl aluminum (TMAl) and TMGa was used as the source precursor and $NH_3$ as the nitriding gas. The ratio of TMAl/[TMGa+TMAl] was varied between 0% (GaN) to 100% (AlN). Polycrystalline alumina with 0.4–0.8 nm of Ni was used as the substrate. Long NWs (4–5 $\mu$m) with low density and clean background and short (1–2 $\mu$m) rod-like morphology with nanocrystallites in the background were observed at high and low gas-phase Al vapor content, respectively. The absence of TMAl or TMGa resulted in short GaNNRs and AlN film, respectively. The AlGaNNWs growing along the $[10\bar{1}0]$ direction have a dark core and a light sheath contrast as observed from transmission electron microscopy (TEM) measurements (Figure 17a). The composition profile suggests that the NWs are Al rich on the outside and Ga rich on the inside (Figure 17b). AlGaAsNWs were tried by different techniques,[68,69] and phase segregation was observed in the growth of AlGaNNWs[70] by hot wall chloride vapor epitaxy.

However, the incorporation of InN in GaN or AlN is difficult. Valence force-field model calculations[71] showed the existence

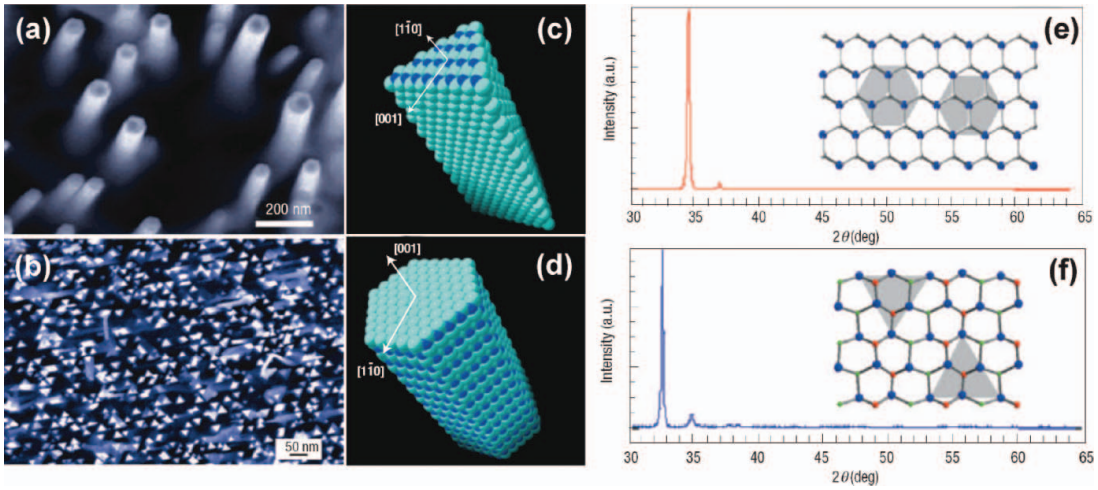


FIG. 12. SEM images of GaNNWs grown on (a) (100) $\gamma$–$LiAlO_2$ and (b) (111) MgO substrates. Space filling structural models of the GaNNWs with the (c) triangular and (d) hexagonal cross sections corresponding to (a) and (b), respectively. XRD patterns of the GaNNWs (e) as shown in (a) and (f) as shown in (b). The insets show the crystal structure of the substrates at the interface between the substrate and the NW that dictate the selective GaNNW growth. The grey boxes indicate the respective orientation of the GaN crystal planes at the interface. (Reprinted with permission from Kuykendall et al.[58] Copyright 2004 Nature Publishing Group.)

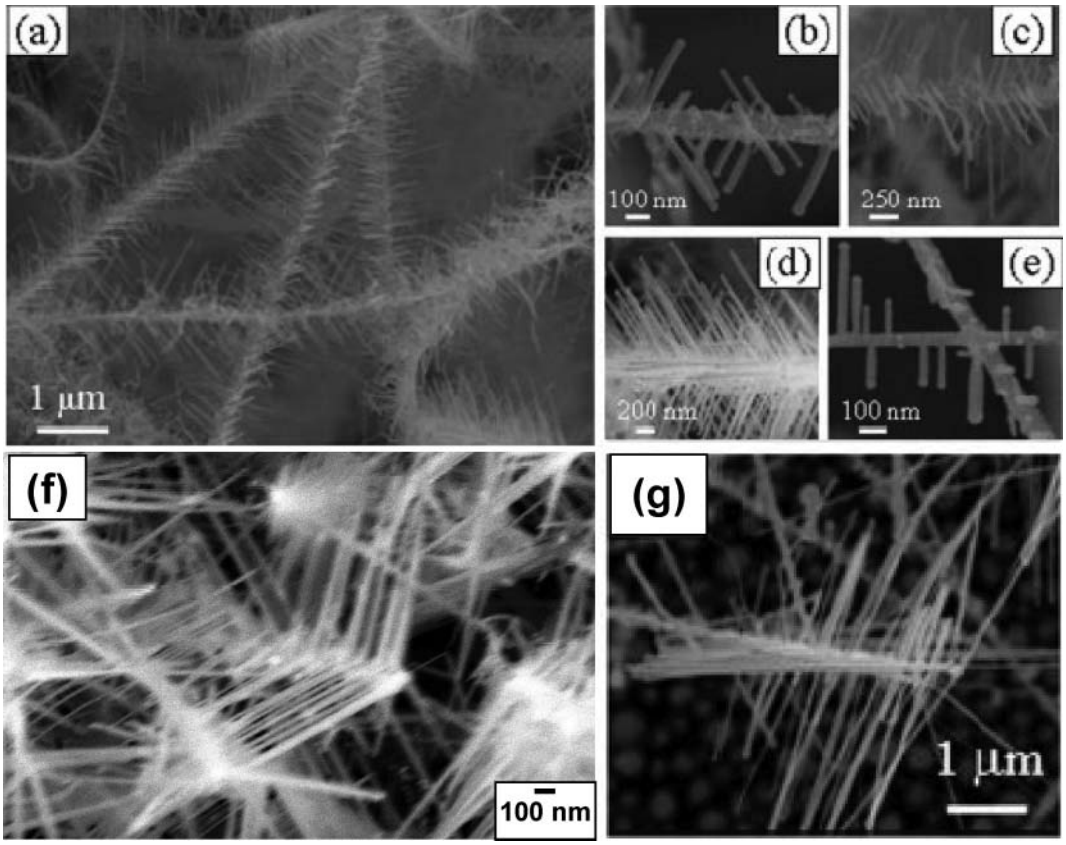


FIG. 13. (a) Medium magnification FESEM image of homojunction (GaN on GaN) nanobrushes showing the presence of two- and fourfold nanostructures. (b)–(e) High-magnification images showing (b) 4S-fold, (c) 4M-fold, (d) 4M*[1]-fold, and (e) 2S-fold subsymmetries. (f) FESEM image of InN nanobrushes, InNNWs on InNNB, prepared by MOCVD. (g) FESEM image of a heterojunction nanobrush, InNNRs on GaNNW, showing 2S-fold subsymmetry. (Reprinted with permission from Lan et al.[60] Copyright 2004 Wiley-VCH Verlag GmbH & CoKG.)



of a solid-phase miscibility gap due to the large difference in the interatomic spacing between InN and GaN. There are other concerns about the growth of the ternary phase arising out of a narrow temperature window for the growth of InN and GaN. GaN, or AlN in that sense, grows at high temperatures exceeding 800°C, whereas InN can be grown around 540°C to prevent InN dissociation. However, InGaN is an indispensable part of the high-efficiency LEDs performing in the red to UV range of the spectrum. The use of high nitrogen and indium source flow rate enabled the deposition of relatively good quality In-Ga-N film by MOCVD.[72] But strong band-to-band emission at room temperature was demonstrated by Nakamura et al. in InGaN film[73] and multi-quantum-well (MQW) structures.[74] The reason that these InGaN films emit so strongly despite having a high density of threading dislocations from $1 \times 10^8$ to $1 \times 10^{12}$ $cm^{-2}$ is not clear.

Recently there has been a report of InGaNNRs grown on Si by hydride vapor-phase epitaxy (HVPE) that are nearly defect free.[75] The source precursors resulted from reactions of high-purity In (6N) and Ga (7N) metal with HCl gas (5N) in the presence of $N_2$ at 750°C and then transported to the substrate region and reacted with $NH_3$ (6N4) at 510°C. In and Ga, were varied between 10 and 100 sccm and 100 and 300 sccm, respectively, and $NH_3$ flow rate was kept between 4000 and 5000 sccm for the growth time of 5 h. A yellowish product was obtained on the Si substrate, which was found by electron microscopy to be InGaNNRs with 50 nm diameter and 10 $\mu$m length. TEM studies revealed that the growth direction was [0001] for the NRs. The same technique can also produce aligned InGaNNRs arrays growing along [0001] on sapphire substrates.[76,77]

InGaNNWs with straight or helical shapes were prepared by a thermal CVD technique using Au-coated silicon substrates.[78] A temperature of 600°C and pressure of 3.5 Torr were used for the growth. The formation of the coiled or helical InGaNNWs with an In-rich core could not be easily explained. However, following other similar coiled structures, the authors opined that it may be due to lateral displacement of the catalyst particle with respect to the central axis of the NW during growth. Another school of thought is that the different growth rates for the core and the shell could probably give the helical shape for the NWs.

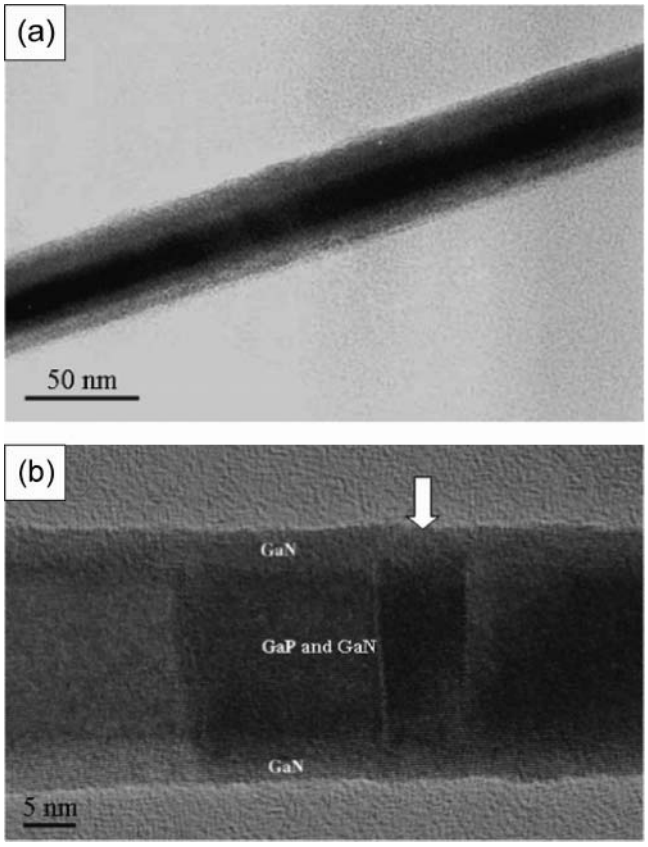


FIG. 14. HRTEM image of a single core-shell (a) GaN@GaPNW and (b) GaP@GaNNW. The misfit dislocation is marked by an arrow in (b). (Reprinted with permission from Lin et al.[61] Copyright 2003 American Chemical Society.)

Vertically aligned InGaNNTs were grown on InGaN thin films grown on sapphire substrate.[79] A 30-nm low-temperature GaN buffer layer was grown at 500°C on sapphire substrate on which a 2-$\mu$m-thick undoped GaN buffer was grown at 1,000°C. Subsequently, a 3-nm InGaN was grown at 730°C. Thermal annealing of the InGaN film at 740°C at atmospheric pressures for 20 min in a quartz furnace produced the NTs.

A complicated core-multishell NW heterostructure is reported for the ternary system for use in multicolor, high-efficiency nanoscale LEDs.[80] The structure of the core (n-GaN)-multishell (i-InGaN/i-GaN/p-AlGaN/p-GaN) NWs is shown schematically (Figure 18a). The NW was synthesized by a catalyst-assisted MOCVD process for the core wire and subsequent shell deposition onto the core. $NiNO_3$ solution–coated sapphire substrate was used for the core n-GaN (Si-doped) NWs grown at 950°C, using TMGa and $NH_3$ with $SiH_4$ in $H_2$ for the doping purpose. An intrinsic InGaN layer, of 8 nm thickness, was deposited on the GaN core by the same MOCVD process using TMIn and TMGa in $N_2$ at 600–800°C. By controlling the growth temperature, the In content and hence the bandgap of the InGaN can be systematically tuned. The intrinsic GaN (28 nm) and p-AlGaN (33 nm) layers were subsequently deposited with TMAl used as the Al source at 860 and 940°C, respectively. The final p-GaN shell was deposited in $H_2$ at 960°C using biscyclopentadienylmagnesium as the p-type dopant. The NWs have a triangular cross section and grow along [11$\bar{2}$0] direction. The NW is nearly dislocation free, which suggests epitaxial shell growth. The energy band diagram of the core multishell NW is shown in Figure 18b and the LED application of this structure will be discussed in Section 11.2.

An attempt to grow InGaNNWs by a VLS process using In, Ga, and $NH_3$ as precursors and Au as catalyst always produced Ga-rich and In-rich InGaNNWs at high and low growth temperatures, respectively.[81] TEM studies revealed that the NWs are either predominantly binary GaN or InN with some ternary self-assembled quantum dots (SAQD) embedded in them. The strain in the inhomogeneous structure and the low miscibility of GaN and InN are probable reasons for the formation of SAQDs in NWs. The optical properties of the NWs were dominated by the SAQDs that phase separated from the bulk of the NW. The PL spectra show peaks inconsistent with the binary composition and can only arise due to a ternary $In_xGa_{1-x}N$ phase. This study also underlines the difficulty in growing defect-free ternary materials without phase separation.

## 7. STRUCTURE AND BONDING

The purity and quality of the material are often judged by its structure and nature of bonding. Structural characterizations such as XRD, TEM, and Raman and infrared spectroscopy are essential for this purpose.

### 7.1. Defect/Strain

XRD patterns are often used as basic signatures for the quality of the nanomaterial in contrast to the bulk. Typical XRD spectra of GaNNWs or GaNNRs will show similar features as that of the bulk. But a change in the intensity ratio of the peaks will show any preferred growth directions present in the NWs or NRs. For example, the GaNNWs grown by thermal CVD using Co-$TiO_2$ catalyst[45] showed the hexagonal fingerprints similar to bulk GaN, but the intensity ratios of the (100), (002), and (101) triplet (72:100:84) is clearly different than the 70:50:100 observed for the bulk phase (JCPDS file No. 2-1078). This might signify a preferential growth along [002] direction. However, the (111) signature of cubic GaN could overlap with the (002) of hexagonal GaN, complicating the analysis. Growth directions could also be directly affirmed from TEM measurements as shown for the GaNNWs growing along [100]. However, the growth direction is highly system dependent and reports of [100][82] and [110][83] growth directions are not scarce. The strain in the GaNNWs can also be estimated from the XRD spectrum. GaNNWs prepared by catalytic CVD at 900–1,050°C using Fe NPs[84] show an ensemble XRD spectrum that is shifted toward higher $2\theta$ values with respect to the GaN epilayer or GaN bulk powders (Figures 19a, 19b). Here, the XRD reflects the separation of lattce planes that are along the growth direction but not

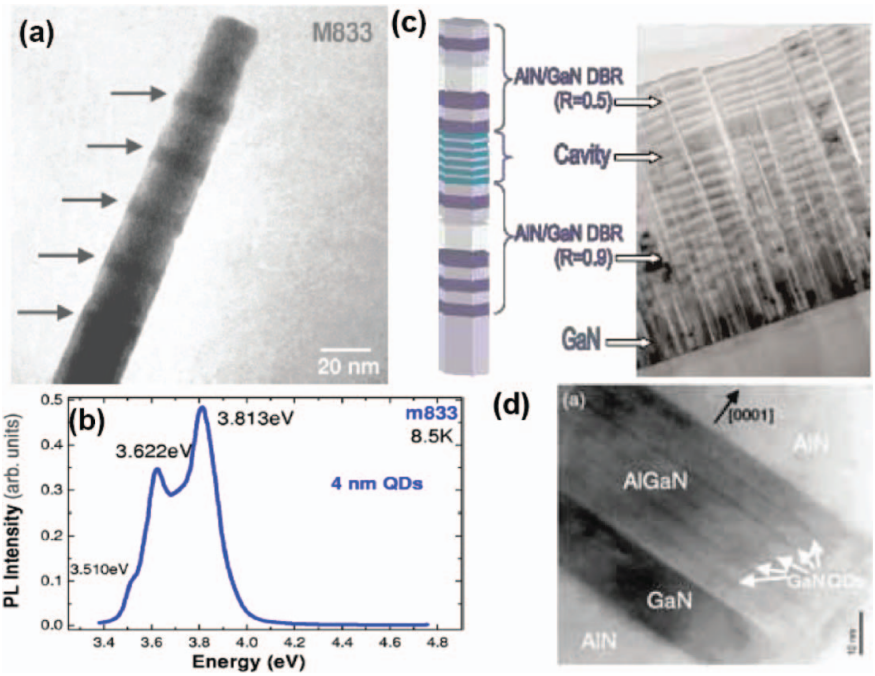


FIG. 15. (a) Cross-sectional TEM image of the 4-nm-thick GaN quantum disc embedded AlGaN nanocolumn; (b) PL spectrum measured at 8.5 K for the nanocolumn described in (a). (c) The scheme of the nanocavity structure is shown on the left. The white color disc within the AlN/GaN distributed Bragg reflectors (DBR) means "and so on." On the right is cross-sectional TEM image of the nanocavity structure; (d) High-resolution TEM image of the cavity area surrounded by the AlN/GaN DBR. (Reprinted with permission from Ristic et al.[63,64] Copyright 2003, 2005 American Physical Society.)

perpendicular to it. Hence, the (100), (002), and (101) diffraction peaks come from different NWs that have the (100), (001), and (101) planes along the growth direction. The amount of up-shift (positive with respect to bulk) was $\Delta(2\theta) = 0.07$, 0.15, and 0.1 degrees for the (100), (002), and (101) diffraction peaks, respectively (Figure 19b). The shift toward higher $2\theta$ indicates smaller lattice spacing in GaNNWs than that of the bulk. This indicates a biaxial compressive stress in the radial direction of the NWs with a resultant uniaxial tensile stress along the length (Figures 19c–19e). The uniaxial tensile stress that would show a higher separation of adjacent planes, perpendicular to the growth direction, and hence a downshift (negative with respect to bulk) of $2\theta$ values, was not picked up in the XRD measurement. These stresses could be accompanied by a change in the bandgap of the material because it is closely related with the bond length in the material.

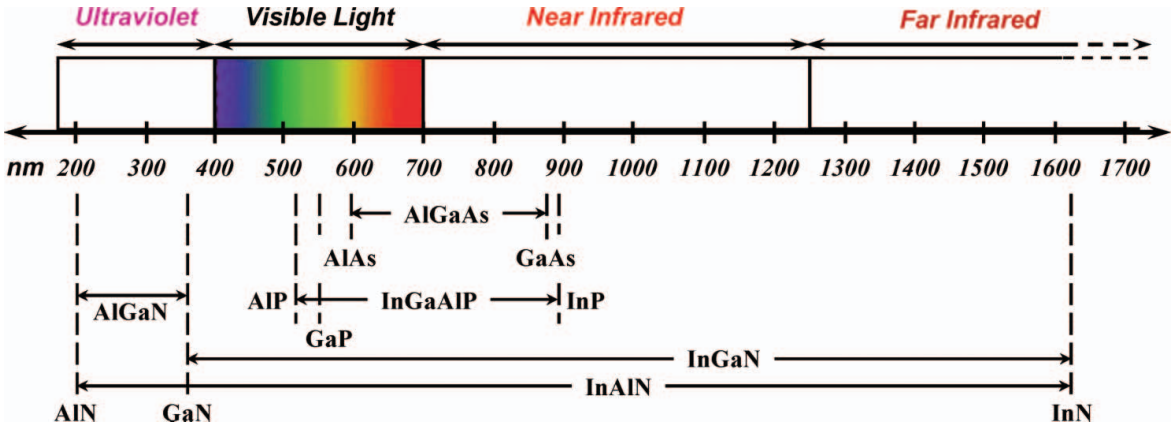


FIG. 16. Various ternary and quaternary materials used for LEDs with the wavelength ranges indicated.

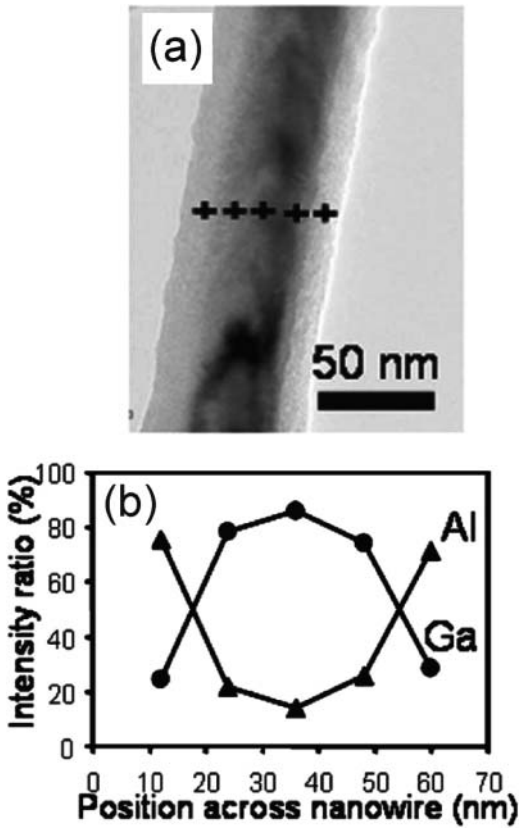


FIG. 17. TEM image of AlGaNNWs on alumina templates with Al gas-phase ratio $x_{Al,gas} = 50\%$, (b) normalized composition profile across the nanowire. (Reprinted with permission from Su et al.[67] Copyright 2005 American Institute of Physics.)

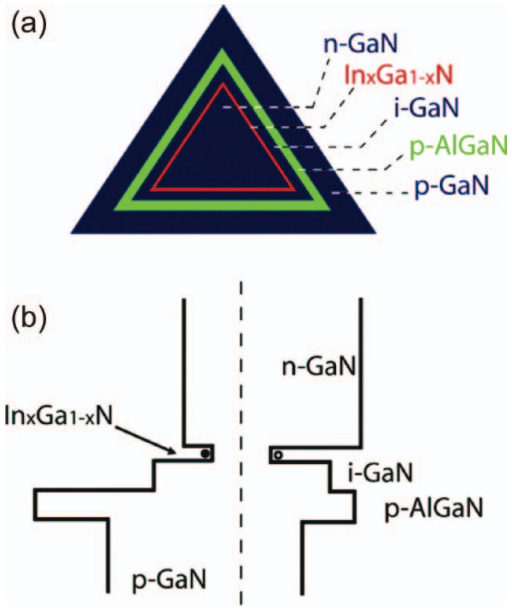


FIG. 18. Cross-sectional view of a core/multishell (CMS) nanowire radial heterostructures and the corresponding energy band diagram. The dashed line in the energy band diagram indicates the Fermi level. (Reprinted with permission from Qian et al.[80] Copyright 2005 American Chemical Society.)

Apart from stress, other kind of defects such as point defects and stacking faults can also be seen through high-resolution TEM. A particularly interesting series of study was performed in this direction by Dhara et al. and Datta et al.[85–88] They compiled a report of self-ion ($Ga^+$) implantation on catalytic CVD-grown GaNNWs by a focus ion beam (FIB) technique. A 50-keV $Ga^+$ ion beam with a fluence ranging from $1 \times 10^{14}$ to $2 \times 10^{16}$ ions/cm$^2$ was used for the purpose. Unlike a bulk amorphization observed in epi-GaN film under heavy ion irradiation, the GaNNWs demonstrate a resistance to amorphization at intermediate fluence. Only at the highest fluence was a complete amorphization of the subsurface region (~15 nm) of the GaNNW observed. At intermediate fluence an enhanced dynamic annealing of point defects, such as vacancies, takes place that resists the amorphization.[85] This is due to the trapping of highly mobile interstitials by the vacancies, resulting in the removal of the defect. The high diffusivity of the interstitials is unique in the confined geometry of the GaNNWs, unlikely to be observed in epi-GaN films. Such self-ion implantation was also found to bring about a hexagonal-to-cubic phase transformation in the $h$-GaNNWs at optimum fluence of $5 \times 10^{15}$ ions/cm$^2$.[86] Interesting observations, such as blister formation in the GaNNWs, were also observed under self-ion implantation.[87,88] Disintegration of lattice atoms, mostly Ga, and its accumulation at the subsurface in the form of metallic $\alpha$-Ga resulted in the blisters (Figure 20). Nitrogen blisters observed in epi-GaN films under heavy ion implantation were not observed in the GaNNWs probably due to the enhanced defect mobility in the NW geometry as discussed before.

In the AlNNTs system,[31] the XRD spectrum gave evidence of stress present in the material (Figure 21). A description of these NTs will be given later. The slant face of the NT showed a stepped nature and a continuous tapering along the length of the NTs, making them smaller and smaller toward the apex. This indicated a restriction in the growth along the radial direction of the NT, whereas the axial growth proceeded unrestricted. This kind of limited growth, however, indicates the presence of stress in the material, which was elucidated by the XRD spectrum. The XRD spectrum clearly showed a shift of the (002) and (100) peaks toward lower and higher $2\theta$, respectively, as compared to bulk AlN powders. As discussed above for GaN, this shift indicated a compressive stress along the radial direction of the AlNNTs and a tensile stress along the [002] growth direction.

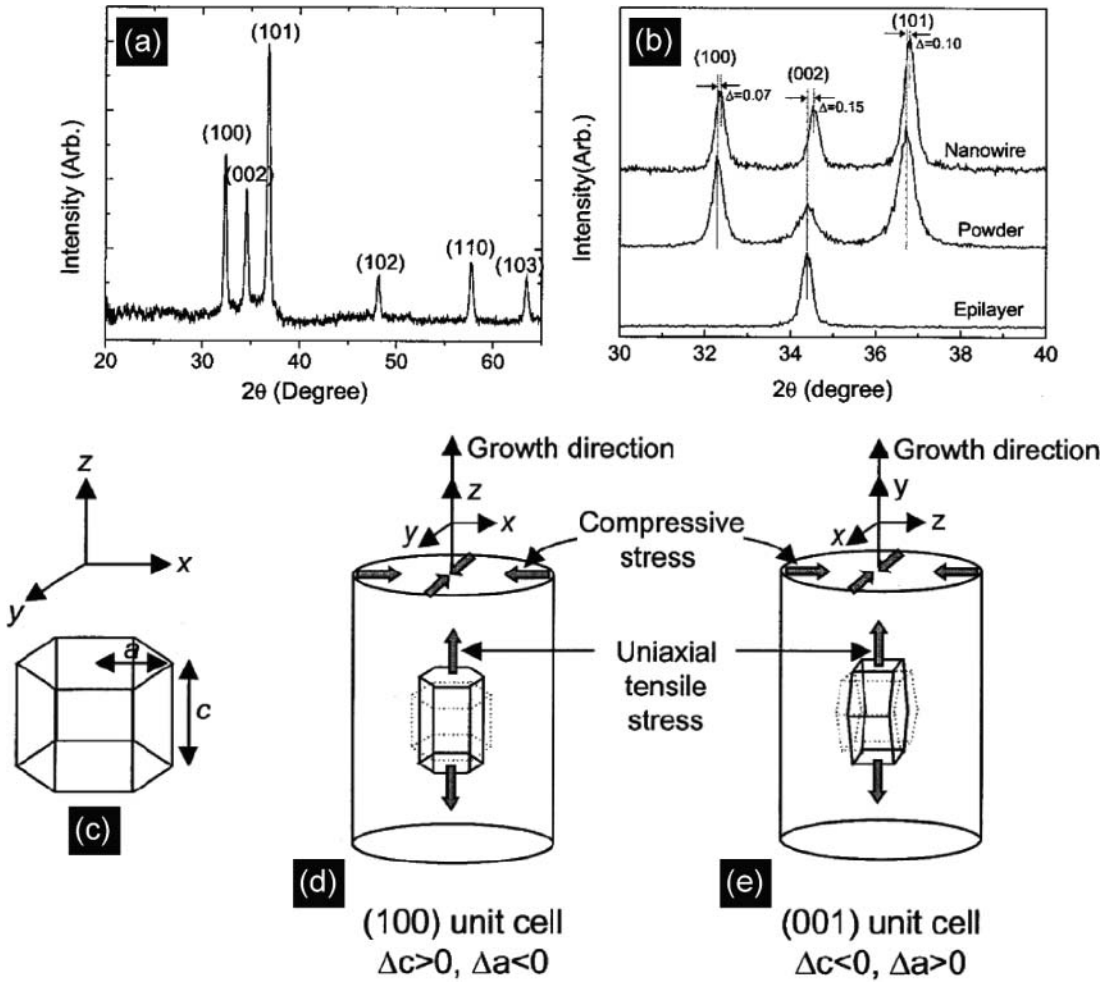


FIG. 19. (a) A full-range XRD pattern taken from the strained GaNNWs. (b) The (100), (002), and (101) peaks for the strained GaNNWs, epilayer, and powders. Schematic diagrams for (c) a hexagonal unit cell with the lattice constants $a$ and $c$, (d) the (100) unit cell that the z-axis is aligned to the growth direction of NW, and (e) the (001) unit cell that the z-axis is perpendicular to the growth direction of NW. (Reprinted with permission from Seo et al.[84] Copyright 2002 American Institute of Physics.)



### 7.2. Raman/Infrared Spectroscopy

The chemical identity and bonding microstructure of a material can be probed by both Raman and Fourier transform infrared (FTIR) spectroscopy complementarily. These techniques can effectively distinguish between a bulk and nanomaterial because some phononic excitation would not be observable in the former because of symmetry restrictions. However, in the nanomaterials, due to exceptionally small dimensions and high surface-to-volume ratio, the phonons may be confined, their symmetries broken, and surface phonons observable with proper excitations. The Raman line shapes carry information about atomic bonding and so does the frequency of infrared absorption bands.

A comparison of Raman spectra for NRs and films of InN, GaN, and AlN has been reported (Figure 22).[89] The films have stronger and sharper Raman signals compared to the NRs. The Raman signals from the NRs have asymmetric line shapes and some of the modes are shifted toward lower wavenumbers, except for AlN. These differences are often attributed to size effects. A comparison between the Raman spectra of GaN film and NWs can be found in Liu et al.[90] and the set of vibrations observed in bulk, film, and NW GaN has been tabulated by Chen et al.[57] Significant broadening and asymmetry in certain phonon modes marked the presence of nanocrystalline GaN in the NWs. However, higher order longitudinal optic (LO) phonons could be observed in GaNNWs with diameters smaller than $\sim$3 nm.[91] Stronger electron–phonon interaction in ionic-bonded GaN could enhance the LO phonons so that they can be observed up to the fourth order. This is only possible when the

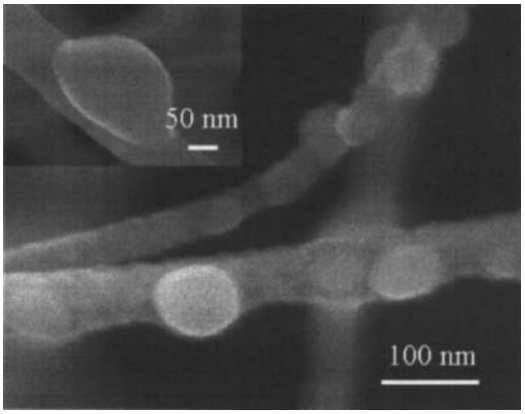


FIG. 20. FESEM images of the nanoblisters formed at 50 keV $Ga^+$ implantation on GaNNWs with a fluence of $2 \times 10^{16}$ ions/cm$^2$. Inset shows a large nanoblister of 200 nm diameter. (Reprinted with permission from Dhara et al.[87] Copyright 2005 American Institute of Physics.)

defect luminescence from the GaN is small, implying very good quality of the crystals. For InN epitaxial films and NWs, the $A_1$(TO), $E_2$, and $A_1$(LO) modes can be observed in the Raman spectra. However, the line shapes for the InNNWs are broader and asymmetric compared to their thin-film counterpart. A large $A_1$(LO) phonon softening was also observed in the InNNWs[25] compared to the film, which is similar to what was observed in the GaN system. InN nanostructures even show distinction between NWs, NBs, and NRs as revealed by Figure 23. In addition to the symmetry allowed modes, such as $E_1$, $A_1$, and $E_2$ (high), InNNWs and InNNBs also demonstrated surface optic (SO) modes, which are generally not observed in the Raman spectrum due to symmetry considerations.[92] Surface nanotexturization sometimes excites these otherwise forbidden Raman modes.

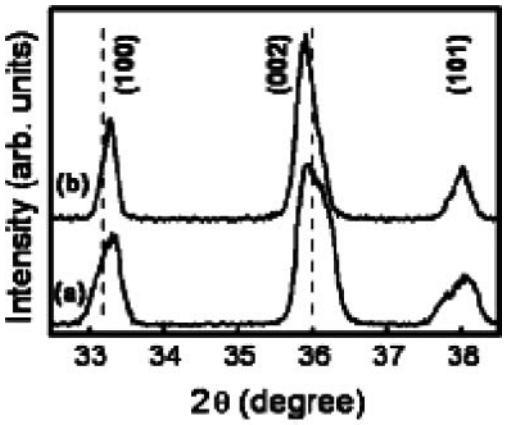


FIG. 21. XRD spectra for the AlN (a) nanotips (b) nanorods. The vertical dashed line represents the bulk AlN positions for (100) and (002) reflections (JCPDS Card No. 25–1133). (Reprinted with permission from Shi et al.[31] Copyright 2005 Wiley-VCH Verlag GmbH & CoKG.)

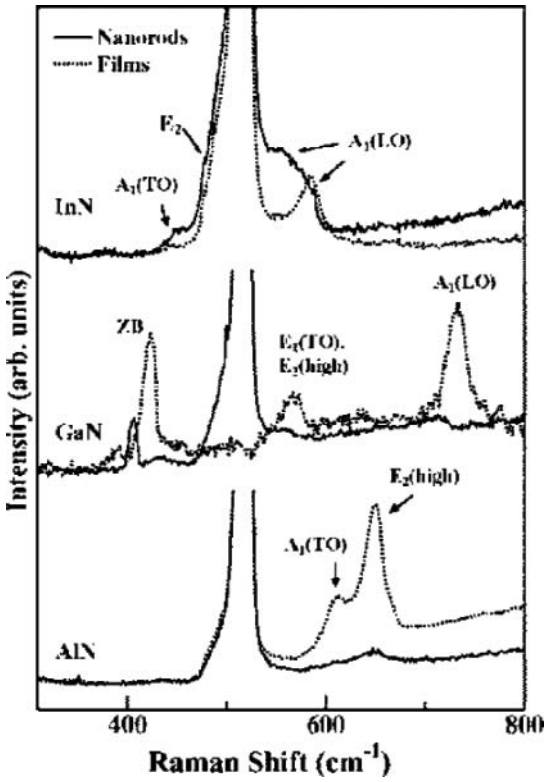


FIG. 22. Comparative Raman spectra for films and nanorods of InN, GaN, AlN. The spectra show different $A_1$(TO), $A_1$(LO), $E_2$, and zone boundary (ZB) phonons in these systems. The strongest signal from the Si substrate has been cut off. (Reprinted with permission from Pao et al.[89] Copyright 2006 American Institute of Physics.)

## 8. OPTICAL PROPERTIES

Optical properties of nanomaterials are interesting and rich in information because they carry the quantum mechanical phenomenon of photon confinement with them. PL,[93] cathodoluminescence (CL),[94] thermoluminescence (TL), and optical absorption measurements form the basic characterization tools for the optical properties. Piezoreflectance (PzR) spectroscopy[95] has also been used in a limited way. These techniques, except CL, although suitable for the thin-film system, are not uniquely conclusive for the nanosystems in a sense that the large probe size often obscures the signal of the nanomaterial from a host of backgrounds. Even a size distribution of NWs or particles would result in a broadening of the PL signal being collected from several hundreds of those. The narrow electron beam used in the CL technique, however, can perform single nano-object spectroscopy and is relatively error free.

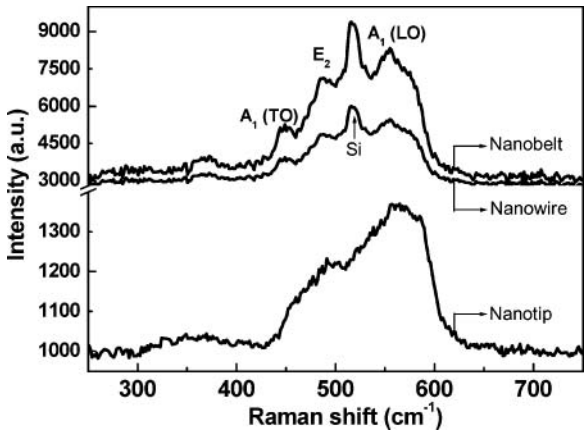


FIG. 23. Representative Raman spectra for InN nanowires, nanobelts, and nanotips. The position of the Si Raman line at 520 $cm^{-1}$ is indicated.

The optical properties of the dimensionally limited nanomaterials are vastly different from their bulk counterpart. Limiting the electron motion in any one of the three degrees of freedom will alter the electronic density of states, especially near the band edges. Excitonic transition energies can also shift, usually to the blue, if the material dimension is close to the Bohr radius of the exciton. This is the quantum confinement regime. The Bohr radius for GaN is within 2.8–11 nm.[17,96,97] The shift in the transition energy ($\Delta$E) can be calculated by solving the Schrödinger equation for electrons in a quantum wire. Assuming the NW of diameter $d$ as an infinite potential well, $\Delta E$ was found to be

$$\Delta E = (h^2/2m_e)\left(j_x^2 + j_y^2\right)\pi^2/d^2 \qquad [12]$$

where h is the Planck's constant, $m_e$ is the effective electron mass, and $j_x$ and $j_y$ represent integers.[98] GaN having $m_e = 0.22$ $m_o$, where $m_o$ is the rest mass of electron, can have energy shifts of ~1–100 meV when the NW diameter is reduced from 100 to 10 nm. Most GaNNRs or GaNNWs having a band edge transition at 3.4 eV do not show any such shifts due to their large diameters compared to the Bohr radius. But a 200 and 60 meV blue shift of the transition edge energy was observed for GaNNWs ($d \approx$ 10–40 nm) by Chen et al.[99] and GaNNRs ($d \approx$ 80–120 nm) by Kim et al.[100] However, concern remains about the cause of the blue shift because the synthesis of NWs within the limit of the small Bohr radius is extremely difficult. One possible origin of such blue shifts beyond the confinement regime may be the surface states. An anomalous blue shift was observed in ZnONRs that was explained by the existence of a few surface layers that had a bandgap exceeding the bandgap of the rest of the sample.[101] Hence, transitions occurring at the surface may show a blue shift in the emission spectrum. This argument may be extended to GaN as well. A quantum confinement effect in the NWs can, however, be corroborated from the CL spectrum showing a comparison of GaN thin film and single GaNNW of different diameters.[102] The cause of broadening of the line width of the CL signal is, however, more unanimous and attributed to the crystallite size distribution in the nanomaterials.

However, nominally doped n-GaNNWs have, along with the blue band edge emission, another band at 2.2 eV popularly known as the yellow band. This yellow band was found to blue shift with increasing fluence of self ($Ga^+$)-ion implantation.[103] The chemically clean implantation was done by an FIB machine using a 50-keV $Ga^+$ beam using a fluence of $1 \times 10^{14}$ to $2 \times 10^{16}$ ions/$cm^2$. The yellow band shifts to ~2.8 eV at the highest fluence. The blue shift of the yellow band is believed to be due to shallow donors introduced by nitrogen vacancies in the GaNNW. These vacancies created by the implantation process behave as point defect clusters. A two-step high-temperature annealing of the GaNNWs, first at 650°C for 15 min and then at 1,000°C for 2 min in nitrogen ambient, restores the position of the yellow band by removing the nitrogen vacancies. Contributions from the deep acceptors, created by Ga interstitials, cannot be ruled out as a source of the blue shift also.

Optical properties of InN are also shrouded in controversy with both infrared and visible bandgaps being reported. However, the IR bandgap enjoys greater support recently with the visible bandgap being attributed to an indium oxide phase in the material,[104] quantum size effect,[105] Burstein-Moss shift,[106] or nitrogen excesses in InN.[107] Oxide-assisted InNNRs grown by a catalytic thermal CVD process showed a bimodal size distribution with optically black and brown NRs demonstrating diameters of 50–100 and 30–50 nm, respectively.[51] The optically black and nearly defect-free InNNRs showed a PL emission at 0.76 eV (at 20 K) that blue shifted to 1.9 eV (at 300 K) for the brown InNNRs. This shift of ~1.1 eV cannot be explained on the basis of indium oxide formation, Burstein-Moss shift, or quantum size effect alone. For example, the InN crystals should have a size less than 5 nm to have a shift of 1.1 eV according to quantum confinement, whereas the brown InNNRs were 30–50 nm. The Burstein-Moss effect can cause a shift of only 0.5 eV for a carrier concentration increase of over 2 orders in magnitude. Hence, this result indicates a convoluted contribution of quantum confinement and Burstein-Moss shift toward the blue shift of the PL emission in InNNRs.

Recently, a unique NT structure of InN has been reported by the resistively heated MOCVD process.[53] PL measurements on these NTs supported the IR band edge emission at 0.77 eV with a full width at half maxima of 18 meV. A side peak at 0.754 eV was observed and attributed to a 20 meV donor level in InN (Figure 24a). But the striking feature in the temperature-dependent PL of these InNNTs is the absence of quenching near room temperature (Figure 24b). When the measurement temperature was varied from 15 to 300 K, the emission intensity decreased by only 14%. An Arrhenius plot of the normalized

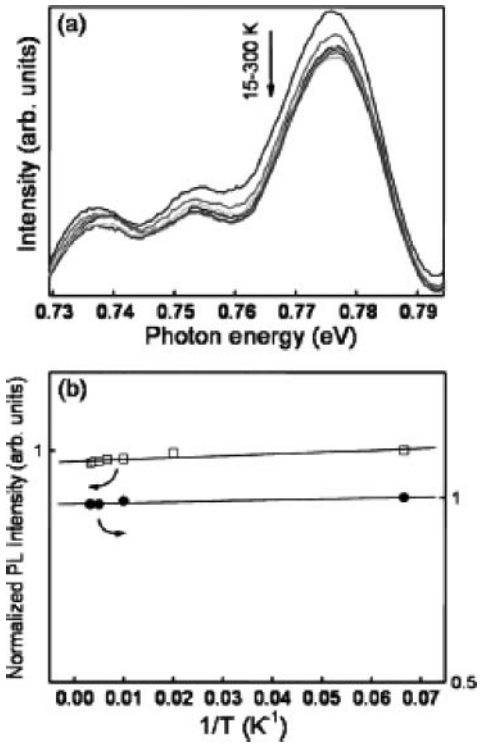


FIG. 24. (a) Temperature-dependent photoluminescence (PL) spectrum of InNNTs measured with 100-mW incident laser power and 3-mm slit width. (b) Two sets of Arrhenius plots of the normalized integrated PL intensity as a function of inverse temperature: (□) 15–300 K with 488 nm laser and 3 mm slit width; (•) 15–320 K with 514 nm laser and 0.5 mm slit width. (Reprinted with permission from Shi et al.[53] Copyright 2005 American Institute of Physics.)

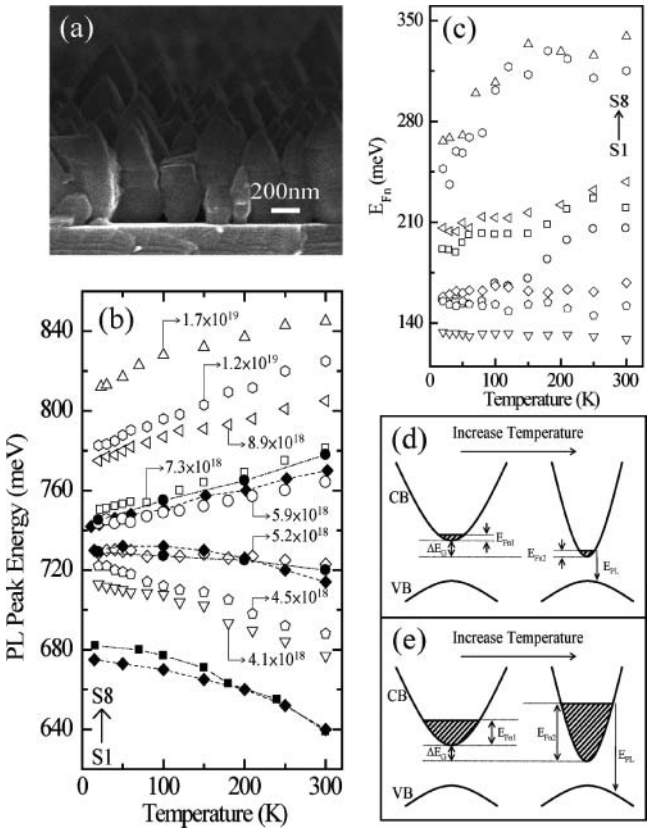


FIG. 25. (a) Cross-sectional scanning electron microscope image of vertically quasi-aligned InN nanocolumns; (b) plot of PL peak energies as a function of temperature for samples S1–S8 (hollow symbols) from this study and from published references (thin film, ♦; nanorods, •, ■). Estimated carrier concentration values (in units of $cm^{-3}$) are marked for each sample (S1–S8). (c) Variation of the quasi-Fermi level, $E_{Fn}$, with temperature, obtained by fitting the temperature-dependent photoluminescence spectra for each sample (S1–S8) according to published equation. (d) Schematic band diagram showing the change in the intrinsic bandgap ($\Delta E_G$), defined as the separation between the conduction band minima and valence band maxima, and the quasi-Fermi level $\Delta E_{Fn} = E_{Fn2} - -E_{Fn1}$, with temperature for (d) low- and (e) high-carrier-density InN nanocolumns. The optical bandgap, $E_{PL}$, is also shown. (Reprinted with permission from Wei et al.[109] Copyright 2009 Optical Society of America.)

PL intensity with inverse temperature should show two distinct slopes with low and high activation at low and high temperatures, respectively. However, for the InNNTs the quenching of the PL intensity near room temperature was very weak and hence the high activation region of the Arrhenius plot was missing altogether. This reduced temperature quenching suggests high internal quantum efficiency, low defect losses, and low thermal escape of carriers in the InNNTs.

InNNWs or InNNRs showed an anomalous temperature evolution of their PL peak energy ($E_{PL}$) that does not follow the trend of common nondegenerate semiconductors. InN has been shown to be degenerate, with high intrinsic carrier density, and demonstrates a blue shift of the $E_{PL}$ with increasing temperature. This finding puzzled scientists until a report from Shen et al.[108] claimed that it might be due to a surface band bending occurring in degenerate InNNRs as a result of the high surface charge density. In sufficiently thin (small radius) InNNRs, such band bending can be pronounced to open up the bandgap. This is true for nanostructures of different radii. However, InN thin films also showed the blue shifting of the $E_{PL}$ with increasing temperature. The extent of surface charge accumulation in the thin films is not as high as in the case of nanostructures. In a quest for a more fundamental answer to this issue, Wei et al.[109] proposed that this effect may be due to a change in the electron effective mass as a function of temperature in InN. This is true because InN has a nonparabolic conduction band edge whose shape—i.e., dE/dK—can change significantly with temperature,

affecting the effective mass of electrons. An approximate 10% reduction in effective mass with 280 K change in temperature is possible in degenerate InN. InN nanocolumns (Figure 25a) studied by Wei et al.[109] showed that samples with $E_{PL} \sim 0.73$ eV showed temperature invariance of $E_{PL}$, whereas samples with $E_{PL}$ lower and higher than this value show conventional red shift and anomalous blue shift of $E_{PL}$ with increasing temperature (Figure 25b). After confirming that the individual $E_{PL}$ values do increase with increasing carrier density (Burstein-Moss shift), Wei et al.[109] came to the conclusion that the temperature evolution of $E_{PL}$ is the result of a competition between the conventional red shift from lattice dilation, dominant for low carrier density samples, on one hand, and a blue shift of the electron and hole quasi-Fermi-level separation, dominant for the high carrier density samples, on the other. The electron quasi-Fermi level is shown to blue shift strongly with temperature (Figure 25c) for the high-carrier-density samples and dominates over the competing conventional red shift of $E_{PL}$. A schematic for such temperature-dependent change of $E_{PL}$ in low- and high-carrier-density samples is also shown (Figure 25d). This suggests that such anomalous temperature dependence of $E_{PL}$ has more to do with carrier concentration, in general, for samples with similar crystal sizes. Additional effects of surface charge density[108] have to be incorporated if the size distributions of the samples are largely different. This is supported by a recent report that demonstrates a larger blue shift of $E_{PL}$ in InN nanobelts, in comparison to thin films, with increasing excitation intensity.[110] The reason attributed to such blue shift of $E_{PL}$ in the nanobelt system is again the surface charge accumulation and the band bending at the surface. Hence, surface band bending is a critical parameter in InN systems with large disparity in crystal size; however, the carrier density is a more fundamental parameter controlling the temperature evolution of $E_{PL}$.

There has been a report on random lasing from InNNBs with cw laser pumping at 20 K.[111] A superlinear dependence of the PL intensity vs. excitation power density could be observed with significant gain in the intensity and concomitant decrease in the FWHM (from 33 to 2.3 nm) of the PL band around 1,600 nm. At powers higher than 77 kW/cm$^2$, the InNNBs underwent structural damage and lasing could not be observed. These InNNBs, with rectangular cross section, were not vertically aligned, so the possible cavity to sustain the lasing action should come from the longitudnal walls of the belt that are nearly parallel to the substrate. The InNNBs grown on a-$SiN_x$-coated Si substrates must have contrasting refractive indices (RI) on both sides of this cavity to form the waveguide. The authors claim that this function could be achieved with a 2.9 index InN sandwiched between lower RI air (RI = 1.0) and $SiN_x$ (RI = 1.9).[111]

A nanotip morphology was also observed for AlN and was discussed in Section 4.[32] AlN is a direct, wide-bandgap, 6.2 eV, hexagonal, close-packed (hcp) material. This is in marked contrast with other III–V compounds containing Al that show indirect and lower bandgap values such as AlAs with 2.16 eV,

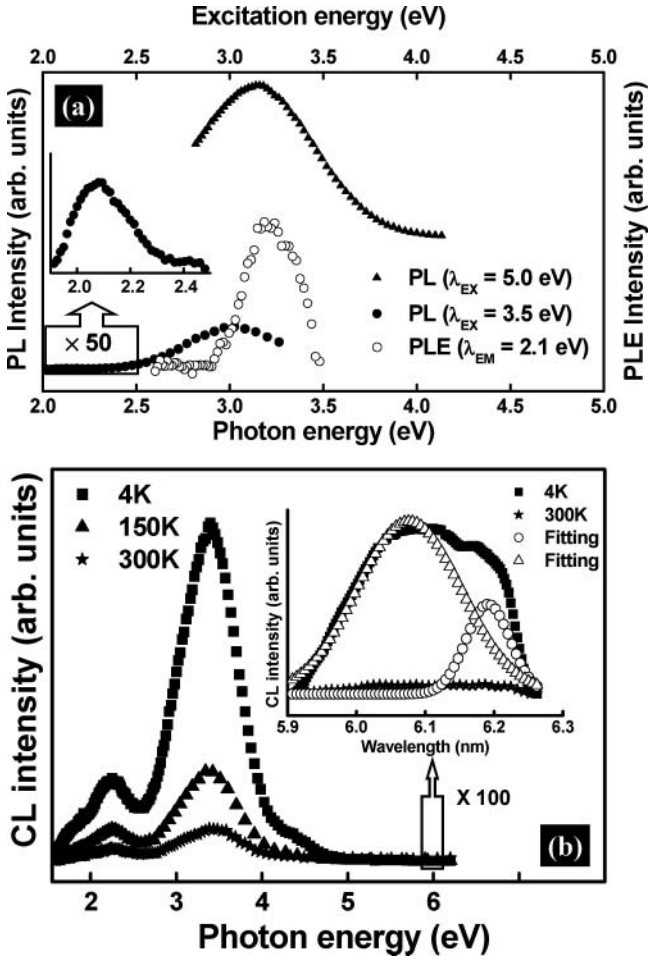


FIG. 26. (a) PL and PLE spectrum of AlNNTs measured at room temperature. PL was measured with (▲) 5.0 and (?) 3.5 eV excitation, respectively. PLE was measured with a detection at (○) 2.1 eV. (b) Temperature-dependent CL spectra from AlNNTs grown on Si substrate measured between 4 and 300 K. The inset shows the near band edge transition, which can be resolved into two peaks. (Reprinted with permission from Shi et al.[112] Copyright 2006 American Institute of Physics.)

AlSb with 1.5 eV, and AlP with 2.45 eV. However, these Al-containing compounds have zinc blende structures, whereas AlN has a wurtzite structure. The PL measurements of the AlNNTs showed two defect-related transitions around 2.1 and 3.4 eV (Figure 26a) and a well-resolved excitonic feature at 6.2 eV (inset, Figure 26b).[112] According to Youngman et al.,[113] the 3.4-eV peak is related to the defect created when oxygen substitutes for nitrogen in the AlN lattice. Interestingly, the position of the oxygen-related defect luminescence in AlN can vary from 3.3 to 4.0 eV as the concentration of oxygen is changed. Based on Strassburg et al.[114] it is presumed that nitrogen vacancies and Al interstitial point defects are responsible for the 2.1 eV emission band. Temperature-dependent CL studies (Figure 26b)

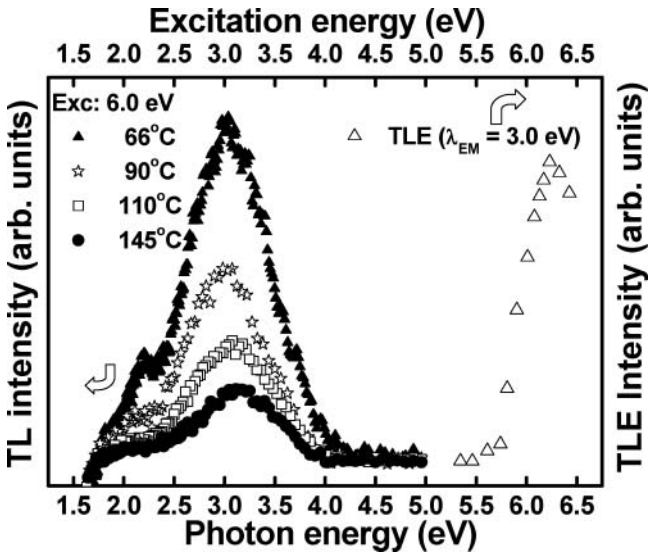


FIG. 27. Thermoluminescence (TL) spectrum of AlNNTs measured at different temperatures between 66 to 145°C with 6.0 eV preexcitation. TLEs were observed at very near band edge. (Reprinted with permission from Shi et al.[112] Copyright 2006 American Institute of Physics.)

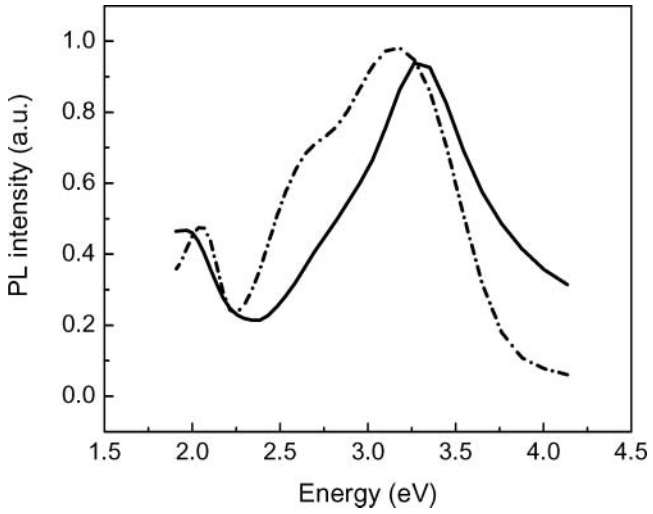


FIG. 28. PL spectra for AlN (···—··) ceramics and (—) nanotips, under an excitation of 6.05 eV. (Reprinted with permission from Shi et al.[112] Copyright 2006 American Institute of Physics.)

also show two broad emission bands at 3.4 and 2.1 eV. The peak at 3.4 eV dominates the spectral range from 1.8 to 6.2 eV. A broad emission ranging from 1.7 to 4.1 eV can be observed in the TL spectra (Figure 27) within the temperature range of 66–145°C with a preexcitation of 6.0 eV. The observed spectra are in good agreement with the results of CL and PL, with defect peaks arising around 3.0 eV (slightly shifted to lower energy) and 2.1 eV. Thermoluminescence excitation (TLE) data suggest that the source of the emission around 3.0 eV is the near host-lattice absorption (∼6.2 eV). The peak around 2.1 eV, however, is unaltered and no optical excitation could be made responsible for this emission, presumably due to the extremely low intensity, which is below the detection sensitivity of the detector used in the TLE measurement system. A significant TL intensity even at high temperatures of 145°C suggests possible ultraviolet detector and dosimetric applications of these AlNNTs. Compared to the bulk AlN macropowders, the AlNNTs show a marked blue shift (+0.2 eV) in the ∼3.2 eV peak (Figure 28).

Ternary group III-nitride systems are ideal to practice bandgap engineering. The low-bandgap InN could be alloyed with the wide-bandgap AlN or GaN to tune the resultant bandgap of the alloy material depending on the concentration of mixing or the molar fraction. A good example of the bandgap engineering can be found in Brunner et al.[65] where the transmission edge was shown to shift to higher energies with increasing Al content in $Al_xGa_{1-x}N$ thin films grown by plasma-induced molecular beam epitaxy (PIMBE). The effective bandgap of $Al_xGa_{1-x}N$ at room temperature shifted toward higher energies following

$$E_{(AlxGa1-xN)} = xE_{(AlN)} + (1-x)E_{(GaN)} - bx(1-x) \qquad [13]$$

where $E_{(AlN)}$ and $E_{(GaN)}$ were found to be 6.13 and 3.42 eV (energy at which the absorption coefficients in AlN and GaN are $10^{4.8}$ $cm^{-1}$; E can be treated as bandgap or absorption edge), respectively. The term b is referred to as the *bowing parameter* and can be determined from a plot of $E_{(AlxGa1-xN)}$ as a function of x. For the $Al_xGa_{1-x}N$ thin films $b = 1.3 \pm 0.2$ eV.

InGaNNRs discussed earlier[75] showed a CL spectrum centered at 428 nm with a full width at half maximum ∼30 nm. These NRs have a composition of $In_{0.1}Ga_{0.9}N$. The same

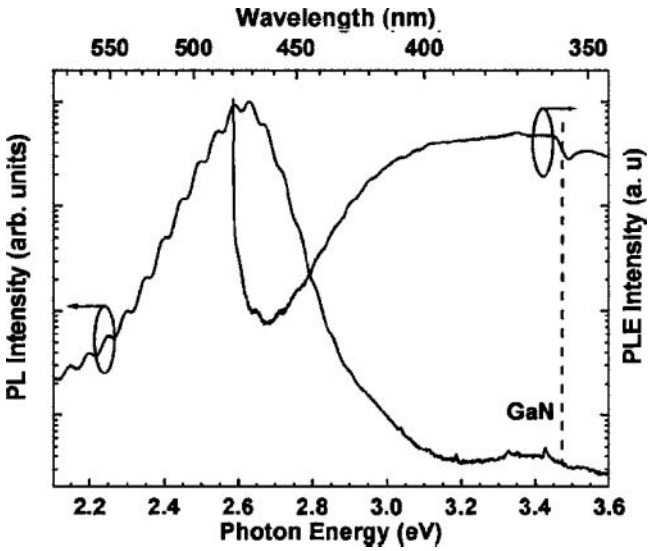


FIG. 29. PL spectrum of the InGaN/GaN MQW nanorod arrays (NRAs) sample with excitation energy of 3.82 eV and PLE spectrum of detection energy at 2.57 eV at 15K. (Reprinted with permission from Sun et al.[115] Copyright 2005 American Institute of Physics.)

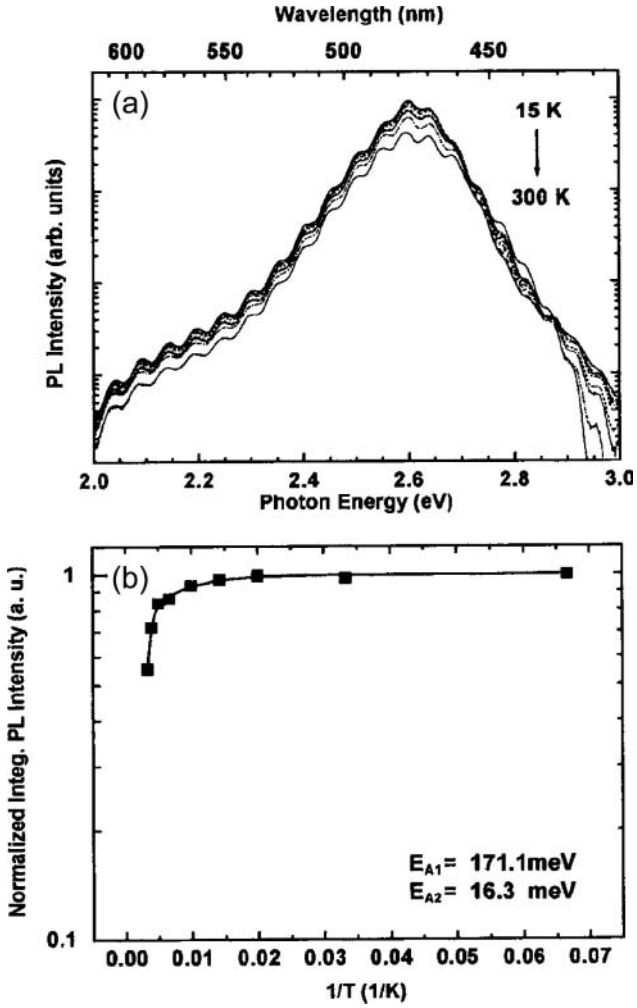


FIG. 30. Temperature-dependent PL spectra from 15 to 300 K excited by 325-nm He-Cd laser and (b) the Arrhenius plot for the InGaN/GaN MQW NRAs sample. (Reprinted with permission from Sun et al.[115] Copyright 2005 American Institute of Physics.)

$In_xGa_{1-x}N$ NRs show a tunable CL emission from 380 nm (3.26 eV) to 470 nm (2.64 eV) as the In content was varied from $x = 0.04$–$0.2$.[77] The low-temperature PL spectrum of the InGaN/GaN MQW NR arrays[115] with an excitation of 3.82 eV and the PL excitation (PLE) spectrum with the detection at 2.57 eV are shown in Figure 29. The intensity ratio from the InGaNQWs to that of the GaN barrier is more than three orders of magnitude. The oscillation seen in the spectrum is due to microcavity effects in the NRs. The temperature-dependent (15–300 K) PL of the MQW NR arrays demonstrate substantially reduced PL quenching of the 477-nm (2.6 eV) peak in the NR arrays as temperature was increased (Figure 30a). An internal quantum efficiency of 55.4% was estimated assuming 100% efficiency at 15 K. The Arrhenius plot of the integrated PL intensity shows two distinct activation energies of 16.3 and 171.1 meV in the low-temperature and high-temperature regimes, respectively (Figure 30b). The activation at high temperature is significantly higher than that obtained for InGaN MQW reported in the literature.[116] The high activation energy of 171.1 meV can be attributed to the thermal escape of holes/electrons from the InGaN QWs into the barriers.

## 9. ELECTRICAL PROPERTIES

With the avenues for selective doping in nanomaterials opening up, electrical measurements are becoming increasingly important and fundamental for the understanding of the nanomaterial. However, making a proper contact to the nanomaterial is a concern and the choice of a contact material is extremely complex and mostly relies on trial-and-error principles. The electrical characterization of the group III-nitride bulk and nanomaterial is discussed in the following paragraphs.

GaN is intrinsically n-type with a carrier concentrations of $10^{16}$ $cm^{-3}$, but which defects are responsible for their n-type behavior is controversial.[117–119] One theory is that the nitrogen vacancy acts as shallow donors and infuses the n-type conductivity in them.[117] Another school shows that the formation energy of Ga vacancies is low and they give rise to the yellow band in the optical measurements.[120] The fact that the yellow band is suppressed under Ga-rich conditions lends support to this theory. There are other experimental observations that oxygen or other impurities such as Si and Ge are responsible for the n-type conductivity and the yellow band observed in nominally undoped GaN.[121,122] Inconclusive experimental evidence suggests that the n-type conductivity and the yellow band may be originating out of different centers in different samples produced by different techniques.

Undoped GaN produced by MOVPE (metal organic vapor phase epitaxy) on GaN buffer/sapphire substrates shows a strong dependence of the electron Hall mobility and electron concentration on the thickness of the buffer layer.[123] The mobility increases with the buffer layer thickness upto 20 nm, decreasing thereafter. The highest value of mobility for these samples was 600 $cm^2$/Vs at room temperature and 1,500 $cm^2$/Vs at 77K. The actual thickness of the GaN layer also affects the mobility and electron concentration. These GaN layers can be doped by Si and Ge during growth.[124] The carrier concentrations increased linearly with the molar flow rate (mol/min) of the dopant gases ($SiH_4$, $GeH_4$). Good quality Si-doped GaN surfaces with carrier concentrations of $2 \times 10^{19}$ $cm^{-3}$ can be obtained. However, the Ge-doped GaN surface degraded at a lower carrier concentration of $1 \times 10^{19}$ $cm^{-3}$. A plot of decreasing electron mobility as a function of increasing electron concentration can be obtained from Jain et al.[125] Annealing temperature-dependent activation energy of 130 and 11 meV for the Si in GaN was obtained by using Hall effect measurements.[126] Other measurements, however, indicate the existence of two donor levels at depths of 12–17 and 32–37 meV where the density of the former exceeds that of the latter by more than a factor of 3.[127] The activation energy obtained from PL measurements was $\sim$22 meV.[127]

Amano et al. reported p-type GaN by doping with Mg.[128] The MOCVD grown GaN layers on AlN buffer/sapphire substrates were doped by $10^{20}$ Mg atoms/cm$^3$ and a resistivity of 35 Ωcm and carrier concentration of $2 \times 10^{16}$ cm$^{-3}$ were obtained.[128] Nakamura, however, obtained p-type GaN with hole concentrations of $3 \times 10^{18}$ cm$^{-3}$ and resistivity of 0.2 Ωcm upon low-energy electron beam irradiation (LEEBI).[129] Hole concentrations in the range of $\sim 10^{18}$ cm$^{-3}$ can be obtained at room temperature. By heating the Mg-doped GaN layers in hydrogen atmosphere the dopants can be deactivated. From the temperature-dependent PL measurements of Mg-doped GaN layers grown by MOVPE and posttreated, ionization energy of Mg around 155–165 meV was obtained.[130] Apart from LEEBI, rapid thermal annealing (RTA), carried out over >600°C, can also lower the resistivities of MOCVD-grown Mg-doped GaN layers by 6 orders of magnitude (from $10^7$ Ωcm for as-grown films to 10 Ωcm for annealed films).[131]

GaNNWs synthesized via a laser-assisted catalytic growth process was used for an FET device preparation and measured for its current-voltage characteristics.[132] Free-standing NWs were dispersed from a solution onto an oxide (600 nm)-covered silicon substrate that served as a global gate. Source and drain electrodes of Ti/Au (50/70 nm) were defined by electron beam lithography and deposited by electron beam evaporation (Figure 31a). The conductance modulation of the GaNNW FET device exceeded 3 orders of magnitude as the gate voltage spanned −8 to +6V (Figure 31b). Carrier concentrations estimated from the total charge, with geometrical dimensions of the NW inserted in the calculation, yielded a value of $10^{18}$ to $10^{19}$ cm$^{-3}$ for the device. The mobility of the n-type GaNNWs measured from the transconductance ranged from 150 to 650 cm$^2$/Vs. This mobility value is at least equal, if not more, than GaN thin films having similar carrier concentrations. The mobility only shows a weak dependence on the carrier concentration, which suggests that a dopant-independent scattering process controls the mobility in the GaNNW FET device. Mg-doped p-type GaNNWs in a similar measurement showed a mobility of 12 cm$^2$/Vs.[133] The mobilities reported for GaNNWs, demonstrating diffusive transport, are mostly in the range of 1–65 cm$^2$/V.s[134–136] compared to that of the bulk crystal ($\mu = 900$ cm$^2$/V.s).[137]

InN films are also intrinsically n-type with high electron concentrations exceeding $10^{20}$ cm$^{-3}$.[138] Mobility and carrier concentrations range from 30 to 100 cm$^2$/Vs and $7 \times 10^{20}$ to $2 \times 10^{20}$ cm$^{-3}$ as the growth temperatures increased from 400 to 525 K. A low carrier concentration at high temperature dismisses the idea of the nitrogen vacancy being responsible for the n-type conductivity, because at high temperature InN dissociation should result in nitrogen reduction in the material. Residual oxygen or impurities are probably responsible for the n-type conductivity in InN. Transport properties of InNNWs grown by a catalytic (Au) thermal CVD were measured.[139] These NWs had 0.76 eV feature in the PL spectrum. The diameters of the NWs ranged from 35 to 120 nm and lengths from 7 to 10 μm. Using shadow mask, Pd/Ti/Pt/Au (5/20/20/100 nm in thickness) was evaporated to make ohmic contacts at the end of the NWs (Figure 32a). Current-voltage (I–V) characteristic was measured at 300 K (Figure 32b). A contact resistivity of $1.09 \times 10^{-7}$ Ω-cm$^2$ and sheet resistivity of $(4 \pm 1.5) \times 10^{-4}$ Ω-cm were obtained from the fit of the total resistance as a function of the ratio of length to area of the NWs (Figure 33). The specific contact resistivity was obtained from a transmission line method analysis and its value confirmed with reported values. A comparison of the resistivity values of InN thin film and NWs show that it is around one order less in the NWs ($4 \times 10^{-4}$ Ω cm), although the contact resistivities are similar.[139]

A diameter-dependent resistivity study of InNNWs was performed[134] in which the total measured resistance of the wire

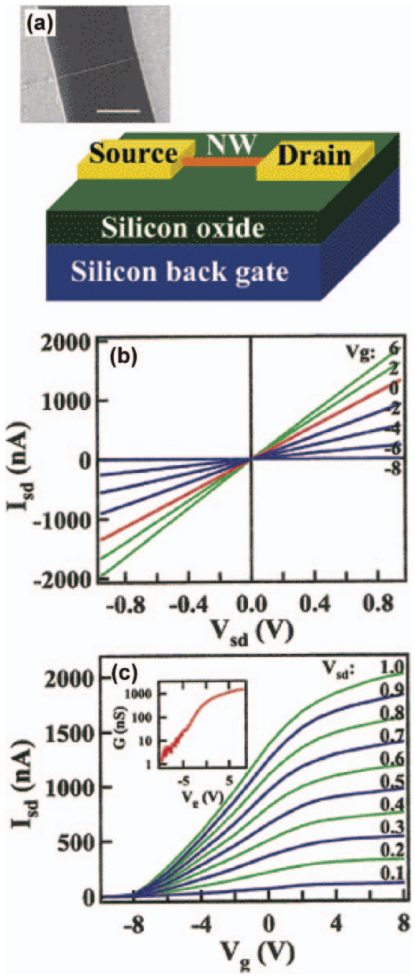


FIG. 31. (a) A schematic of a NW FET and (inset) FESEM image of a GaNNW FET. Scale bar is 2 μm. (b) Gate-dependent $I - V_{sd}$ data recorded on a 17.6-nm diameter GaNNW. The gate voltages for each $I - V_{sd}$ curve are indicated. (c) $I - V_g$ data recorded for values of $V_{sd} = 0.1$–1.0 V. (inset) Conductance, G, vs. gate voltage. (Reprinted with permission from Huang et al.[132] Copyright 2002 American Chemical Society.)

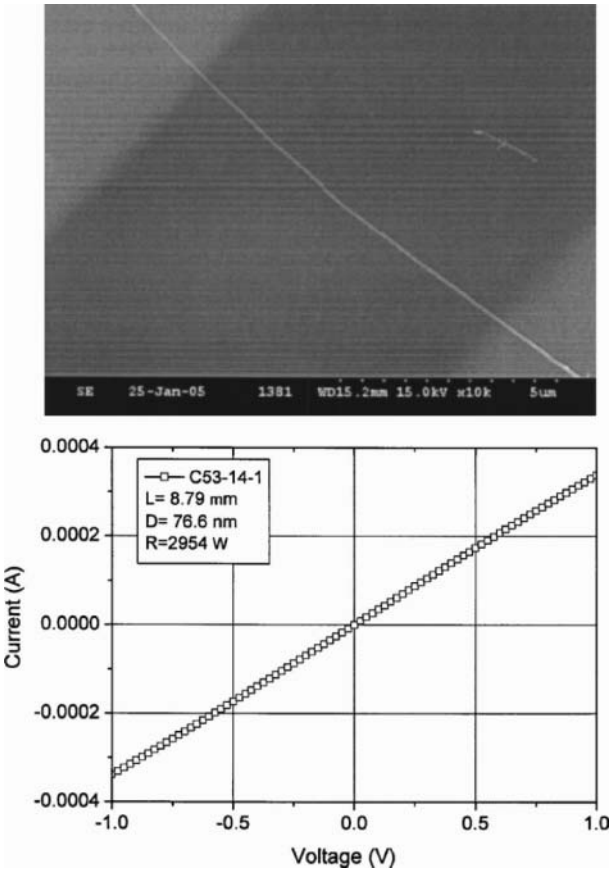


FIG. 32. SEM image of InNNW contacted at both ends by Pd/Ti/Pt/Au (top) and 300 K I − V characteristics (bottom). (Reprinted with permission from Chang et al.[139] Copyright 2005 American Institute of Physics.)

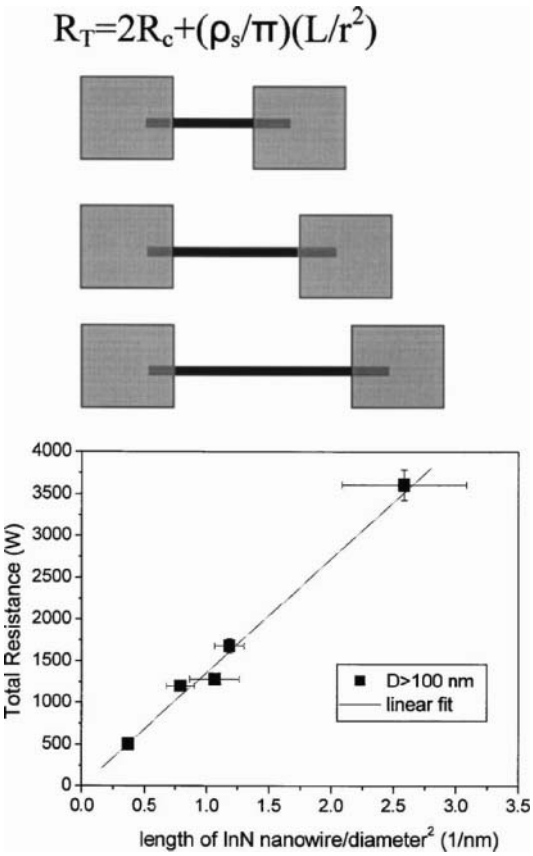


FIG. 33. Contact geometry for measuring the nanowire resistance as a function of length (top) and plot of total resistance vs. length/(radius)$^2$ for nanowires of diameter > 100 nm (bottom). (Reprinted with permission from Chang et al.[139] Copyright 2005 American Institute of Physics.)

was plotted as a function of the ratio of its length/radius$^2$. Above a NW diameter of 100 nm, the resistance showed a classical ohmic behavior; i.e., the resistance increasing with decreasing diameter of the wire. However, for NWs in the diameter range of <90 nm, a decrease of resistance was observed as the wire diameter decreased. This is an anomaly, which was later explained by Yin et al.[140] In a regime of diffusive transport, if the wire diameter is smaller than the carrier size or scatterer potential, the resistance is not inversely proportional to the square of the radius of the wire but in fact is proportional to the number of scattering centers. Each scattering center contributes equally to the resistance as if they are connected in series (neglecting parallel combinations). The electron mean free path ($\ell$) is of the order of the impurity–impurity distance and is given by

$$\ell \propto (1/n_i)^{1/3} \qquad [14]$$

where $n_i$ is the impurity concentration, and for the InN under consideration it was $10^{17}$ to $10^{20}$ cm$^{-3}$. Hence, $\ell \approx$ 2.2–22 nm is the carrier De-Broglie wavelength or the carrier–carrier distance. For InNNWs with radius < 45 nm, the NW dimension $\approx \ell$, and hence the resistance R is given by

$$R = R_C + R_0 n_i AL \qquad [15]$$

where $R_C$ is the contact resistance, $n_i$ is the impurity (scatterer) concentration per unit volume (area [A] × length [L]) of the NW, and $R_0$ is the resistance per scatterer. This expression of resistance, in place of the usual ohmic form, can then explain the anomaly observed by Chang et al. for thin InNNWs.[134]

Field emission (FE) of electrons is an important property of 1D nanomaterials. GaNNWs and AlNNTs exhibit informative FE properties. GaNNWs with diameters of 10–50 nm and lengths of several micrometers were measured in a diode configuration for their FE properties, where the GaNNWs served as the cathode and the conducting glass served as the anode.[26] Substantial emission was observed from the NWs and a linear Fowler-Nordheim plot indicated the quantum mechanical tunneling behavior underlying the electron emission mechanism. A turn-on field (in many cases user defined), defined as the field that would extract an emission current density of 0.01 mA/cm$^2$, of 12 V/$\mu$m was observed. The low turn-on field for

the GaNNWs suggested promise for these materials as field emitters.

Fundamental information on the field emission mechanism was obtained while studying the FE properties of AlNNTs.[31,141] AlN is an insulating, wide-bandgap ceramic material, so good FE properties were not expected. This was indeed true when the AlNNTs were grown on n-type silicon substrates. Hardly any emission current was observed. However, the FE properties were dramatically improved when the AlNNTs were grown on p-type silicon substrates. The best emission was obtained on $p^+$ silicon substrates with a turn-on field of 6 V/$\mu$m. A maximum emission current density of 0.22 A/cm$^2$ was obtained at a field of 10 V/$\mu$m. This phenomenon was explained with the help of an Si-AlN heterojunction band structure. The band diagram clearly showed a potential barrier at the n-Si-AlN interface that prevented electron transport required for the FE, whereas there was a clear potential well as a result of band alignment at the p-Si-AlN interface that encouraged electron transport across the interface. This phenomenon, of a better FE from wide-bandgap materials when grown on p-type substrates, and low-bandgap materials grown on n-type substrates, was put forward by Chang et al.[142]

Compared to GaN or AlN, InN in NTs structure exhibited exceptionally superior field emission properties, as observed by Wang et al.[143] Single-crystalline, well-aligned, and unidirectional InNNTs were fabricated through a dry-etching process, on MBE-grown InN(0002)/AlN(0002)/Si(111) substrates, with an $Ar^+$ plasma system. These InN nanoemitters with a density of $\sim 10^7$ cm$^{-2}$ showed excellent FE properties with a turn-on field (in this case defined as voltage required for an emission current density of 1 $\mu$A/cm$^2$) as low as 0.9 V/$\mu$m, which is lower by almost one order compared to single-crystalline and polycrystalline nanostructural forms of InN.[144–146] In addition to the geometry of NTs that will affect the enhancement factor ($\sim$69,000), the low turn-on field represents lower electron tunneling barrier as a consequence of the downward band bending near the InN surface caused by the surface electron accumulation layer and the inherent degeneracy of the InN semiconductor with Fermi-level lying above the conduction band minimum.

### 9.1. Photoconductivity

Photoconductivity (PC) in 1D group III-nitrides has also drawn research interest, particularly in the application of photodetectors. GaN showed great potential for UV detection for wavelengths $\leq$365 nm, due to their primary direct bandgap ($E_g$) of 3.4 eV. An additional advantage with GaN is that the $E_g$ can be modulated over a wide range depending on its alloy formation with InN, thus leading to devices with different cutoff wavelengths. Although study on PC of GaNNWs was reported recently,[147,148] PC for GaN epilayers has been an interesting academic issue for many years.[149–151]

Han et al.[147] have first revealed the promising candidature of a single GaNNW for nanoscale UV light sensors. The thermal CVD-grown NW in FET structures exhibited a substantial photocurrent upon UV light exposure (Figure 34a), along with the selectivity between two different UV wavelengths of 365 and 254 nm. The enhancement in zero-bias conductance from 23.4 to 258.3 nS under the illumination of 365 and 254 nm UV light, respectively, is attributed mainly to the larger photogenerated carriers by the latter having 4.88 eV energy. The effect of bias (gate) voltage, $V_g$, on PC (Figure 34b) reveals that the latter is mainly dominated by the increase in carrier concentrations, as evident from the increase in threshold voltages. The change in mobility has a rather limited role because no difference could be observed in the slopes (linear sections) of $I - V_g$ curves. The single NW exhibited great reversibility in PC activity (Figure 34c) with extremely fast response (81.9% of the saturation value within 2 s) and recovery time. The advantage of using quasi-1D structure of NWs has been realised in Figure 34d, where GaNNWs showed pronounced polarization anisotropy of conductance. The anisotropy arose because the incident electric field perpendicular to the NW-axis would be effectively attenuated due to the confinement in the radial direction of the GaNNW with diameters ($\sim$15 nm) much smaller than the excitation wavelength (254 nm). In contrast, electric fields parallel to the NW axis can be readily adsorbed because no confinement exists along this longitudinal direction.

In 2004, Kang et al.[148] reported the PC study on a bundle of as-synthesized GaNNWs, which exhibited the "persistent" photocurrent similar to what was observed in various GaN epilayers.[149–151] It is interesting to note that this study contradicted the observation of fast photoresponse on 15-nm thin GaNNW reported by Han et al.[147] The device, an ensemble of as-synthesized GaNNWs on the alumina substrate with Ti-electrodes, exhibited ohmic characteristics both in the dark and under UV light.[148] Despite the GaNNWs length (20 to 70 $\mu$m) being too short to connect directly to the pair of Ti-electrodes (with a $\sim$1-mm separation), a significant dark current and photocurrent could be observed, and the substrate was confirmed to be electrically insulated. Dark current (of the order of mA) was observed to be significantly high in magnitude compared to GaN epilayers (in the order of 0.1 nA).[152] In addition, both dark current and photocurrent exhibited temperature invariance, in contrast to the strong temperature-dependent conductivity observed for GaN epilayers.[153] The observations would imply the presence of degenerate electronic states in the NWs. Such degeneracy in NWs was expected to lead to the electrical networking of GaNNWs bundle, which allows electron transport from one NW to another between the electrodes.

The photoresponse spectra revealed the persistent phenomena: upon exposure to the light, the photocurrents slowly increased (rise duration: $\geq$2,000 s), and when the light was turned off, the photocurrents decayed for at least one day. The photocurrent decay was found to be more rapid in air than in vacuum. By correlating the PC behavior with PL spectra, Kang et al. found that the photoresponse characteristics of GaNNWs were similar to the green-band luminescence (GL), rather than the yellow-band emission (YL).[149–151] The latter has been attributed to

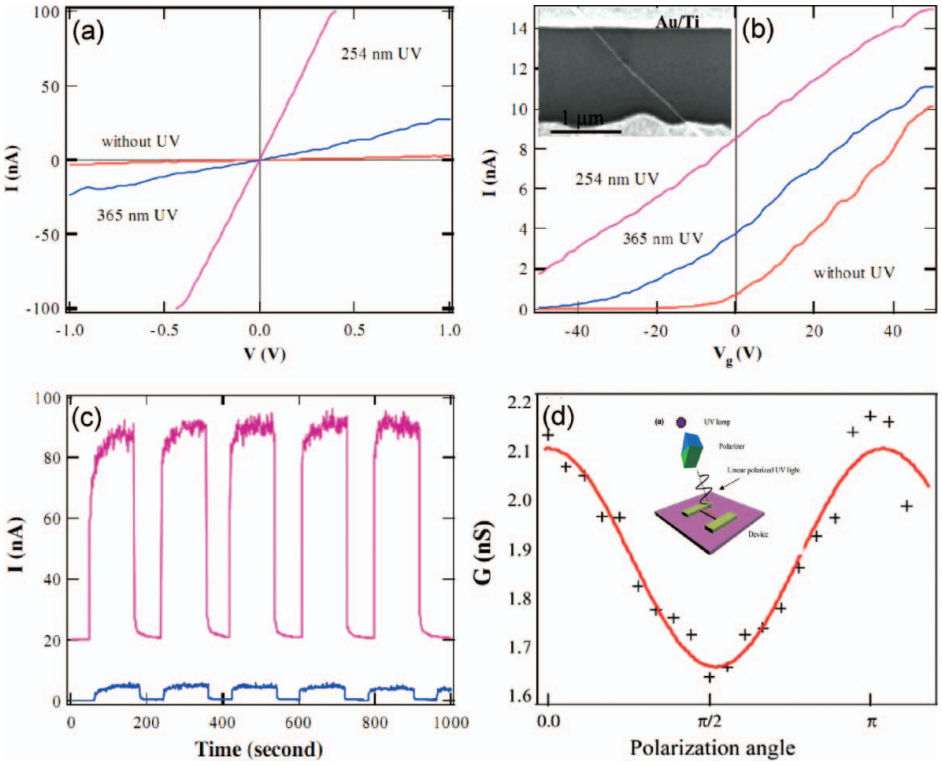


FIG. 34. (a) I − V curve of single GaNNW before and after exposed to 254 nm and 365 nm UV light, at zero-bias (gate voltage, $V_g = 0$). (b) I − $V_g$ curve at fixed drain source bias V = 0.1 V. Inset: SEM image of a GaNNW transistor, showing an NW (diameter = 15 nm) contacted by two Au/Ti electrodes (source and drain) with a channel length of 2 $\mu$m using Si substrate as a back gate. (c) Current vs. time (V = 0.1 V and $V_g = 0.1$ V) with UV light repeatedly turned on and off. The red curve (offset by 20 nA) is measured with illumination of 254 nm UV, and the blue curve corresponds to 365 nm UV light. (d) Photoconductance vs. polarization angle ($\theta$) under UV illumination (254 nm): the dots are experimental data and the solid curve is a fit following a function of $\cos^2\theta$. Inset: Schematic of the experimental setup for polarization anisotropy measurements. (Reprinted with permission from Han et al.[147] Copyright 2004 Elsevier.)

intrinsic structural defects and is commonly suggested as an origin for the well-known persistent photocurrent observed in GaN epilayers. The morphology study could not reveal any noticeable dislocations or grains in the free-standing NWs, and the observation of GL characteristics suggested its origin could be the nitrogen vacancy–related complex existing near or on the surfaces of NWs, which also could be responsible for the persistent behavior of photocurrent.

The persistent photocurrent has also been reported by Calarco et al.[154] in an investigation on MBE-grown GaNNWs, which exhibit anomalous dimension-dependent characteristics. The study established a model based on the effect of surface Fermi-level pinning and its interplay with the NW dimensions on the electron-hole recombination behavior in PC through these wires. From the I–V characteristics, they observed that post-UV illumination, the relatively thick wires (diameter, d = 500 nm) exhibited a photocurrent ($I_p$) higher than the dark current ($I_d$) by an order of magnitude, which decayed after switching off the light but still retained approximately double the $I_d$ value (in $10^{-5}$ A range) after 120 s (Figure 35a). This persistent photocurrent was observed for all the NWs with d > 100 nm. In contrast, thinner NWs with d < 100 nm exhibited no persistent photocurrent effect, similar to that observed by Han et al.[147] on 15-nm thin GaNNW. The general pattern of size-dependent photocurrents (Figure 35b) clearly exhibits a kink in the fitting curve at ~85 nm, indicating a critical diameter $d_{crit}$. For thicker wires ($d > d_{crit}$), the photocurrent is proportional to the NW-diameter, whereas those below $d_{crit}$ exhibited a sharp but exponential decrease in the photocurrent.

Previous photoemission spectroscopy studies[155] on GaN surfaces revealed surface Fermi-level pinning (at about 0.5–0.6 eV below the conduction band edge, $E_C$) within the forbidden band. As a consequence, the electronic bands are bent upward at the surface of GaNNWs, exhibiting a depletion space charge layer at the surface (Figure 36a). Electrons prefer to move to the core and holes toward the surface. The effect of surface depletion was evident from the $V^2$ to $V^3$ dependence of $I_d$ (vs. bias voltage). This is the characteristic for space charge–limited currents in

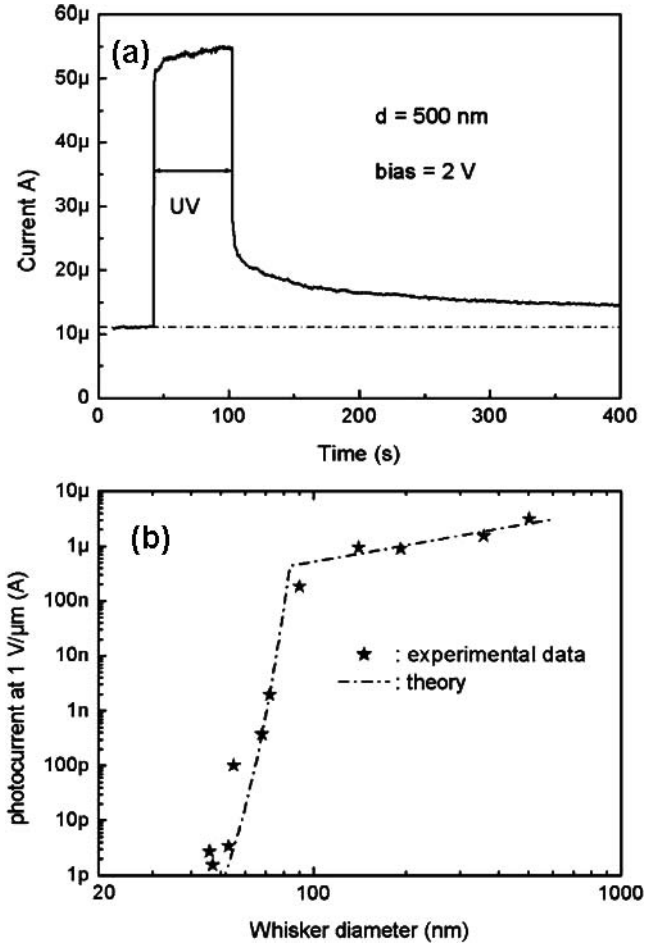


FIG. 35. (a) I-t characteristics of individual GaNNW: Current transient after 1 min of UV illumination (∼15 W/cm$^2$) of NW with diameter 500 nm at a bias voltage of ∼2 V. (b) Photocurrent versus NW diameter (d): the kink (∼85 nm) in the fitting curve indicates the critical diameter $d_{crit}$, where the surface depletion layer just completely depletes the NW. (Reprinted with permission from Calarco et al.[154] Copyright 2005 American Chemical Society.)

insulators. Assuming an n-type background doping in the $10^{17}$ cm$^{-3}$, the depletion space charge layers should have extensions of 50 to 100 nm into the bulk. For $d > d_{crit}$, NWs would have a tight open conducting channel (right image, Figure 36a), providing easy access for spatial separation of photoexcited electrons and holes. The recombination of nonequilibrium carriers would thus be reduced or may even be impossible if recombinations via surface traps in the forbidden band dominate, and hence the effect of a persistent photocurrent would be obvious for thick NWs. A decrease of the NW diameter (from right image to middle one, Figure 36a) would lead to the complete depletion, with unchanged surface barrier height Φ for electrons. Down to the $d_{crit}$, the recombination rate and hence the photocurrent would not change significantly. Further shrinkage ($d < d_{crit}$) would cause less band curvature and therefore a reduction in the barrier for surface electron-hole pair recombination (left image, Figure 36a). The recombination process becomes strongly enhanced and the photocurrent decays strongly with decreasing Φ; i.e., with decreasing NW diameter.

In a subsequent report, Cavallini et al.[156] revealed the presence of an exponential tail below the energy gap, in the UV spectral region, and its strong dependence on the NW diameter for GaNNWs by surface photovoltage spectroscopy (SPS) and spectral photoconductivity (SPC) measurements. The absorption tail may be due to structural disorder, defects or impurities, doping fluctuations, as well as broad excitonic, phononic, or plasmonic absorption or the presence of a strong electric field (Franz-Keldysh effect).[157–159] Because the free-standing NWs are near perfect crystals, the tail may not be due to defects or disorders. As a matter of fact, the specific energy of the band tail (∼0.1 eV) and its diameter dependence (increasing with d) for GaNNWs with low carrier concentrations ($10^{17}$ cm$^{-3}$) can only be explained by the Franz-Keldysh effect due to the internal electric field in the depletion region induced by Fermi-level pinning at the NW surface. Under a constant electric field, the free electron wave function modifies into an Airy function, which exponentially decreases in the bandgap region. As a result, a sub-$E_g$ optical absorption occurs, which can be interpreted as a photon-assisted tunneling through the forbidden band region (Figure 36b). The experimental values of the band tail energy, $\Delta E$, are in good agreement with the results obtained by simulating the electric field in the depletion region of the NW surface using a cylindrical model (Figure 36c). For wires with $d > d_{crit}$, containing a tight core conductive channel, the barrier Φ is equal to the Fermi-level pinning energy relative to the unperturbed conduction band, whereas for $d < d_{crit}$, because NWs are completely depleted, Φ decreases with d (Figure 36a), as evident from the sharp fall of $\Delta E$ below $d_{crit} = 80$ nm (Figure 36c).

In spite of several reports on PC studies on GaNNWs, quantitative studies of photocurrent gain (Γ) values, its underlying mechanism and related advantages for 1D nanostructures were not found until recently. The Γ in a photoconductor is one of the most important physical parameters related to photocarrier collection efficiency. GaN thin-film materials have been reported to possess high Γ[160,161] and good responsivity.[162–164] Chen et al.[165] first reported an ultrahigh Γ in GaNNWs, which exhibited distinct characteristics unmatched by their thin-film counterparts. The quantitative results on a single thermal CVD-grown GaNNW, with m-directional long axis, revealed an onset in the photocurrent response at around 3.2 eV. The photocurrent generation efficiency of the NW photodetectors, and hence the Γ value, estimated from PC spectrum utilizing the defined parameters like photon energy, incident intensity, and effective illuminated area was found to be related to the wire diameter (d), as shown in Figure 37a. For comparison, the Γ values of GaN film–based photoconductors measured under similar conditions were also depicted. The NWs (d ∼ 40–135 nm) exhibited Γ values ($5.0 \times 10^4$ to $1.9 \times 10^5$) that are significantly higher than

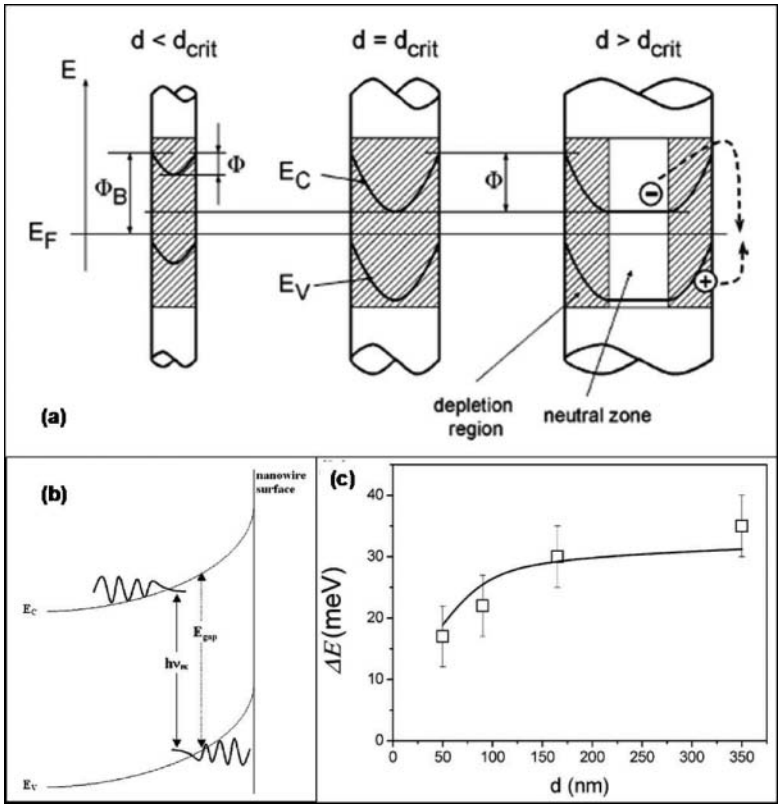


FIG. 36. (a) Schematic diagram of proposed model: dependence of depletion region (shaded), shape of conduction ($E_C$) and valence band ($E_V$) edges, and recombination barrier ($\Phi$) on the nanowire diameter (d). Barrier height $\Phi_B = \Phi + (E_C - E_F)$. Right: the surface recombination mechanism of the photoexcited carriers. (b) Schematic band structure of an n-type semiconductor surface: the wave function of an electron in the conduction band and a hole in the valence band are characterized by tails in the forbidden band gap induced by the internal electric field (Franz-Keldysh effect): the band-to-band transition occurs at energy lower than the energy gap. (c) The simulated values of Franz-Keldysh band tail widths $\Delta E$ as a function of d: the experimental data (?) obtained from PC spectra. (Reprinted with permission from Calarco et al.[154] and Cavallini et al.[156] Copyright 2005, 2007 American Chemical Society.)



their thin-film counterparts ($5.2 \times 10^1$ to $1.6 \times 10^2$). Moreover, a size effect was also observed. As d increased from 40 to 100 nm, $\Gamma$ increased and reached a maximum. Beyond d $\sim$ 100 nm, $\Gamma$ did not further increase but decreased slightly.

The phenomenon of high $\Gamma$ in GaN films[162,163] has been attributed to the presence of hole traps that prolong the lifetime of excess carriers. On the other hand, Munoz et al.[160] and Garrido et al.[161] have held the strong surface band bending in GaN responsible for the localization of the excess carriers and hence the resultant long lifetime and high $\Gamma$. In 1D NWs, the high surface-to-volume ratio could lead to significant spatial separation of charge carriers and surface band bending (SBB) effects.[154] Though the influences of hole traps are difficult to neglect,[166] from the logarithmic plot (Figure 37b), the intensity(I)-dependent behavior of $\Gamma$ revealed a clear inverse power law ($\Gamma \propto I^{-0.9}$) in the intensity range of 0.75–250 W/m$^2$. The power (k) value in the range $k = 0.8$–$0.9$ indicates strong carrier localization effect induced by the electric field arising due to the spatial charge separation.[160–161] In contrast, the contribution of traps could be identified by the independency of $\Gamma$ on $I$ under low-level excitation.[162,163] However, for a small I (<40 W/m$^2$), $\Gamma$ follows an inverse power law, $\Gamma \propto I^{-k}$, with k = 0.5. Hence, the observation (Figure 37b) strongly suggests a surface-dominant rather than trap-dominant high $\Gamma$ mechanism in GaNNWs.

Chen et al. observed persistent PC for NWs with d $\leq$ 40 nm,[165] and Calarco et al.[154] observed the same phenomena only for thick MBE-grown GaNNWs ($d \geq 100$ nm). Although the accurate reason for this discrepancy could not be identified, two probable factors have been proposed:[165] (1) The dark conductivity ($\sigma$) for the GaNNWs grown by the CVD process ranged from 10 to 1,000 $\Omega^{-1}$ cm$^{-1}$,[135,136,167] implying a higher carrier concentration (n) at $10^{18}$ to $10^{20}$ cm$^{-3}$, which is reportedly higher than that (n = $10^{17}$ to $10^{18}$ cm$^{-3}$) for the MBE-NWs.[154] Hence, an approximate width ($w \propto n^{-1/2}$) of surface depletion region would be less (w = 10–30 nm) for

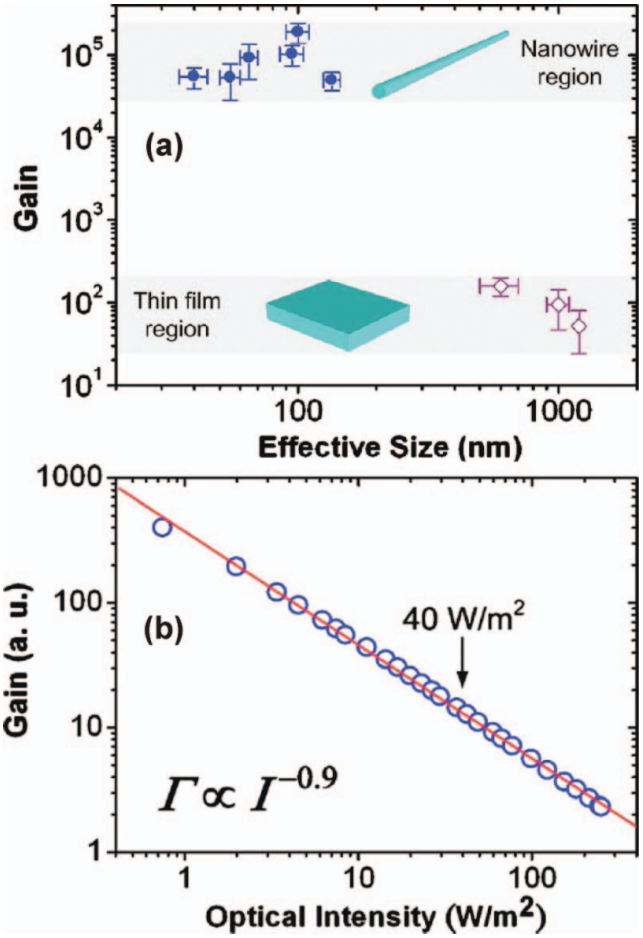


FIG. 37. (a) The photocurrent gain as a function of effective size for the GaNNWs (diameter, blue solid circles) and thin films (thickness, open purple diamonds) at 400 V/cm applied field and 4.0-eV excitation with 10–12 W/m$^2$ power density. Three data points of thin-film photoconductors are obtained from Munoz et al.[160] (size at 600 nm), Chen et al.[165] (1,000 nm), and Shen et al.[164] (1,200 nm). (b) The optical intensity–dependent gain of the GaNNWs at 325-nm excitation and bias of 1.0 V. The red solid line shows a fitting to the power law $\Gamma \propto I^{-k}$, revealed with $k = 0.9$. (Reprinted with permission from Chen et al.[165] Copyright 2007 American Institute of Physics.)

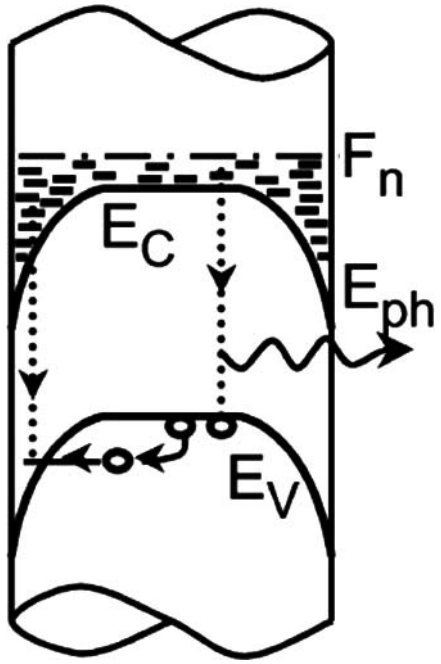


FIG. 38. Schematic band diagram illustrates the carrier recombination by thermal activation and tunneling into the accumulation layer of the InNNW surface ($E_C$ and $E_V$ are conduction and valence edges, $F_n$ is the Fermi level in the conduction band). (Reprinted with permission from Stroica et al.[170] Copyright 2006 American Chemical Society.)

CVD-grown NWs[165] compared to the MBE-NWs (w = 50–100 nm), assuming similar Φ ( = 0.5–0.6 V).[154] The narrower w of the CVD-NWs probably explains the contrast in size-dependent PC behavior with those grown by MBE. This also explains why Han et al.[147] could not observe any persistent photocurrent for the d = 15 nm thin CVD-NW because those are completely depleted with d < w ( = 10–30 nm). (2) In addition, typical CVD-NWs always reveal m- or a-axial orientation, which is strikingly different from the c-axial MBE-NWs; such contrast might also provide a probable surface polarity effect on the PC behavior of NWs. Nevertheless, the study by Chen et al.[165] clearly showed the importance of growth techniques even if they follow the same growth mechanism (e.g., VLS) for NW growth.

Instead of the usual depletion layer observed on most semiconductor nanostructure surfaces, an intrinsic electron accumulation layer could be found on InN surfaces[168] that pins the surface Fermi level at 0.5–0.9 eV higher than the conduction band.[169] This accumulation layer, though only few nanometers thick,[170] significantly influences the properties of the 1D InN. As usual for narrow bandgap semiconductors, the electron accumulation layer at the InNNW surface leads to a significant downward band bending,[170] which is just opposite to what was observed for GaNNW.[154,165] Optoelectronic properties of InNNWs revealed the effect of the narrow $E_g$ and surface accumulation layer.[170–174] The first report on optoelectrical properties of InNNWs[173] demonstrated generation of IR emission through impact excitation under a high applied electric field. Photogenerated holes in the valence band can be thermally activated over the lowered potential barrier (due to band bending) and recombine with the high-density electrons at the surface accumulation layer (Figure 38), contributing to the low-energy tail in PL spectra. Nanodevices using individual single-crystalline InNNWs also exhibited temperature-dependent conductance with thermal activation as the dominating transport mechanism.[171,174]

Lee et al.[174] demonstrated the performance of a photocurrent generation device using InNNWs. A sandwich-type photoelectrochemical cell was assembled with an acceptor-sensitized dyad with di-(3-aminopropyl)-viologen (DAPV) and an Ru complex ($RuL_2(NCS)_2$) on an InNNWs/ITO plate and Pt-sputtered ITO substrate. The $RuL_2(NCS)_2$ could generate photocurrent, exhibiting fast response, under white light illumination (100 mW/cm$^2$). The study revealed that, in presence of InNNWs layers (DAPV/InNNWs/ITO cell), the photocurrent could be enhanced significantly by 62.7% compared to the DAPV/ITO cell (without InNNWs). The InNNWs layers could improve the charge collection by minimizing the charge recombination process.

## 10. MECHANICAL PROPERTIES

AlN (0001) bulk hardness is around 17.7 GPa and exceeds those of GaN (0001) or InN (0001), which are 10.2 and 11.2 GPa, respectively.[175] A temperature dependence of hardness of the group III-nitride materials has been presented.[175] However, mechanical hardness measurement in nanostructures is a tough task given the dimension of the indentor, which is nearly always larger than the nanostructure being measured. Molecular dynamic simulations or ab initio and first principle calculations have been carried out to understand the mechanical response in metal NWs and III-nitride materials.[176–178] Mechanical properties of NWs were also measured by mechanical resonant methods,[179,180] atomic force microscopy-based methods,[181–183] and nanoindentation methods.[184] But each of these techniques has problems of its own and extraction of hardness data is nontrivial. Recently there was a report on the hardness of GaNNWs by the indentation method.[185] These GaNNWs were prepared on sapphire substrates and were 20–50 nm in radius. A single NW was placed on a silicon substrate by an FIB Omni probe (Omniprobe, Inc., USA). A nanoindentor XP (Agilent Technologies, USA) with Nano Vision scanning force microscope was used to image the NWs (Figure 39a). A Berkovich tip was used to do the indentation measurements. To prevent any movement of the NW while scanning, the ends of the NW were fixed to the substrate by a deposition of Pt using FIB. The indentation of the NW may be modeled as that shown in (Figure 39b) for small indentation depths. The indentation of the NW is a dual contact situation under an applied force P, where contact 1 is an elliptical between the spherical indentor and the cylindrical NW and contact 2 is a receding contact between the cylindrical NW and the elastic half space of the substrate (Figure 39b). The cylinder is expected to recede from the half space when the load is applied on the indentor. The two contacts are in series and hence an equivalent contact stiffness (S) is given by

$$1/S = 1/S_1 + 1/S_2 \qquad [16]$$

where $S_1$ and $S_2$ are the contact stiffness for contact 1 and contact 2, respectively. With these formulations a model was developed to analyze the indentation data because the conventional Oliver-Pharr method was not suitable in the nanomaterials case. The hardness of the GaNNW was found to be 46.7 $\pm$ 5.6 GPa, which is much higher than the corresponding ZnONW hardness of about 3.4 $\pm$ 0.9 GPa. This work is a significant step forward in the measurement of the mechanical properties of NWs, but validation of data on several other systems is required for reliability and repeatability.

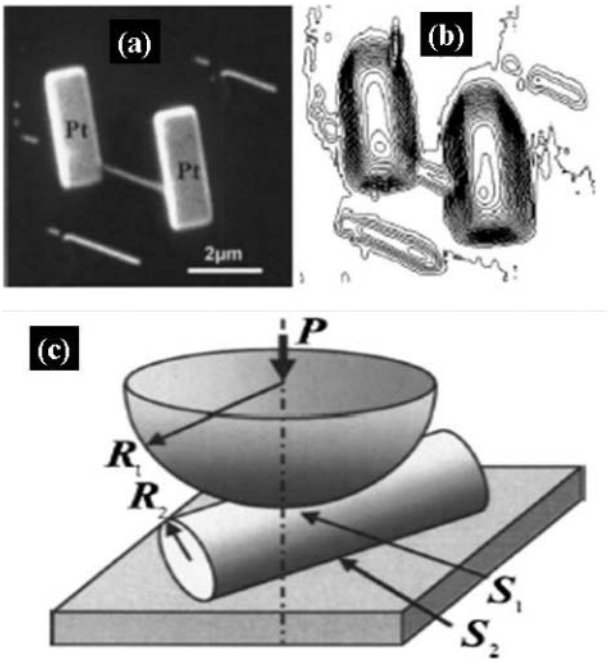


FIG. 39. Typical SEM image for a fixed GaNNW on an Si substrate by Pt deposition; (b) the corresponding scanning force microscopy contour image scanned by a Berkovitch indentor (10 nm/contour). (c) The schematic of the indentation of an NW on a substrate (half space). For very small indentation depths the indenter can be modeled as a spherical indenter. (Reprinted with permission from Feng et al.[185] Copyright 2006 American Institute of Physics.)

## 11. APPLICATIONS

Several applications, most prominently LEDs, of the group III-nitride materials, in general, have been reviewed.[186,187] The role of defects on the properties of these materials and how they can be utilized in devices have also been reported.[8,21] Several reviews have described the FETs using this class of binary or ternary compounds.[188–191] But reviews on applications of one-dimensional group III-nitride materials have been scarce.[57,192] This section will discuss primarily sensing applications and nanoscale LEDs of these materials as an addition to what has already been described in other reviews or books.

### 11.1. Nanoscale Sensors

The sensing principle is based on modifying various properties, optoelectronic, physical, or chemical, of a material M by

the addition of an external agent A and then determining or in some cases quantifying the changes with respect to the pristine material by suitable technique. For example, the electrical resistance R of M can be changed, preferably in a uniform manner, by the chemical adsorption/absorption of an external molecule A with uniform variation in concentration (c). If the change in the differential resistance ($\Delta$R) is specific to *A*, the molecule is identified. The amount absorbed/adsorbed on the pristine material is obtained from the plot of *R* as a function of *c*. Optically, we may probe the shift of the luminescence band characteristic of *M* upon chemisorption of A to sense the presence of A. A can also trigger the appearance of an altogether new luminescence signal whose intensity might be calibrated with the intensity of the luminescence band. One classic example of electrical sensing may be the modification of the gate electrode of a planar FET (described in Section 9) with molecular receptors or selective membranes that can bind to specific analytes. Binding of the charged species A will result in the depletion or accumulation of charge carriers in the FET that can be directly monitored from the change in conductance. Nanomaterial-based sensors are being developed using particles, tubes, and wires.[193–195] Not limited to group III-nitrides, the NW-based sensors have a direct advantage over the planar sensors. Owing to the large surface-to-volume ratio, the NWs offer much higher attachment sites, which in turn increases the sensitivity of the device often to the tune of single molecule detection. High density of NW sensor arrays could be incorporated in a chip device. Lastly, the 1D elements of the sensor offer the least invasive of the in vivo sensing techniques. However, there are concerns: (1) separating single NP or NW and establishing an electrical contact is a gargantuan work, (2) single nanomaterial-based sensors suffer from a low signal-to-noise ratio, (3) a nanomaterial sensor may fail (sensor fouling) if the agent to be sensed is in the overwhelming micrometer size. Work is in progress to use arrays or assemblies of nanomaterials to increase the reliability of the sensing process.

A hybrid structure made from AuNPs-decorated GaNNWs has been used for methane and $N_2$ sensing.[196] The GaNNWs were made by a conventional catalyst-assisted thermal CVD setup at 950°C using Ga pellet and $NH_3$. The random GaNNWs form a 10- to 20-$\mu$m-thick mat on the sapphire substrate. Five-nanometer AuNPs were deposited on the GaNNW mat by PECVD. The schematic of the sensor device is shown where the gold wires are 25 $\mu$m thick and separated by 1 mm (Figure 40a). The entire device is sandwiched between two 10-mm glass plates. After ensuring an ohmic contact, the device was exposed to different gaseous environments of Ar, $N_2$, and methane. Without AuNPs, the GaNNW mat demonstrated a linear ohmic behavior insensitive to the environment, but with the Au particles the I–V is nonlinear with a drop of 5 orders in the current value (Figure 40b). This suggests that the AuNPs do not offer the primary transport path in the device. The I–V for the Au coated GaNNW mat is now sensitive to the environment. The I–V curves in presence of $N_2$ and Ar, although identical,

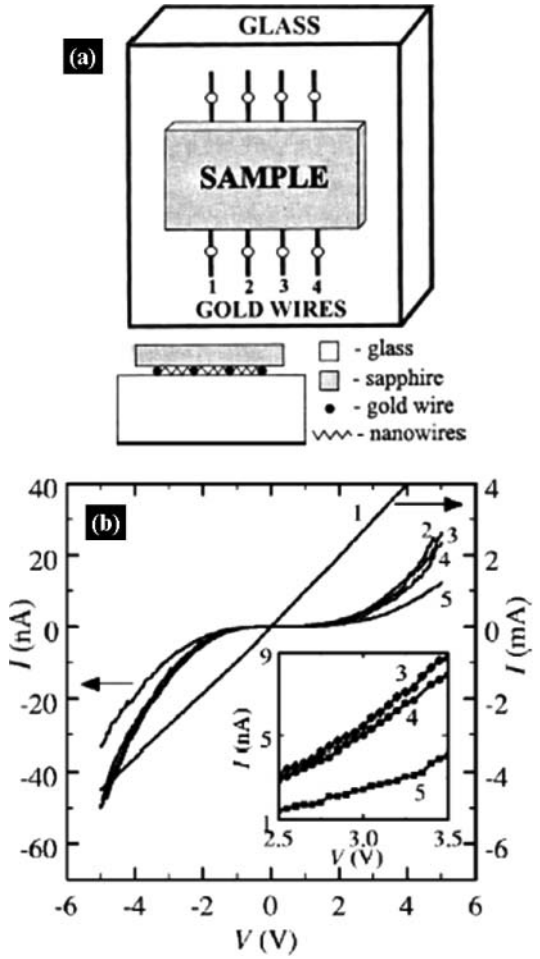


FIG. 40. (a) A schematic of the gas sensor constructed from a mat of GaNNWs. (b) Current-voltage curves of a sensor constructed from bare GaNNWs (curve 1; right-hand vertical axis) and a sensor constructed from AuNPs decorated GaNNWs (curves 2–5; left-hand axis) for in vacuum (2) and atmospheres of Ar (3), $N_2$ (4), and methane (5). The inset is an expanded view of the I − V data in the first quadrant (♦– vacuum, •– $N_2$, ■– methane). (Reprinted with permission from Dobrokhotov et al.[196] Copyright 2006 American Institute of Physics.)

deviate from that observed in vacuum. The most reactive gas—methane—however, produced a large response. As the methane pressure fell below $10^{-6}$ Torr, the signal returned back to its original vacuum condition, proving that the device response is reversible. The device is regenerative because the adsorbed gases could be easily desorbed by thermal heating. The sensing mechanism is still based on conductance of the device in a manner similar to the NW FETs described in the earlier section. The sensing mechanism can be visualized as follows (Figure 41): the conducting channel of the intrinsically n-type GaNNW is reduced as the AuNP is formed on its surface (Figure 41a). Charge transfer across the Au/GaN interface, required to have the Fermi-level alignment, will create a depletion region within

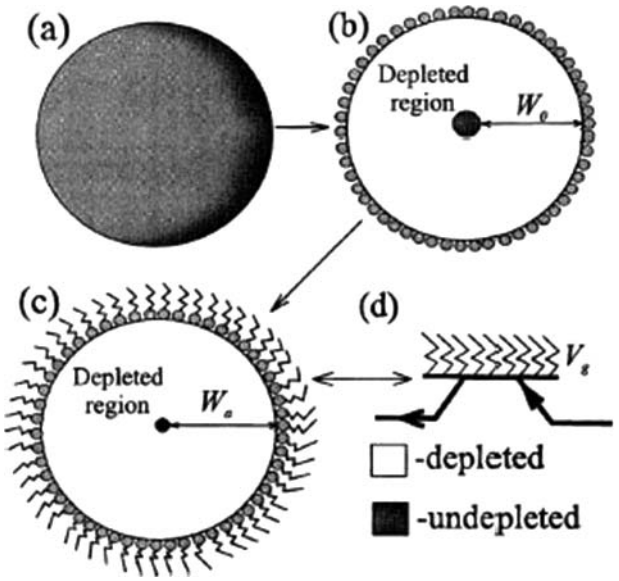


FIG. 41. A cross-section view of an NW showing the size of the conducting region (grey) with no AuNP on the surface (a), with a layer of AuNPs on the surface in vacuum (b), with gas physisorbed on the surface of the NPs (c), and an equivalent circuit diagram representative of the operation of the NW as a gas-sensitive FET with $V_g$ representing the induced potential by the absorbed molecules. $W_0$ is the depletion depth due to just AuNPs on the NW surface and $W_a$ is the depletion depth when gas molecules have been physisorbed onto the AuNPs. (Reprinted with permission from Dobrokhotov et al.[196] Copyright 2006 American Institute of Physics.)

the NW and the conducting channel in the GaNNW will shrink (Figure 41b). This will lower the current drastically as observed. Physisorption of the gases on the Au NP will induce a negative potential (similar to a gate voltage in FET), which will further increase the depletion layer thickness and reduce the conductance (Figure 41c).

Substrate-supported GaN layers can also serve as H-sensors.[197] Here a vertical diode structure of Pt-GaN was used and the I–V characteristics of the diode were measured in the presence of $H_2$. Different concentrations (10–500 ppm) of $H_2$ in $N_2$ were used and change in the forward bias (0.5 V) current was monitored. The percentage change of current was more in the Pt-GaN diode compared to Pd-GaN diode probably because of the higher catalytic activity of Pt. GaN resistive gas sensors were also reported, using a 2-$\mu$m-thick silicon-doped GaN epilayer grown by organometallic VPE on sapphire substrates.[198] Planar metallic contact pads placed at separations of 0.5 and 1.0 mm were deposited by e-beam (Ti) and thermal (Al, Au) evaporation. An ohmic contact was ensured. The current was measured after passing a mixture of $H_2$ in Ar with pure Ar forming the reference point. The differential current ($\Delta$I) at a constant DC bias of 2 V and at 50°C measuring temperature was plotted as a function of time for a pure $H_2$ flow. $\Delta$I increased with the $H_2$ pulses and decreased without it, showing the sensing behavior. A similar result exists for AlN thin films in sensing $H_2$.

Detection of hydrogen has also been demonstrated via change of resistance in an ensemble of thermal CVD-grown GaNNWs on Si substrates.[199] Both the uncoated and Pd-coated GaNNWs were found to detect $H_2$ at concentrations from 200 to 1500 ppm (in $N_2$) at room temperature, although the latter demonstrated improved sensitivity by a factor of ~10 at low concentrations (Figure 42a). The Pd-coated GaNNWs showed relative resistance change, from ~7.4% at 200 ppm to ~9.1% at 1,500 ppm $H_2$ in $N_2$ ambient. Upon removal of $H_2$, almost 90% of the initial resistance value could be recovered within 2 min (Figure 42b). These sensors exhibited low power consumption (<0.6 mW) at 300 K, suitable for long-term applications. Study revealed that these sensors perform better at elevated temperatures. The adsorption activation energy of the sensor was estimated to be 2.2 kcal mol$^{-1}$ (0.097 eV), at 3,000 ppm $H_2$ in $N_2$, which is smaller

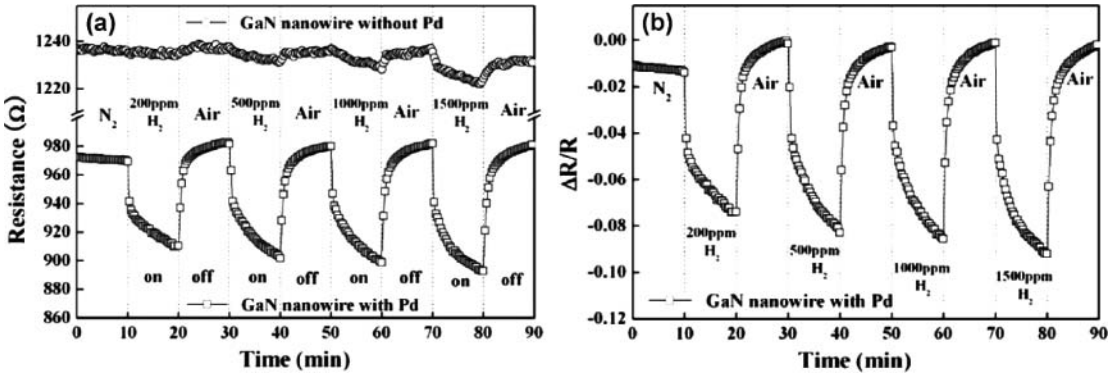


FIG. 42. (a) Room temperature hydrogen sensing: measured resistance at an applied bias of 0.5 V as a function of time from Pd-coated and uncoated multiple GaNNWs exposed to a series of $H_2$ concentrations for 10 min. (b) Relative response of the sensor at different $H_2$ concentrations (200–1,500 ppm) in $N_2$ ambient. (Reprinted with permission from Lim et al.[199] Copyright 2008 American Institute of Physics.)

than that (0.12 eV) of Pd-coated ZnONRs,[200] under the same operating conditions.

Following the sensitivity of GaN surface to $H_2$, pH sensitivity of GaN was also studied and reported.[201] GaN FET and AlGaN/GaN high-electron-mobility transistor (HMET) structures were used to measure the response of nonmetallized GaN gate regions to the pH of the electrolyte solution. These are also known as ion-sensitive field effect transistors (ISFET). Conventionally, the effect of the changes in the pH of the electrolyte on the sensing surface (GaN) is monitored by adjusting the gate voltage to compensate for the ion-induced changes in the channel current, $I_{DS}$, at a constant $V_{DS}$ ( $= 250$ mV).[201] The interface potential change (in mV) was found to be a function of pH yielding parallel straight lines, with a pH sensitivity between 56–57.3 mV/pH,[201] almost independent of the presence of native oxide on the gate surface. The GaN surface shows immediate response to the change in the pH and good stability of the channel current. Schottky diodes fabricated on GaN thin films also help in studying electromechanical response as a function of strain frequency and DC bias. These properties may well be extended to GaN nanostructures and application possibilities exist in these areas.

InN has strong surface charge accumulation properties, which stay within 4 nm of the surface and contribute to the lateral conductivity of the film. This surface charge is sensitive to the external environment and can be modulated by external agents. Twenty- to 80-nm thin films of InN grown on GaN buffer-coated sapphire substrates at 470°C by MBE have been used for sensing purposes.[202] Standard Hall patterns with Van der Pauw geometry were defined on the film using lithography and plasma etching. The sample surface was exposed to solvents for about 3 s via a cotton swab wetted with the solvent. The sample surface was then blow-dried with RT and hot air to take care of any temperature decrease due to solvent evaporation. Ex situ Hall measurements were then carried out with a small current of 0.1 mA. The sheet carrier density and room temperature Hall mobility both increase after treatment with water, methanol, and isopropanol (IPA) for different thicknesses of InN films compared to the equilibrium values (Figure 43). The increase in the carrier density (Figure 43a) and mobility (Figure 43b) result in the decrease in the InN sheet resistance after solvent treatment. The surface and bulk electrons have different Hall mobilities in the InN thin films, which is not assumed in the Hall measurement and hence the data are a weighted average. The reason for the larger intercept on the carrier density axis obtained by extrapolating the linear fit (dashed line) to a zero thickness of InN film for the treated sample compared to the untreated one suggests a larger surface charge. However, both the enhanced sheet carrier density and Hall mobility will decay in a time scale of several hundreds of minutes. Nevertheless, the applicability of the InN film in sensing has been demonstrated.

InNNRs for $H_2$ sensing were produced by hydride metalorganic vapor phase epitaxy on c-$Al_2O_3$ substrates by the reactions of TMIn, hydrochloric acid, and $NH_3$.[203] The InNNRs produced were sputter-coated with platinum to form a 10-nm thin film. Without the Pt, the InNNRs were ineffective for the sensing. This is probably due to the fact that Pt acted as a catalyst to dissociate $H_2$ to atomic H. Al/Ti/Au contacts were defined by a shadow mask and then sputter-deposited. Au wires were then bonded to the contact pads for electrical resistance measurements. The ohmic contact for the as-grown and Pt-coated InNNRs was confirmed from the linear current-voltage curves. The current and hence the relative resistance change (Figure 44) in the Pt-coated multiple InNNRs were seen to change with time when exposed to different amounts of $H_2$ (10–250 ppm) mixed in air at room temperature. The change in the relative resistance was small at the beginning of the $H_2$ exposure but then rapidly increased and ultimately saturated after about 15 min of exposure (Figure 44). The initial native oxide on the metal can retard its catalytic activity, which is regenerated by the removal of the

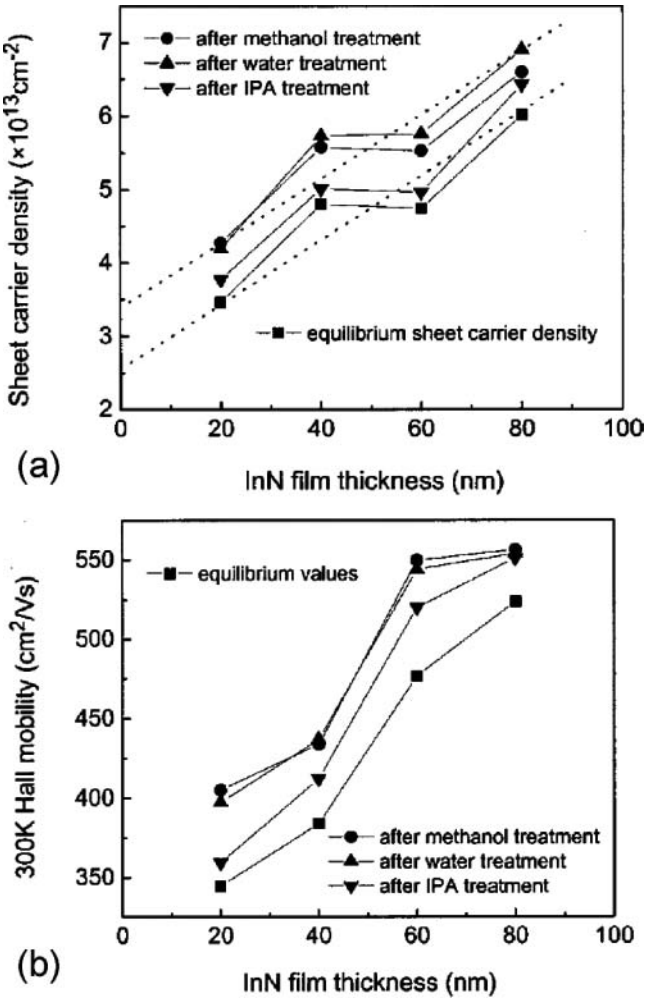


FIG. 43. Room temperature (a) sheet carrier density and (b) Hall mobility of a series of InN samples with different thickness before and directly after (3 min) methanol, water, and isopropanol (IPA) treatments. (Reprinted with permission from Lu et al.[202] Copyright 2004 American Institute of Physics.)

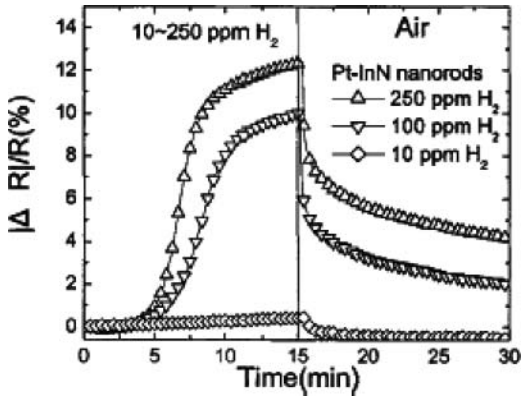


FIG. 44. Hydrogen test by Pt-InN nanorods: $|\Delta R|/R(\%)$-time plot at different $H_2$ concentrations (10–250 ppm). (Reprinted with permission from Kryliouk et al.[203] Copyright 2005 American Institute of Physics.)

oxide by the $H_2$. Again, after some time the Pt surface can be saturated with $H_2$ to level off the current or resistance change. After the removal of the $H_2$, the current dropped steadily at first and then slowly. The reversible chemisorption of reactive gases at the surface of nitrides can produce a large reversible change in conductance of the nitride.[204] Exchange of charges between adsorbed gas species and the surface resulting in changes of the depletion depth[205] or change of surface conduction due to gas adsorption/desorption[206] was believed to be controlling the sensing mechanism, though the mechanism in this case is not clear. Also, the Pt-coated InNNRs were seen to be insensitive to $O_2$.

Recently, hydrogen sensing at room temperature was also demonstrated using an ensemble of InNNBs grown on $SiN_x$-coated Si substrates by MOCVD.[207] Upon exposure to various concentrations of $H_2$ (20–300 ppm in $N_2$ ambient), InNNBs exhibited an increase in the relative resistance change from 1.2% at 20 ppm $H_2$ to 4% at 300 ppm $H_2$. The recovery of the initial InN resistance, upon the removal of $H_2$, was faster compared to single InNNR.[203] InNNBs catalyzed with Pd revealed higher relative response than Pt-coated ones.[208]

Biosensing is also an important area for clinical diagnosis, medicine, and bioengineering. Sensing single or a minute amount of biomolecules needs a perfect integration of the highly selective biorecognition with the unique electronic, photonic, and catalytic features of nanomaterials. Interestingly, biomolecular complexes, proteins, or nucleic acid fragments have nanometric dimensions comparable to the inorganic nanomaterials, whose inherent surface-dictated characteristics offer the opportunity for efficient binding or bio-functionalization and superb sensitivity in detecting them.[209–212] Though various materials, including metal, silicon, and II–VI semiconductors, have been used in nanobiotechnology,[209–221] the use of group III-nitrides, such as GaN, have been scarce,[222–224] though they are chemically robust, nontoxic, and biocompatible.

Initial studies[222,223] showed that GaN surface, even without any surface modification, could promote reasonably good neuronal cell attachment, differentiation, neuritic growth, and survival compared to Si, which is a common template for biochip application.[223] Figure 45 represents the behaviors of cerebellar granule neurons prepared from 7-day-old Wistar rats on GaN thin film. After incubation for 6 days on the n- (Figure 45a) and p-type (Figure 45b) GaN surfaces, neurons exhibited a dense fiber network displaying features of differentiation. In comparison, neurons cultured on Si (Figure 45c) or polystyrene surfaces (Figure 45d) showed scanty cell coverage of few immature neurons with limited branching. Clearly, GaN surface provides preferential cell aggregation, indicating stabilized cell-material interface and biocompatibility.[223]

A bio-semiconductor coupling requires efficient and direct transfer of charges between semiconducting templates and bioorganic layers. This depends on the alignment of the relevant electronic levels on both sides at the bio-semiconductor hybrid interface.[224] The study has pointed out that the classical semiconductors like Si and GaAs are not actually ideally suited for direct electronic charge exchange with bioorganic systems under physiological conditions, whereas the use of large bandgap semiconductors like GaN or AlN, or their alloys like AlGaN, which can cover the entire range of highest occupied molecular orbital (HOMO)-lowest unoccupied molecular orbital (LUMO) positions of those bioorganic systems (Figure 46), should be much more promising for bioelectronic applications.[224]

In spite of this, the potential application of group III-nitrides in biotechnology is quite limited and mainly constrained to their thin-film configuration. The promising candidature of group III-nitrides has been truly realized on the AlGaN/GaN heterostructures[222,224–231] that support the spontaneous formation of a two-dimensional high-density electron gas (2DEG) at the interface. For AlGaN/GaN high-electron-mobility transistors (HEMTs), the existence of a conducting 2DEG channel very close to the surface provides the efficient transduction of the surface adsorption of solution ions or charged biomolecules, making the device extremely sensitive to the ambient.[224–227] Few groups, mainly Eickhoff and Ren et al., have established an appreciable foundation for AlGaN/GaN based transistors in biosensing application; e.g., a readout device for selective ion transport across lipid membrane via transmembrane ion channels,[222] for sensing the catalytic activity of immobilized enzymes,[228] for the detection of protein adsorption,[229] for deoxyribonucleic acid hybridization,[230] or for binding of antigens with immobilized antibodies.[230,231] The chemical inertness and biocompatibility of GaN-based semiconductors provides an easy way to directly deposit lipid membranes or cell cultures on the gate surfaces of the FETs[222] or direct functionalization of surfaces via deposition of self-assembled organic monolayers and subsequent immobilization of biomolecules.[228,229] General practice is to functionalize the gate area with different organic linkers depending on the analytes and/or sensing applications.[225]

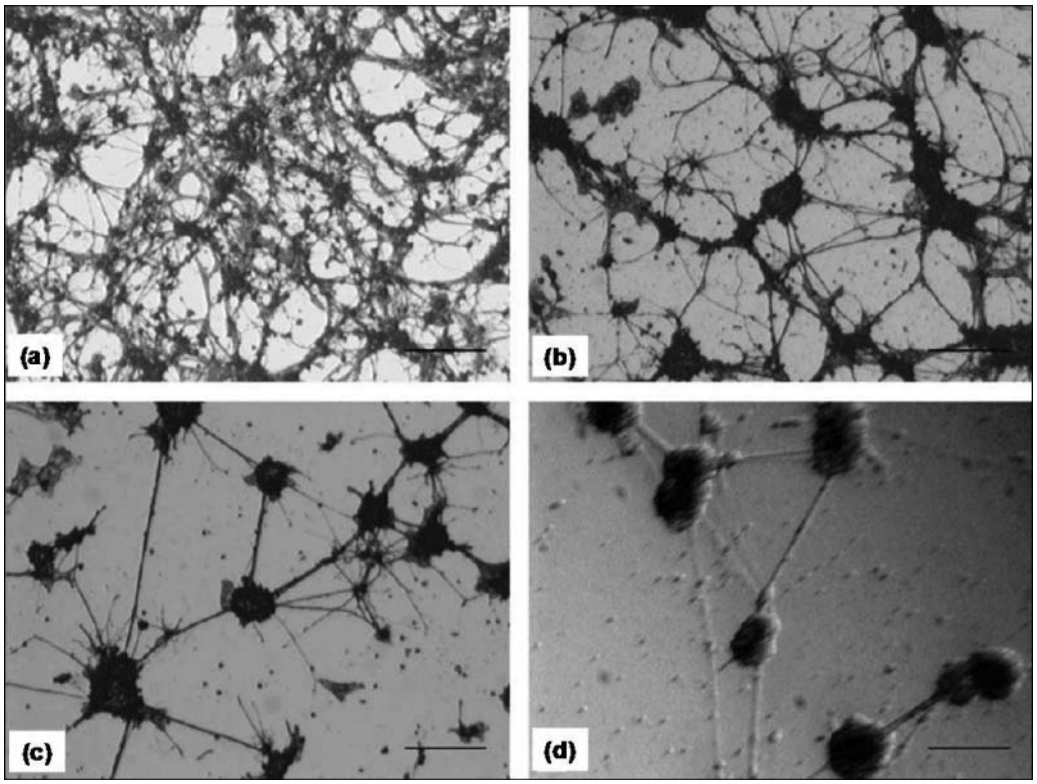


FIG. 45. Photomicrographs of cerebellar granule neurons cultured, after 6 days in culture, on (a) n-type GaN, (b) p-type GaN, (c) Si, and (d) tissue culture polystyrene plates (scale bar = 100 $\mu$m). (Reprinted with permission from Young et al.[223] Copyright 2006 Elsevier.)



However, some reports[230–232] state that the Au-coated gate could provide easier functionalization of biomolecules and a more reproducible result than using the native oxide on the GaN or AlGaN gate surfaces (Figure 47).

Tonisch et al.,[233] utilizing the high specific surface area of nanomaterials, have proposed a basic module for a novel NW-based and AlGaN/GaN-based nanoelectromechanical (NEMS) device. The device works via the mechanical coupling of NWs to the polarization-induced 2DEG of AlGaN/GaN FET. In a laminar flow system, the force applied to the NW decreases almost linearly toward the channel wall due to viscosity. Thus, a tensile and an equally compressive strain would exist simultaneously at the opposite sides of the fixation point of the NW, which in turn influences the piezoelectric polarization locally (Figures 48a, 48b). Hence, the deflection of free-standing NWs in a streaming liquid causes an additional strain in the AlGaN barrier, which leads to a change in the resistance of the 2DEG. Researchers [234,235] have demonstrated the unique advantage of nanomaterial-based AlGaN/GaN sensors for immobilization of enzymes that could retain their bioactivity due to the desirable microenvironment and the direct electron transfer between the enzyme's active sites. The huge difference in the isoelectric points of glucose oxidase and ZnONRs, directly grown on the gate region of AlGaN/GaN HEMTs, ensures a favorable electrostatic interaction between the two to enhance the limit of glucose detection[234] (Figures 48c, 48d).

However, 1D III-nitride nanostructures have not been utilized until recently in biosensors.[236–238] Surface-induced spatial charge separation (discussed before) in GaNNW leads to a higher surface conductivity compared to its naturally high resistive planar film counterparts. Interestingly, such surface specificity can provide an enhanced sensitivity to the ambient, and hence to the surface-immobilized biomolecules, where neighboring charges could alter the electronic behavior of NWs. Very recently, Chen et al. have successfully demonstrated a rationale for using GaNNWs for improved charge transfer efficiency and biobinding to enhance the sensitivity to surface-immobilized DNA molecules.[237,238] This study revealed the potential of GaNNWs to be an attractive material for dual-sensing (optical and electrical-based) applications.

For the requirement of stable and efficient DNA recognition interface/surface, it is preferable to have covalent binding rather than simple adsorption. GaNNWs surfaces can be chemically functionalized by self-assembled organosilane monolayers of MPTS (3-mercaptopropyl trimethoxysilane), which can provide covalent linkage between the probe ssDNA strands (pDNA) and the NW surface (Figure 49a).[237] Interestingly, such MPTS modification also significantly improves the electrochemical

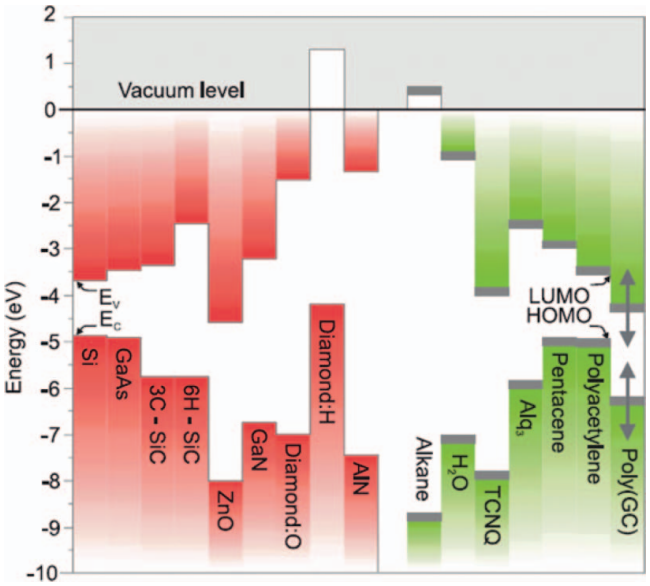


FIG. 46. A comparative study: reference values of the absolute positions of valence ($E_V$) and conduction ($E_C$) band edges for selected inorganic semiconductors, in comparison to the highest occupied (HOMO) and lowest unoccupied (LUMO) molecular orbitals of some organic materials (small molecules, polymers, and DNA). The data for water, as a common solvent in inorganic/organic hybrid heterojunctions, are also included. These data have been deduced from photoemission spectroscopy in conjunction with electronic transport, optical absorption, or luminescence measurements or have been calculated with state-of-the-art theoretical models (Stutzmann et al.[224] and the references therein). Typical error bars of both experimental and theoretical values are of the order of 0.5 eV. For the case of DNA as a prototypical biomolecule, largely varying results have been published, ranging from metallic to completely isolating characteristics, as indicated by the vertical arrows. (Reprinted with permission from Stutzmann et al.[224] Copyright 2006 Wiley-VCH Verlag GmbH & CoKG.)

characteristics of the GaNNWs.[238] The modified GaNNWs exhibit a wide potential window of 4.5 V with very low background current (Figure 49b). This is an advantage for the sensitive detection of surface-immobilized analytes,[239–241] especially those (e.g., nucleic acids) having high oxidation/reduction potential.[242,243] The MPTS-modified GaNNWs have revealed promising candidature as an electrode for in situ detection of DNA hybridization phenomena, down to sub-pM concentration of target DNA (tDNA), via simply monitoring the electrochemical oxidation of adenine (A) and guanine (G), by using cyclic voltammetric (CV) techniques.[238] The control voltammograms of the pDNA (polyA-polyC)-immobilized GaNNWs reveal a broad peak around 0.837 V (vs. reference electrode [RE]), which has been attributed to the A-oxidation (Figure 49c, ssDNA). Upon hybridization with the tDNA (polyT-polyG), a well-defined oxidation peak appears with a little blue shift around 0.88 V (vs. RE), attributed to the G-oxidation (Figure 49c, dsDNA). The peak current $I_P$ exhibited an increasing trend with the increase in tDNA concentration (Figure 49d); however, around 10 nM it reached the saturation level, indicating the limitation of DNA-binding sites on the nanometric surface of GaNNWs. In Figure 50, the first segment exhibits the CV responses over the time scale for in situ DNA hybridization phenomena, revealing a complete hybridization within ~2 h. The second segment represents the reproducibility of sensor response via hybridization-dehybridization-rehybridization (HDR) cycles. This reveals that instead of $I_P$ (Figure 50a), the peak potential $V_P$ (Figure 50b) would be a suitable parameter for confirmation of DNA hybridization phenomena.

Though the CV technique can provide direct detection of DNA via electrochemical oxidation of DNA bases, it suffers from the irreversible redox activity of DNA bases, which leads to the consumption of analytes, as evident from the degradation of $I_P$ with time (Figure 50a). Simultaneously, large potential scan may cause the "etching" or "passivation" of the electrode surface. These effects can impede stability and performance of the DNA-modified electrode. On the other hand, electrochemical impedance spectroscopy (EIS) can provide an alternative safer platform for in situ biosensing, because it is sensitive to the changes in interfacial impedance of the electrodes (conductor or semiconductor) upon biorecognition events occurring at the surface-electrolyte interface. The study by Chen et al.[237] demonstrated in situ DNA sensing without the use of any redox marker, employing a constant potential at low positive value (0.3 V vs. RE) at the GaNNWs electrode in order to prevent the oxidation of the oligonucleotides. As evident from EIS results (Nyquist, Figure 51a, and Bode plots, Figure 51b), on immobilization of pDNA (pLF), there appeared an additional semicircular region at the lower frequency range or higher impedance value over the typical Faradaic spectrum of pristine GaNNWs. The additional impedimetric element (P2 in Figure 51b) could distinguish the GaNNWs electrode with the conventional metallic electrodes, which do not exhibit such Faradaic nature unless redox markers are used.

A hypothesis has been drawn by considering that the immobilization of negatively charged DNA molecules on NWs surface would create an additional capacitive element in series with GaNNWs, exhibiting their own individual electrical characteristics with an impedance comparable to GaN. Consequently, the electron would face two interfaces, GaN/DNA (GD) and DNA/electrolyte (DS) interfaces, in series, while transferring from electrolyte to electrode (Figures 51c, 51d). With the capture of target DNA (LF), as more negative charges accumulate on GaN surface, the electron transfer resistance $R_{DS}$ of the DS interface increased marginally (Figure 52a) with LF concentration ($C_{LF}$) due to electrostatic repulsion. However, the resistance $R_{GD}$ of the GD interface was found to be decreased rapidly with increase in $C_{LF}$ (Figure 52a), serving as a fingerprint for DNA modification on GaNNWs. Experimental observations led to the fact that DNA modification on GaNNWs surface resulted in the

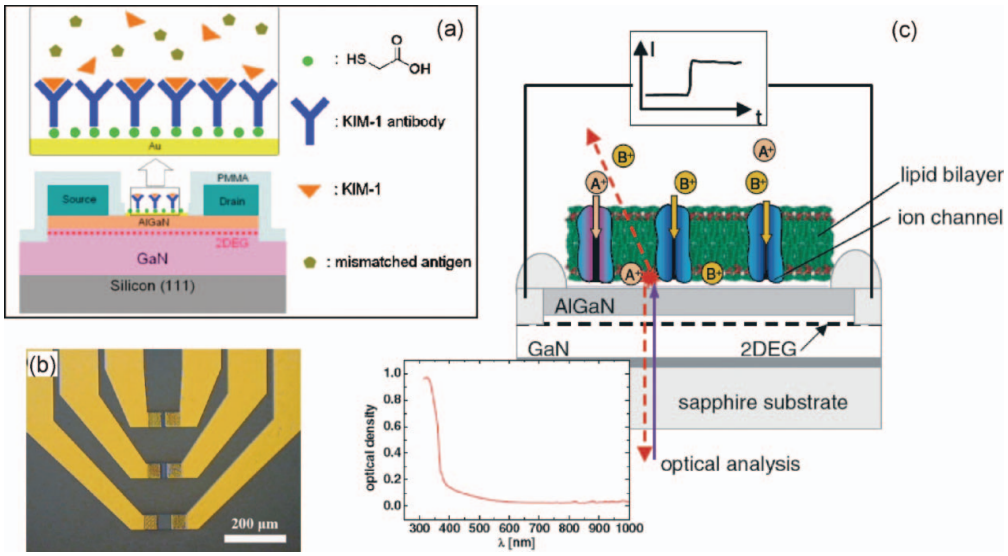


FIG. 47. (a) Schematic design of AlGaN/GaN heterostructure FET biosensor devices for kidney injury molecule-1 (KIM-1), an important biomarker for early detection of kidney injury. The gate area is Au-coated to functionalize with KIM-1 antibody on thioglycolic acid. (b) Planar-view photomicrograph of a complete device with a 5-nm Au film on the gate region. (Reprinted with permission from Wang et al.[232] Copyright 2007 American Institute of Physics.) (c) Schematic of a transparent AlGaN/GaN FET as the readout device for selective ion transport across a lipid bilayer membrane via transmembrane ion channels. Inset: the optical density of a 1-$\mu$m GaN layer on a sapphire substrate, representing the optical transparency of the device, enabling it to benefit from the possibility of simultaneous optical and electronic analysis of lipids. (Reprinted with permission from Steinhoff et al.[222] Copyright 2003 Wiley-VCH Verlag GmbH & CoKG.)

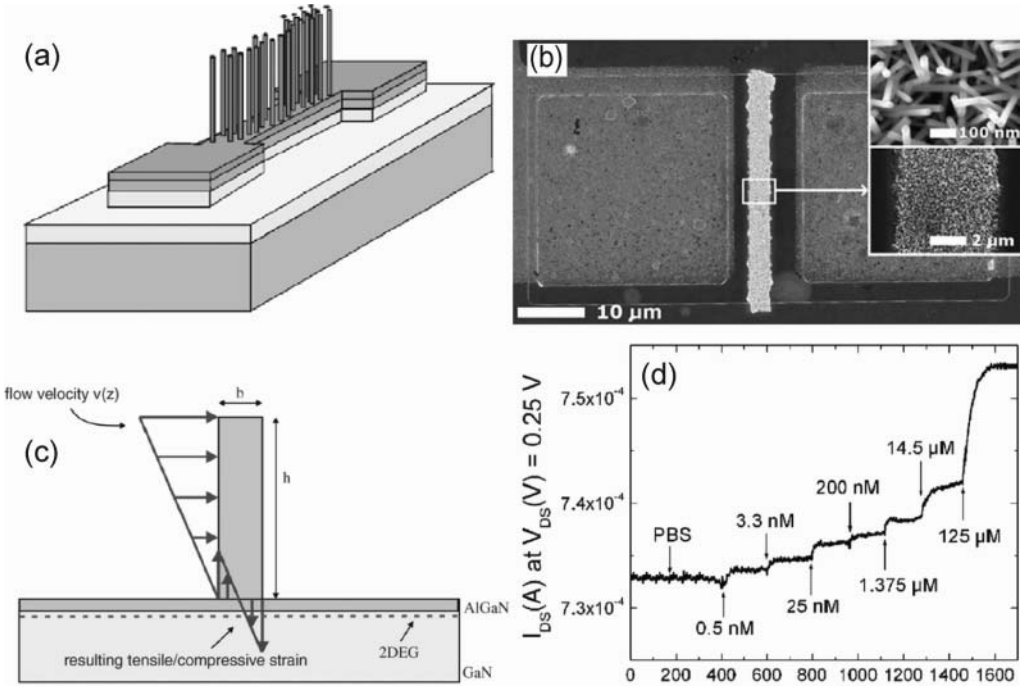


FIG. 48. (a) Schematic drawing of the AlGaN/GaN sensor structure with freestanding NWs on top. (b) Mechanical scheme used for the theoretical calculations: the principle of the sensor is such that the flow deflects the NW (diameter $d$ and height $h$) and thus creates a strain in the 2DEG, in turn leading to a change in its resistance. (Reprinted with permission from Tonisch et al.[233] Copyright 2007 Elsevier.) (c) SEM image of ZnONRs-gated AlGaN/GaN HEMT. Inset: HRTEM images of ZnONRs arrays grown on the gate area with different scales. (d) Plot of drain current versus time with successive exposure of glucose from 0.5 nM to 125 $\mu$M. (Reprinted with permission from Kang et al.[234] Copyright 2007 American Institute of Physics.)

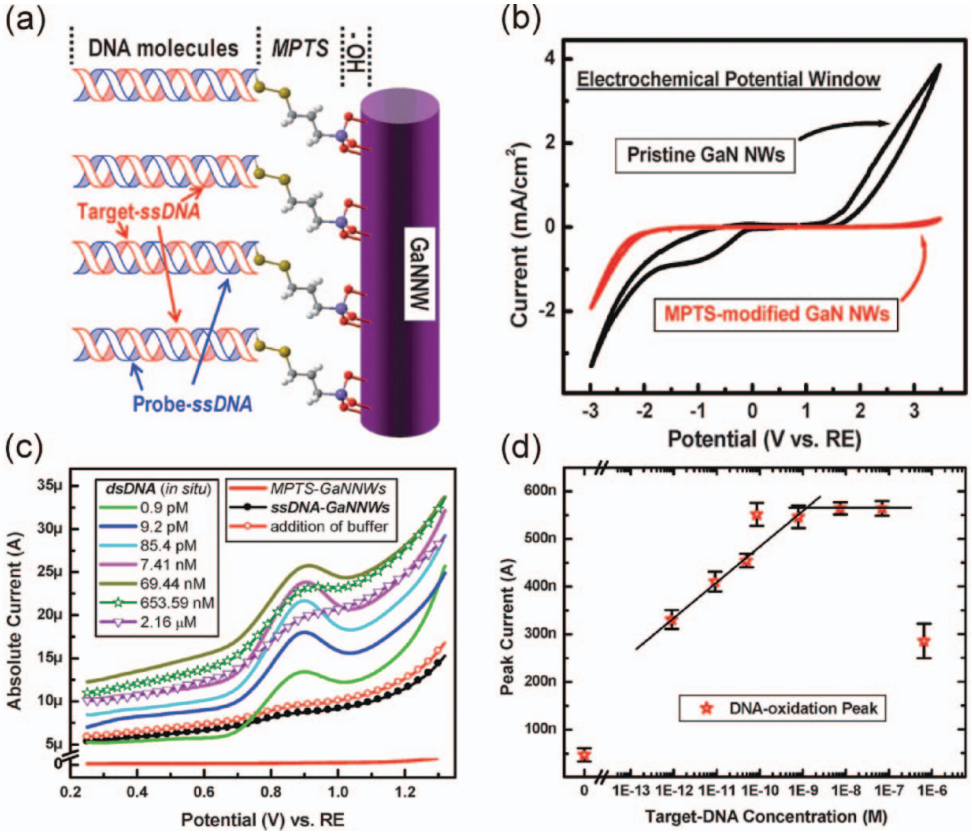


FIG. 49. (a) Schematic diagram of dsDNA-modified GaNNWs represents the surface modification stages: hydroxylation (-OH), MPTS modification (MPTS), DNA immobilization (Probe-ssDNA), and DNA hybridization (Target-ssDNA). (b) Typical cyclic voltammograms (CV) of the pristine and MPTS-modified GaNNWs electrodes, in PBS (pH = 7.42), at a scan rate of 100 mV/s. (c) In situ voltammetric detection of DNA hybridization (after background subtraction): typical CV of the MPTS-modified, probe-ssDNA-immobilized, and dsDNA-modified GaNNWs (at different target concentrations). (d) Variation of peak current of guanine oxidation with target ssDNA concentration. (Reprinted with permission from Ganguly et al.[238] Copyright 2009 The Royal Society of Chemistry.)

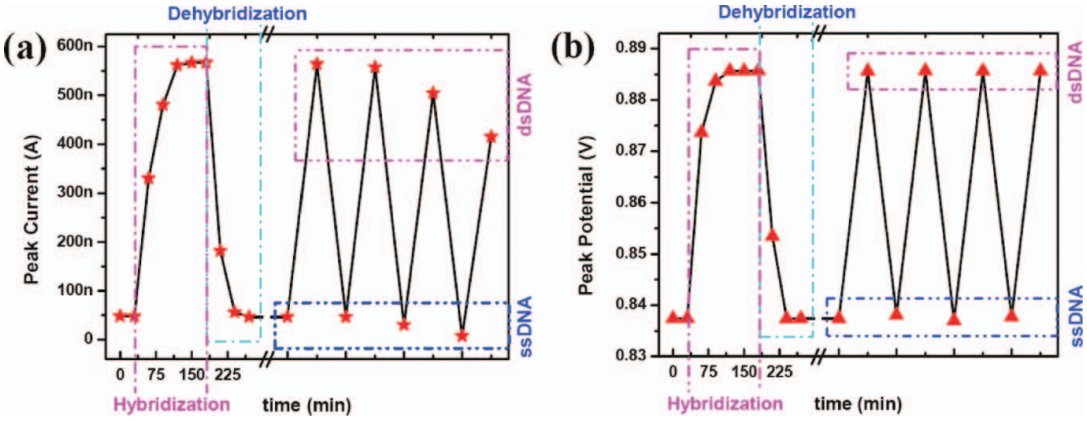


FIG. 50. Reproduction of response: cycles of hybridization-dehybridization-rehybridization (HDR) phenomena: variation of (a) peak current and (b) peak voltage over time scale. (Reprinted with permission from Ganguly et al.[238] Copyright 2009 The Royal Society of Chemistry.)

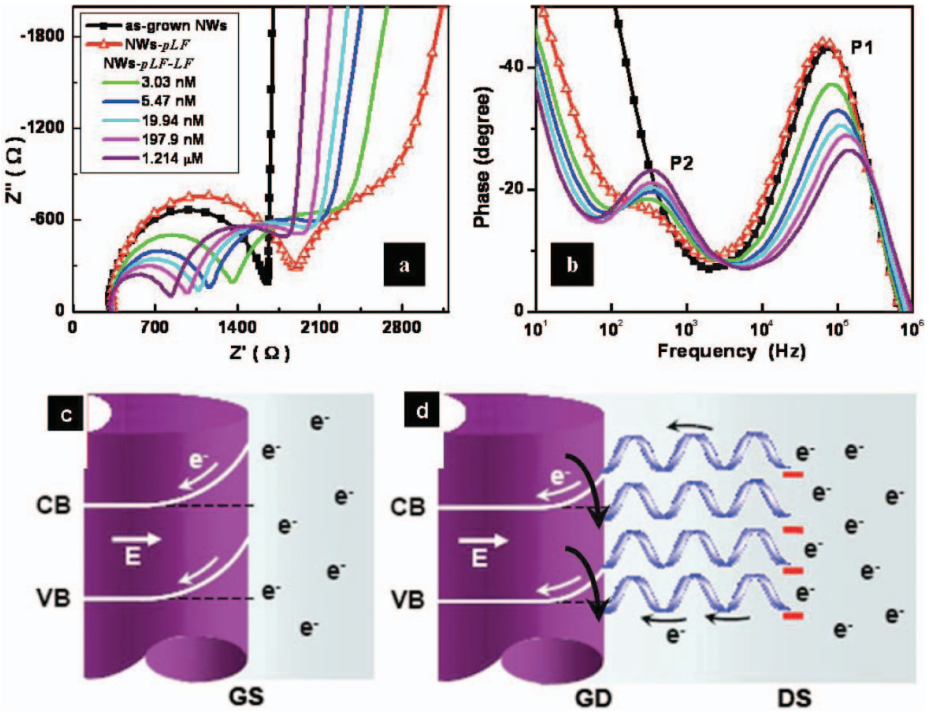


FIG. 51. EIS-based in situ DNA hybridization detection: (a) Nyquist plots and (b) corresponding Bode plots of as-grown, pLF-modified, and dsDNA-modified GaNNWs (at different LF concentrations). Proposed schematic illustration of lowering in surface band bending (SBB) and enhanced charge transport at GD interface: (c) maximum SBB for as-grown GaNNWs, (d) lowering of SBB with MPTS and pLF modification. CB and VB denote conduction and valence band, respectively; E represents the electric field direction. (Reprinted with permission from Chen et al.[237] Copyright 2009 American Chemical Society.)

flattenning of surface band bending of NWs (Figure 51d), a consequence of trap state passivation and charge redistribution, suppressing $R_{GD}$ (Figure 52a).

Employing the $R_{GD}$ as a sensing parameter, the study demonstrated the selectivity of the sensor employing two important hotspot mutations related to human p53 tumor-suppressor gene. The in situ selectivity experiment (Figure 52b) exhibited that only the fully complementary wild-type sequence (WT) among all targets could trigger a decrease in $R_{GD}$, even in pM concentration, and in presence of noncomplementary (LF) and single

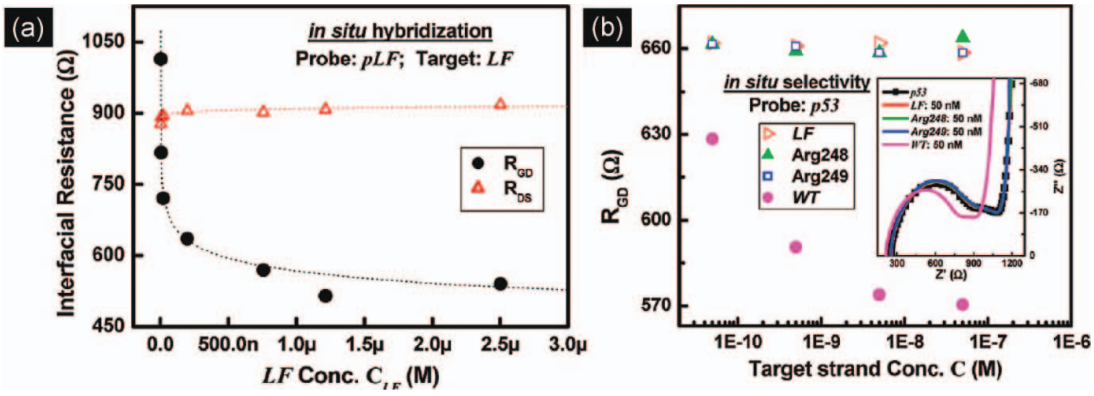


FIG. 52. (a) Variation of $R_{GD}$ and $R_{DS}$ with target concentration ($C_{LF}$). (b) EIS-based in situ DNA selectivity detection: variation of the same $R_{GD}$ with target concentration (C). Inset: Nyquist plots of p53-modified GaNNWs before and after the addition of target DNA strands, in the order as follows: LF, Arg248, Arg249, and WT. (Reprinted with permission from Chen et al.[237] Copyright 2009 American Chemical Society.)

mismatched molecules. In parallel, GaNNWs systems have also been employed for DNA detection via ex situ room temperature PL. The excitonic emission of pristine GaNNWs (~365 nm) was found to be quenched with subsequent pLF immobilization. The luminescence quenching was treated as a sensing parameter correlated to the DNA-induced surface modification, because the phenomenon has become more pronounced with increasing $C_{LF}$.

Reports on sensing using AlN nanostructures are rare, but there are few for AlN thin films. Due to its large electromechanical coupling coefficient, surface acoustic wave (SAW) propagation velocity (~5,607 m/s), resistance to humidity, and endurance to chemical etching, AlN-based SAW devices are promising for high-frequency, high-sensitivity applications,[244–248] over the conventional piezoelectric materials like quartz, lithium niobate, and lithium tantalate. AlN films are flexible in designing a piezoelectric device onto nonpiezoelectric substrates such as silicon. The opposite temperature coefficients of delay in Si and AlN make these materials particularly suitable to implement thermally stable SAW devices. Caliendo et al.[245] demonstrated a, AlN/Si SAW resonator (SAWR)-based chemical sensor application, operating at about 700 MHz. The microsensors, covered with a polymer film sensitive to relative humidity (RH) changes, were able to detect very low RH values (0.6–10%) with sensitivity and detection limit better by 38% and one order of magnitude, respectively, compared to the conventional SAW sensors. Chiu et al.[247,248] demonstrated a quantitative and ultrasensitive biodetection utilizing enhanced-AuNPs AlN-SAW sensor. The sensor is composed of self-assembled DNA-AuNPs conjugates onto functionalized AlN surfaces under physiological conditions. Because of higher operating frequencies of SAW sensors (typically >100 MHz) compared to 5–10 MHz for the conventional quartz crystal microbalance (QCM) sensors, the former's SAW mass sensitivity (~15 Hz cm$^2$/ng) was found to be about two orders of magnitude larger than the latter.

Other than thin-film configuration, the only report on biochemical sensing utilizing the surface sensitivity of 1D AlN nanostructures could be found via metal nanoparticles–assisted surface-enhanced Raman scattering (SERS) techniques.[249] Hexagonal AlNNRs and AlNNTs have been used to self-assemble metal (Ag, Au) particles on its surface (Figure 53). These metal NPs of <10 nm can enhance the electric field at the analyte position by the plasmon they generate under incident laser excitation. The Raman scattering cross section, which is a function of the electric field, is also enhanced and the Raman signatures could easily be seen even at high dilutions. Sputtered metal tends to self-assemble as NPs onto most nanomaterial, such as carbon nanotube and NWs, owing to the high surface area of the latter, but the choice of support, as such, is also important. If the support is Raman active, then the signal from the analyte may overlap with that of the support. Again, if the support is not inert, it may sometimes react with the analytes and degrade the Raman signatures we are looking for. Hence,

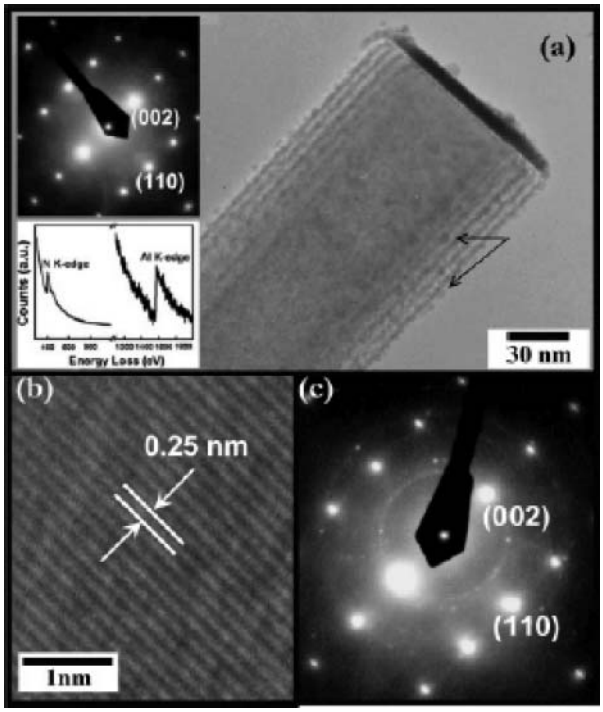


FIG. 53. TEM image of a single Ag-coated AlNNR (the arrows showing the nc-Ag); top and bottom insets show the SAED pattern and the electron energy loss spectroscopy (EELS) spectrum of the as-grown AlNNR, respectively. (b) HRTEM image of the as-grown AlNNR lattice. (c) SAED pattern of the Ag-coated AlNNR. (Reprinted with permission from Chattopadhyay et al.[249] Copyright 2005 American Chemical Society.)

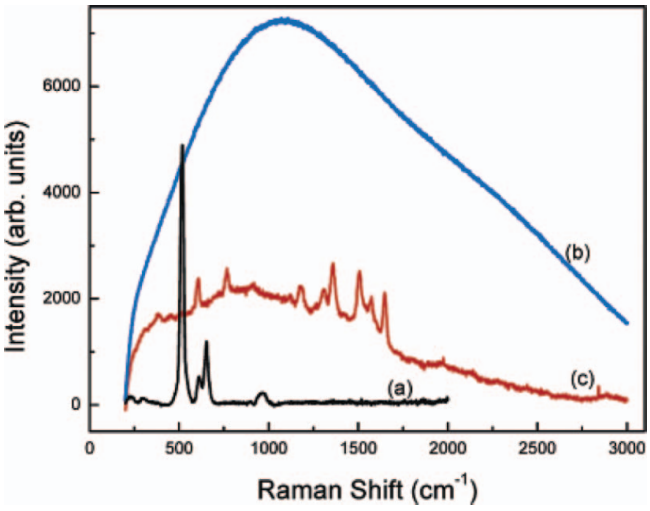


FIG. 54. Raman spectrum of (a) the as-grown AlNNRs and (b) the as-grown AlNNRs with R6G and (c) SERS spectrum of Ag-coated AlNNRs with R6G. (Reprinted with permission from Chattopadhyay et al.[249] Copyright 2005 American Chemical Society.)

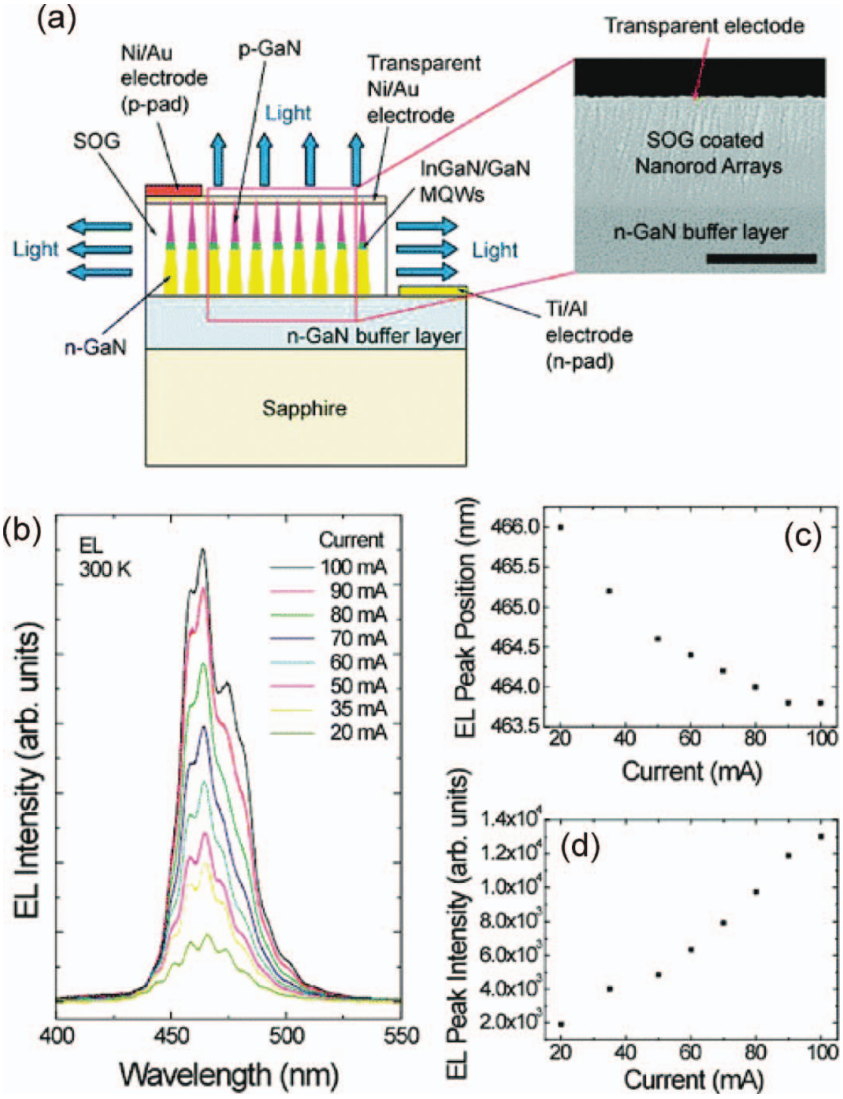


FIG. 55. (a) Schematic diagram and SEM image of cross-sectional MQW NR array LED. Scale bar 1 $\mu$m. (b)–(d) Room temperature electroluminescent (EL) characteristics of InGaN/GaN MQW NRA LEDs at various applied dc currents. EL peak position at 20 mA was 466 nm. A significant blue shift is observed with increasing current. EL peak intensity increased directly with injection current. (Reprinted with permission from Kim et al.[252] Copyright 2004 American Chemical Society.)

choice of a proper support is essential for molecular sensing using SERS. Molecules of rhodamine 6G have been detected by the SERS technique using AgNPs on AlNNRs (Figure 54). Other analytes such as bis pyridyl ethylene (BPE) have also been detected at high dilutions of $10^{-10}$ M.

### 11.2. Nanoscale Optoelectronic Devices

NWs form the building blocks for nanoscale electronics and optoelectronic devices.[250] The idea of nanoscale assembly of an emissive III–V or II–VI n-type NW with a nonemissive p-type silicon NW has been utilized to obtain ultraviolet to near-infrared emission.[251] Single or multicolor LEDs can be fabricated with predictable emissions depending solely on the bandgap of the emitting material. Again, a nanoscale transistor can be used to turn the nanoscale LED on and off.

Inorganic semiconductor nanocrystal-based multicolor LEDs using a GaN p-i-n architecture have also been demonstrated. In this case, an intrinsic semiconductor nanocrystal (CdSe) assembled (by Langmuir-Blodgett technique) on a p-type GaN layer can have an overcoat of an n-type GaN by the ENABLE technique.[35] The top n-type GaN becomes the electron injection layer in the electroluminescence (EL) device with injection efficiencies of $>1\%$. Depending on the nanocrystal emission, which is preserved by surface passivation, single or multicolor LEDs can be obtained. However, the multicolor emission bands may have a broad spectral overlap with

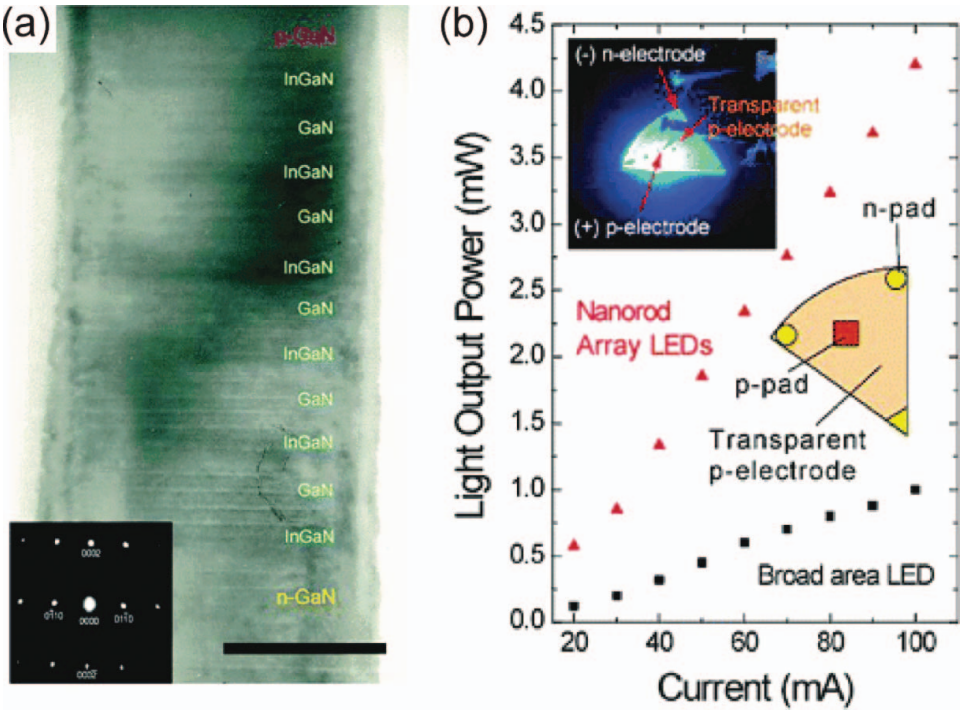


FIG. 56. (a) TEM image of an $In_{0.25}Ga_{0.75}N$/GaN MQWs in a nanorod. The length and diameter of the nanorod are around 1 $\mu$m and 70 nm, respectively. Scale bar is 30 nm. Inset shows the SAED pattern. (b) Light output power forward current characteristics of a six-period InGaN/GaN MQW NRA LED using an on-wafer testing configuration, compared to a conventional broad area LED. Insets show the top-view photograph image (above) and schematic diagram (below) of a blue emission from the $In_{0.25}Ga_{0.75}N$/GaN MQW NRA LED at 20 mA DC current. (Reprinted with permission from Kim et al.[252] Copyright 2004 American Chemical Society.)

each other depending on the nature and size of nanocrystals used.

Application of 1D materials to high-efficiency LEDs has been demonstrated.[252] The dislocation-free NRs are produced by a metal organic HVPE (MO-HVPE) on sapphire substrates. The structure of the device is shown in Figure 55a. An unintentionally doped n-GaN buffer (1.5 $\mu$m) layer was grown on the sapphire substrate; 0.5 $\mu$m of Si-doped n-GaNNRs and subsequently six periods of $In_{0.25}Ga_{0.75}N$/GaN MQW (4.8 nm/12 nm) NR array (Figure 56a) were grown on the n-GaN buffer layer. The NR array was completed with a 0.4-$\mu$m Mg-doped p-GaNNRs. The NR array was buried in spin-on-glass (SOG) to isolate individual NR. A Ti/Al (20/200 nm) n-type contact was defined on the n-GaN buffer layer, a thin Ni/Au (20/40 nm) layer was deposited on the SOG for contact with each of the NR, and finally a Ni/Au (20/200 nm) layer was formed for the p-contact. The InGaN/GaN MQW structures show strong room temperature EL with different current levels (Figures 55b–55d). The light output power of the InGaN/GaN MQW NR array was superior to the conventional broad area LEDs of the same area (Figure 56b). In the MQW NR arrays the carrier transport is physically confined along the length of the nanostructures. This ensures efficient use of the injected carriers. The higher light output in the MQW NR arrays compared to the broad area LEDs prove an efficient light extraction from the sidewalls of the NR array. A similar report of InGaN/GaN MQW grown on sapphire with n- and p-GaN capping layers showed enhanced luminescence when shaped into a nanotip morphology using a specialized plasma etching technique.[253] This method involves a strain relaxation in the MQWs and resultant tenfold increase in the light emission. The use of nanostructures in high-brightness LEDs has been proved to be more efficient compared to thin film.

The core-multishell NW heterostructure described in Section 6 (Figure 18) has been used in multicolor, high-efficiency nanoscale LEDs.[80] Electrical properties were measured on an FET structure after contacts were made on the p-type outer shell and n-type core to simultaneously inject holes and electrons into the NW heterostructure (inset, Figure 57a). The current-voltage characteristics showed a typical p-n diode rectification property (Figure 57a). This NW device shows strong EL response in the forward bias. EL images taken from the NW device show high brightness emission that red shifted (Figure 57b) as the In composition was increased from 1 to 40%. Normalized EL spectra (Figure 57c) collected from near the p-contact of five NW devices, differing only in the In content of the $In_xGa_{1-x}N$ shell, show distinct emissions at 367, 412, 459, 510, and 577 nm

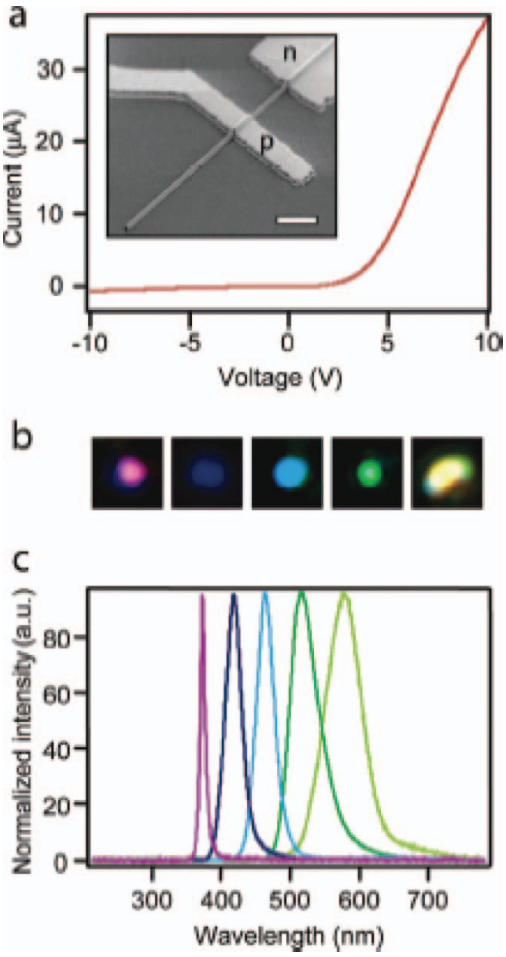


FIG. 57. (a) Current-voltage data recorded on a core/multishell (CMS) nanowire device. Inset shows the FESEM image of a CMS nanowire device. Scale bar is 2 $\mu$m. (b) Optical microscopy images collected from around p-contact of CMS nanowire LEDs in forward bias showing purple, blue, greenish blue, green, and yellow emissions, respectively. (c) Normalized electroluminescent spectra recorded from the representative forward-biased multicolor CMS nanowire LEDs. (Reprinted with permission from Qian et al.[80] Copyright 2005 American Chemical Society.)

corresponding to x = 1, 10, 20, 25, and 35, respectively. The emission line widths also increased with In content, which is believed due to increased strain and inhomogeneity in the material. The absence of the broad emission around 550 nm or GaN band edge at 365 nm proves injected carrier recombination only in the active InGaN layer. The estimated external quantum efficiency (QE) of the NW device was 5.8% at 440 nm and 3.9% at 540 nm. These QE values are comparable to the InGaN-based, single-quantum-well thin-film LED devices at similar wavelengths.[254,255]

Most of the NWs-based studies have focused on single-NW-based devices. However, the integration of individual NW into the thin film–based microchip is a critical process for large-scale industrial manufacturers. Kang et al.[148] have already demonstrated that, instead of a single NW, a bundle of as-synthesized NWs could be utilized, without requiring any manipulation, in order to achieve more realistic and efficient platform for photodetectors or sensors application. Chen et al.[256] have utilized a new bridging NW concept[257] to directly integrate an ensemble of NWs on-chip. These NWs are laterally grown across a trench and suspended between two film posts as nanobridges. After the first demonstration of GaN nanobridges growth by Kim et al.,[258] Henry et al.[259] further extended its application in nanoelectromechanical resonator arrays. Chen et al. have demonstrated a viable nanobridge device with ultrahigh photocurrent generation efficiency.[256] They reported an effective approach for on-chip fabrication of aligned and contact-barrier-free GaN nanobridge devices (Figures 58a, 58b). The top-view Field Emission SEM (FESEM) images (Figure 58b) showed lateral epitaxial growth of high-density NWs across the trench and form bridges between the electrode posts. The total number of integrated nanobridges in a single device could be adjusted by controlling the post-width and the nanobridge growth density in a CVD process.

A typical PC spectrum (Figure 59a) of the nanobridge device showed an observable increase in photocurrent above a threshold excitation energy around 3.2 eV, the bandgap energy of GaN, with remarkably high efficiency compared to the traditional thin-film photodetectors.[164,260–263] The responsivity ($R$) values, defined as the photocurrent generated per unit incident power,[264] exhibited a nearly two orders of magnitude increase beyond 3.2 eV (Figure 59b), revealing the potential of the GaN nanobridge device as a visible-blind UV photodetector. Because the effective sensing area increases with the number of bridging NWs, a higher nanobridge number could amplify the current signal of the device, as evident from a near linear proportionality of photocurrent values to the bridge numbers (Figure 59c). The R values from the three samples with different nanobridge number exhibited nearly the same magnitude having the same slope with applied bias (Figure 59d). However, the maximum $R > 10^6$ A/W, is nearly three to six orders of magnitude higher than those reported for GaN thin-film detectors.[160,163,164,260–263,265,266]

In a recent report on GaN-based UV photodetector application, Wu et al.[267] introduced a new strategy to synthesize the nitride nanofibers (NFs) by employing the electrospinning technique claiming low-cost, high-efficiency growth of extremely long GaN nanofibers (GaNNFs) on a large scale. Controlled assembly as well as precise doping with transition metal has been realized using this solution-based, catalyst, or template-independent method. The synthesized GaNNFs with a diameter of ~40 nm and a length exceeding a centimeter, are polycrystalline in nature. In order to precisely pattern the GaNNFs in a designated device (inset of Figure 60a), a specially designed electrode, fabricated by putting two strips of conductive silicon in a side-by-side parallel arrangement, was used to collect NFs. During the electrospinning process, the strips were

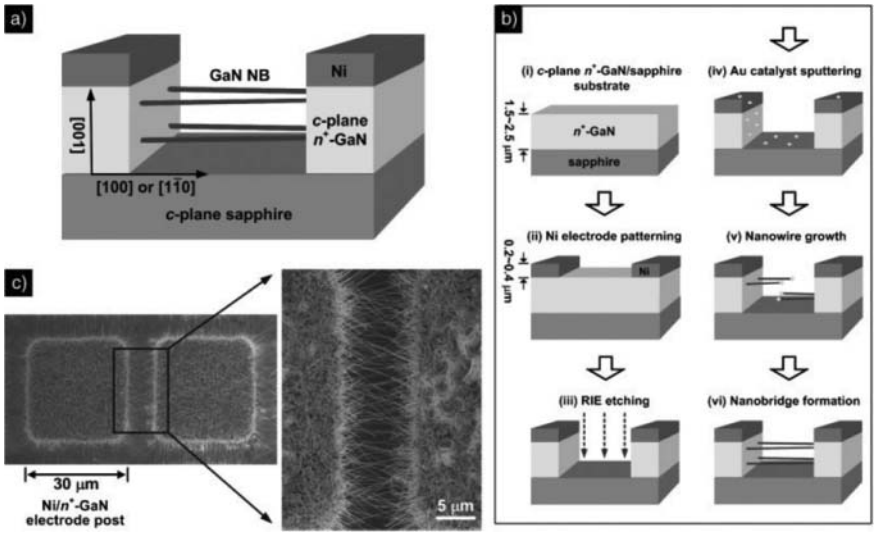


FIG. 58. (a) Schematic architecture of the GaN nanobridge device. The arrows indicate the *c*-plane $n^+$-GaN electrode posts with [100] and [110] sidewalls. (b) Fabrication process of the device. (c) Top-view FESEM images focused on one pair of Ni/n+−GaN electrode posts (left) and on the trench with NWs bridging between two posts (right). (Reprinted with permission from Chen et al.[256] Copyright 2008 Wiley-VCH Verlag GmbH & CoKG.)

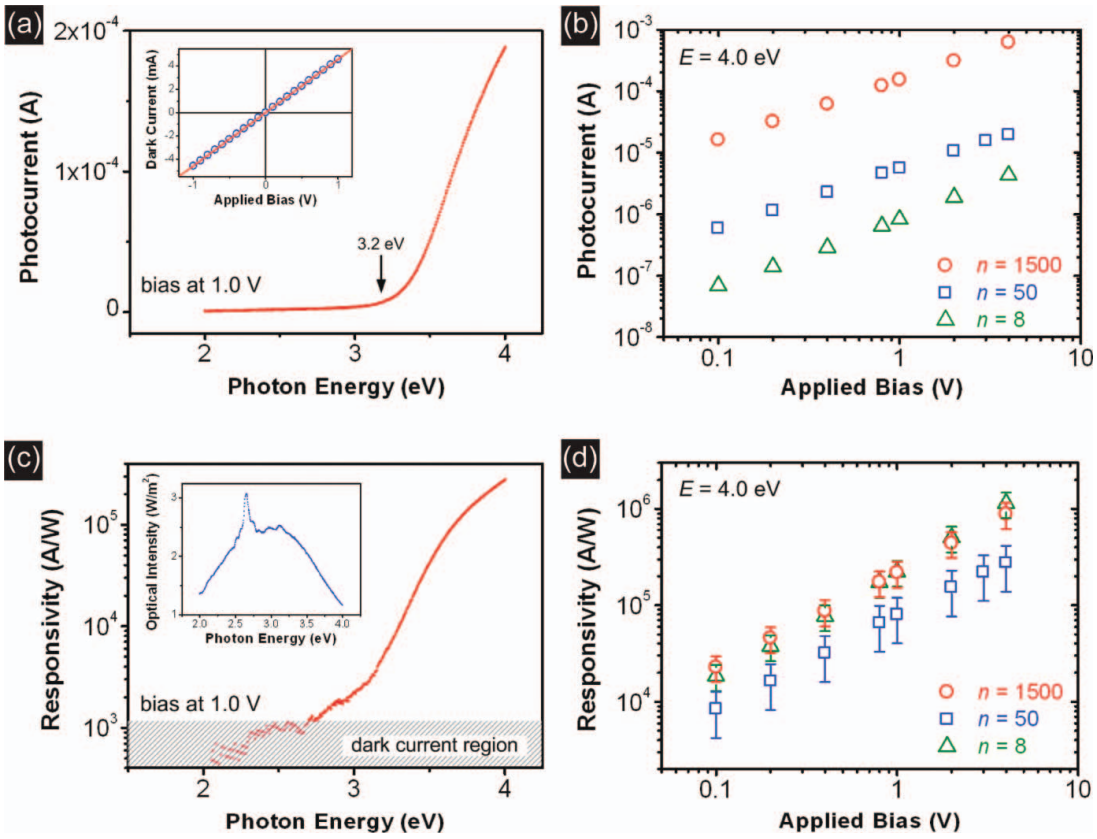


FIG. 59. (a) Typical photocurrent spectrum and (b) the corresponding responsivity spectrum of a GaN nanobridge device with nanobridge number ($n$) 1,500 at a bias of 1.0 V. Inset in (a): dark current to bias measurement; inset in (b): light source intensity spectrum used for PC characterization. (c) Photocurrent and (d) responsivity versus applied bias for three devices with different $n$ under excitation at 4.0 eV. (Reprinted with permission from Chen et al.[256] Copyright 2008 Wiley-VCH Verlag GmbH & CoKG.)

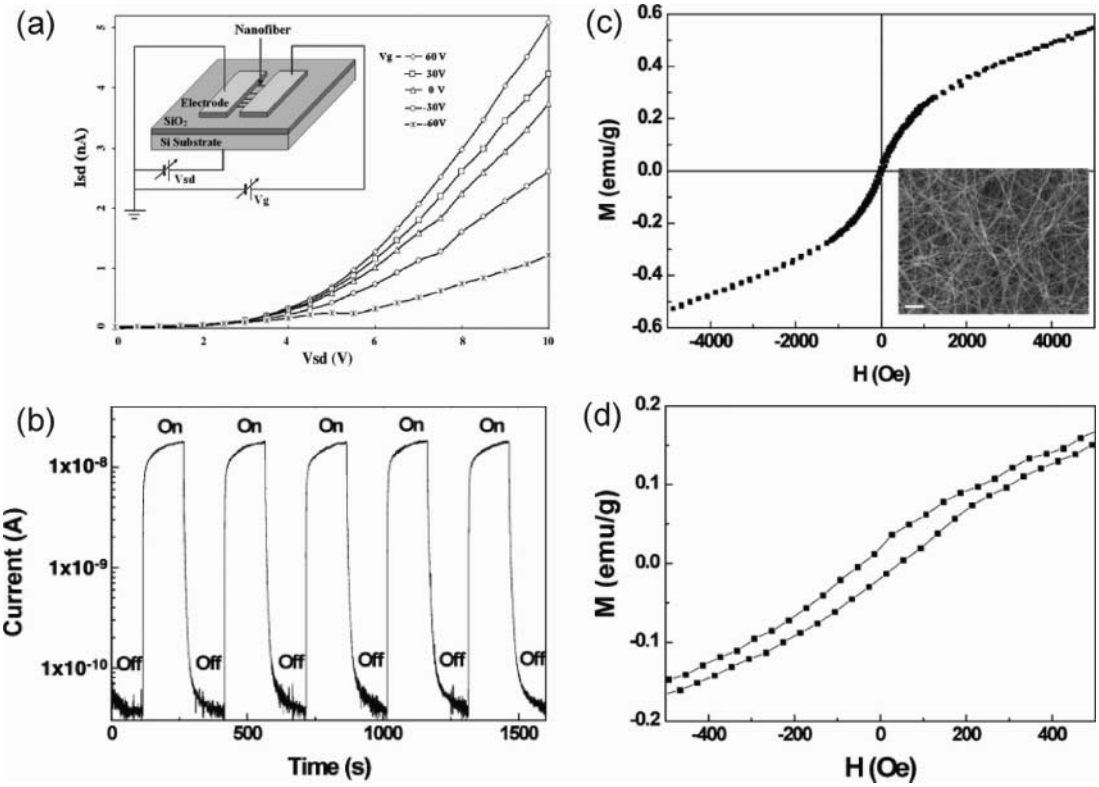


FIG. 60. (a) Gate-dependent I–V measurement of a GaN nanofiber (GaNNFs) FET device at room temperature. Inset: schematic view of the GaNNF FET configuration. (b) Conductance response of a GaNNF FET device under pulsed illumination from a 254-nm UV light with power density 3 mW/cm$^2$. (c) Magnetization loops of the Mn-doped GaNNFs measured at room temperature. Inset: a typical SEM image of the samples (scale bar: 1 mm). (d) Magnetization in low-field region. (Reprinted with permission from Wu et al.[267] Copyright 2009 Wiley-VCH Verlag GmbH & CoKG.)

grounded, providing a driving electrostatic force to align the positively charged NFs between the two counterelectrodes. Typical current-voltage ($I_{sd} - V_{sd}$) characteristics (Figure 60a) revealed an intrinsic n-type semiconductive nature of GaNNFs. These polycrystalline GaNNFs showed a promising candidature for high-performance UV photodetector, exhibiting superior performance in sensitivity, response speed, and reversibility, as depicted by Figure 60b. The conductance of a single GaNNF FET device increases by 800 times under UV excitation;[267] in contrast, a single-crystal CVD-grown GaNNW exhibited a smaller response (∼78) to UV light.[147]

Ultra-thin Mn-doped GaNNFs have been synthesized with designed doping concentrations by adding a suitable amount of $Mn(NO_3)_2$ into the precursor solution and a subsequent electrospinning and annealing process. The Mn-doped GaNNFs ($Ga_{0.9}Mn_{0.1}N$ NFs) showed ferromagnetic characteristics

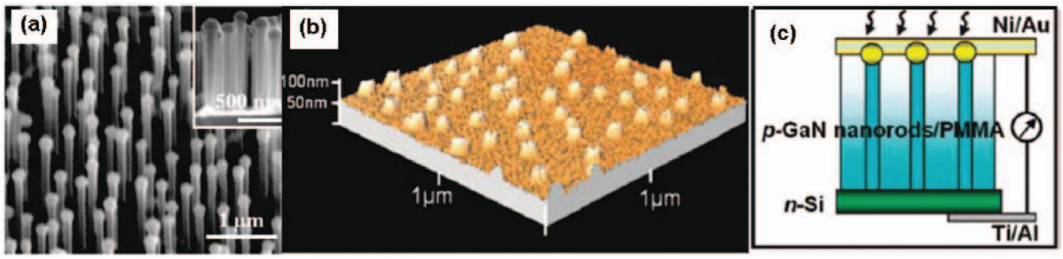


FIG. 61. (a) Tilt top-view SEM image of Mg-doped GaNNRs arrays. Inset shows cross-sectional SEM image. (b) AFM image of GaNNRs tips exposed above the photoresist layer. (c) A schematic of the p-GaNNRs/n-Si heterojunction photovoltaic cell. (Reprinted with permission from Tang et al.[271] Copyright 2008 American Chemical Society.)

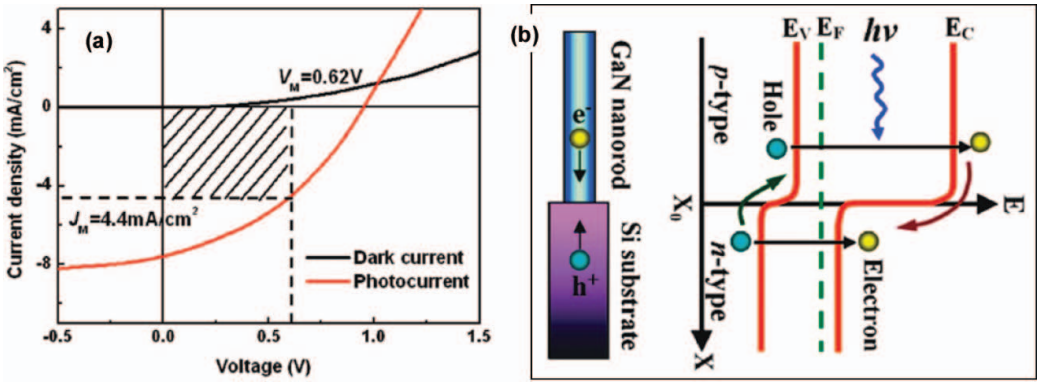


FIG. 62. (a) Current density vs. voltage for the p-GaNNRs/n-Si solar cell in the dark and under simulated AM1.5G illumination with an intensity of 100 mW/cm$^2$. (b) Schematic energy band diagram of the heterojunction diode showing the photogenerated carrier transfer process. (Reprinted with permission from Tang et al.[271] Copyright 2008 American Chemical Society.)



at room temperature (Figure 60c), with clear indication of magnetic hysteresis and remanence in low-field region (Figure 60d), exhibiting a new way to the facile synthesis of 1D diluted magnetic semiconductor (DMS) nanostructures, which reveal significant importance for constructing spintronic nanodevices such as ultrasensitive magnetic field sensors and spin FETs.

For photovoltaic (PV) application, aligned 1D nanostructure arrays possess the advantage of providing direct conduction paths for photogenerated carriers from the junction to the external electrode, thereby resulting in high carrier collection efficiency, compared to polycrystalline films.[268–270] A study by Tang et al.[271] revealed the potential of a uniform array of vertically aligned wide-bandgap Mg-doped GaNNRs epitaxially grown on a low-bandgap n-type Si substrate for fabricating a p-n heterojunction PV cell. The GaNNRs array on the top of the heterostructure act as the optical window for suppressing the minority carrier recombination and enhance short-wavelength spectral response, as well as an effective antireflection layer to reduce visible optical loss due to its low reflectance originating from its high surface area and nanoscale subwavelength size.[271] The direct growth of aligned Mg-doped GaNNR arrays on n-Si substrates by the CVD method reveals their uniform size distribution around 100 nm and preferential growth along the [0001] direction (Figure 61a). To fabricate the heterojunction solar cell, the spaces between the GaNNRs were filled with an insulating photoresist (PMMA) via spin coating. The sample surface was partially dissolved by acetone until the tips of GaNNRs were exposed for metal contact (AFM image, Figure 61b), followed by conventional ohmic contacts Ni/Au (30/50 nm) and Ti/Al (30/50 nm) electrodes onto the p-type GaNNRs and the backside of n-type Si substrate, respectively (Figure 61c).

The current density-voltage characteristics (Figure 62a) exhibited well-defined rectifying behavior in the dark with a large rectification ratio. Under illumination from a calibrated solar simulator with an intensity of 100 mW/cm$^2$ (equivalent to one sun), a maximum power conversion efficiency (PCE) of ~2.73% was achieved with a high open-circuit voltage ($V_{OC}$) of ~0.95 V, a short-circuit current density ($J_{SC}$) of ~7.6 mA/cm$^2$, and a fill factor (FF) of ~0.38. The PCE increased with increasing light intensity and is >2.0% under all tested illumination intensities. Figure 62b shows the schematic energy band diagram of the p-GaNNR/n-Si heterojunction diode at thermal equilibrium, illustrating the possible explanation for the rectifying behavior of the cell. A lLarge bandgap difference between Si and GaN ($E_g$ = 1.1 and 3.4 eV, respectively) would lead to an asymmetrical energy barrier for electrons formed at the junction, reducing the electron diffusion and electron-hole recombination in GaNNRs. Because the hole injection into the n-Si side is naturally low due to the built-in field, GaNNRs array on the top of the heterojunction was used as a wide bandgap semiconductor to decrease the leakage current in the depletion region. Under illumination from the top, photons with energy less than $E_g$(GaN) but greater than $E_g$(Si) would transmit through NRs, acting as an optical window, and be absorbed by Si; light with photon energies larger than $E_g$(GaN) will be absorbed by GaNNRs. The holes and electrons generated in both sides of the heterojunction are collected effectively due to the large built-in electric field at the junction and thus yield the photocurrent.

## 12. CONCLUDING REMARKS

Growth and characterization of the group III-nitride semiconducting materials have been discussed with an effort to distinguish the bulk from the nanomaterials. The size and shape selection in the nanomaterials and their correlation with the growth kinetics are sketched to give a basic idea to the readers. Optical properties, luminescence in particular, and structural properties, Raman scattering in particular, have been discussed to understand the effect of the nano size on them. The ternary materials within this class of compounds have also been discussed with a stress on their growth and properties. Electrical properties, under dark and illuminated conditions, of those

nanostructured materials have been discussed in detail. Conduction mechanisms in size-controlled regimes have been explained vis-à-vis thin films in many cases. Lastly, the cutting-edge applications in biomolecular sensing and nanoscale light-emitting diode applications of these materials is brought forward in an attempt to complement the popular device and applications that are reviewed and reported.

## ACKNOWLEDGMENTS

This work was done under the financial assistance from the National Science Council, Ministry of Education (MOE), and Academia Sinica, Taiwan.

## REFERENCES

1. W.C. Johnson, J.B. Parsons, and M.C. Crew, Nitrogen compounds of gallium III gallic nitride, *J. Phys. Chem.*, **36**, 2651 (1932).
2. R. Juza and H. Hahn, Über die kristallstrukturen von $Cu_3N$, GaN und InN, *Zeitschr. Anorgan. Allgem. Chem.*, **239**, 282 (1938).
3. H.G. Grimmeiss and H. Koelmans, Über die kantenemission und andere emission des GaN, *Zeitschrift Naturforschung Teil A*, **14**, 264 (1959).
4. H.P. Maruska and J.J. Tietjen, The preparation and properties of vapor-deposited single-crystalline GaN, *Appl. Phys. Lett.*, **15**, 327 (1969).
5. J.I. Pankove, E.A. Miller, and J.E. Berkeyheiser, GaN blue light-emitting diodes, *J. Lumin.*, **5**, 84 (1972).
6. H. Morkoc and S.N. Mohammad, High-luminosity blue and blue-green gallium nitride light-emitting diodes, *Science*, **267**, 51 (1995).
7. S. Nakamura, T. Mukai, and M. Senoh, Candela-class high-brightness InGaN/AlGaN double-heterostructure blue-light-emitting diodes, *Appl. Phys. Lett.*, **64**, 1687 (1994).
8. S. Nakamura, The roles of structural imperfections in InGaN-based blue light-emitting diodes and laser diodes, *Science*, **281**, 956 (1998).
9. A. Loiseau, F. Willaime, N. Demoncy, G. Hug, and H. Pascard, Boron nitride nanotubes with reduced numbers of layers synthesized by arc discharge, *Phys. Rev. Lett.*, **76**, 4737 (1996).
10. M. Terauchi, M. Tanaka, K. Suzuki, A. Ogino, and K. Kimura, Production of zigzag-type BN nanotubes and BN cones by thermal annealing, *Chem. Phys. Lett.*, **324**, 359 (2000).
11. L. Bourgeois, Y. Bando, W.Q. Han, and T. Sato, Structure of boron nitride nanoscale cones: Ordered stacking of 240° and 300° disclinations, *Phys. Rev. B*, **61**, 7686 (2000).
12. A. Ganguly, L.C. Chen, K.H. Chen, and S. Chattopadhyay, Recent trends in indium nitride nanomaterials, in *III-Nitride devices and nano-engineering*, Z.C. Feng, Ed., Imperial College Press, UK, 431 (2008).
13. S.J. Pearton, B.S. Kang, B.P. Gila, D.P. Norton, O. Kryliouk, F. Ren, Y.W. Heo, C.Y. Chang, G.C. Chi, W.M. Wang, and L.C. Chen, GaN, ZnO and InN nanowires and devices, *J. Nanosci. Nanotechnol.*, **8**, 99 (2008).
14. S. Nakamura, Blue-Green light-emitting diodes and violet laser diodes, *Mater. Res. Soc. Bull.*, **22**, 29 (1997).
15. I. Akasaki and H. Amano, Lasers, in *GaN* (Gallium nitride), vol. 1, J.I. Pankove, and T.D. Moustakas, Eds., Academic, New York, 459 (1998).
16. S. Nakamura, III-V nitride based LEDs, in *GaN and Related Materials*, S.J. Pearton, Ed., Gordon and Breach, New York, 471 (1997).
17. H. Morkoc, *Nitride Semiconductors and Devices*, Springer-Verlag, Berlin (1999).
18. W. Han, S. Fan, Q. Li, and Y. Hu, Synthesis of gallium nitride nanorods through a carbon nanotube-confined reaction, *Science*, **277**, 1287 (1997).
19. Y. Zhang, J. Liu, R. He, Q. Zhang, X. Zhang, and J. Zhu, Synthesis of aluminum nitride nanowires from carbon nanotubes, *Chem. Mater.*, **13**, 3899 (2001).
20. J. Liu, X. Zhang, Y. Zhang, R. He, and J. Zhu, Synthesis of aluminum nitride nanowires from carbon nanotubes, *J. Mater. Res.*, **16**, 3133 (2001).
21. P.G. Caceres and H.K. Schmid, Morphology and crystallography of aluminum nitride whiskers, *J. Am. Ceram. Soc.*, **77**, 977 (1994).
22. J. Zhang, X.S. Peng, X.F. Wang, Y.W. Wang, and L.D. Zhang, Micro-Raman investigation of GaN nanowires prepared by direct reaction Ga with $NH_3$, *Chem. Phys. Lett.*, **345**, 372 (2001).
23. G. Selvaduray and L. Sheet, Aluminum nitride—review of synthesis methods, *Mater. Sci. Technol.*, **9**, 463 (1993).
24. R.S. Wagner and W.C. Ellis, Vapor-liquid-solid mechanism of single crystal growth, *Appl. Phys. Lett.*, **4**, 89 (1964).
25. C.H. Liang, L.C. Chen, J.S. Hwang, K.H. Chen, Y.T. Hung, and Y.F. Chen, Selective-area growth of indium nitride nanowires on gold-patterned Si(100) substrates, *Appl. Phys. Lett.*, **81**, 22 (2002).
26. C.C. Chen, C.C. Yeh, C.H. Chen, M.Y. Yu, H.S. Liu, J.J. Wu, K.H. Chen, L.C. Chen, J.Y. Peng, and Y.F. Chen, Catalytic growth and characterization of gallium nitride nanowires, *J. Am. Chem. Soc.*, **123**, 2791 (2001).
27. T.J. Trentler, K.M. Hickman, S.C. Goel, A.M. Viano, P.C. Gibbons, and W.E. Buhro, Solution-liquid-solid growth of crystalline III-V semiconductors—an analogy to vapor-liquid-solid growth, *Science*, **270**, 1791 (1995).
28. W.E. Buhro, K.M. Hickman, and T.J. Trentler, Turning down the heat on semiconductor growth: Solution-chemical syntheses and the solution-liquid-solid mechanism, *Adv. Mater.*, **8**, 685 (1996).
29. S.D. Dingman, N.P. Rath, P.D. Markowitz, P.C. Gibbons, and W.E. Buhro, Low-temperature, catalyzed growth of indium nitride fibers from azido-indium precursors, *Angew. Chem. Int. Ed.*, **39**, 1470 (2000).
30. C. Kawai and A. Yamakawa, Crystal growth of silicon nitride whiskers through a VLS mechanism using $SiO_2$-$Al_2O_3$-$Y_2O_3$ oxides as liquid phase, *Ceram. Int.*, **24**, 135 (1998).
31. S.C. Shi, C.F. Chen, S. Chattopadhyay, Z.H. Lan, K.H. Chen, and L.C. Chen, Growth of single-crystalline wurtzite aluminum nitride nanotips with a self-selective apex angle, *Adv. Funct. Mater.*, **15**, 781 (2005).
32. S.C. Shi, S. Chattopadhyay, C.F. Chen, K.H. Chen, and L.C. Chen, Structural evolution of AlN nano-structures: Nanotips and nanorods, *Chem. Phys. Lett.*, **418**, 152 (2006).
33. M. He, I. Minus, P. Zhou, S.N. Mohammad, J.B. Halpern, R. Jacobs, W.L. Sarney, L. Salamanca-Riba, and R.D. Vispute, Growth of large-scale GaN nanowires and tubes by direct reaction of Ga with $NH_3$, *Appl. Phys. Lett.*, **77**, 3731 (2000).
34. M. He, P. Zhou, S.N. Mohammad, G.L. Harris, J.B. Halpern, R. Jacobs, W.L. Sarney, and L. Salamanca-Riba, Growth of GaN

nanowires by direct reaction of Ga with $NH_3$, *J. Cryst. Growth*, **231**, 357 (2001).
35. A.H. Mueller, M.A. Petruska, M. Achermann D.J. Werder, E.A. Akhadov, D.D. Koleske, M.A. Hoffbauer, and V.I. Klimov, Multicolor light-emitting diodes based on semiconductor nanocrystals encapsulated in GaN charge injection layers, *Nano Lett.*, **5**, 1039 (2005).
36. W. Shi, Y. Zheng, N. Wang, C.S. Lee, and S.T. Lee, A general synthetic route to III-V compound semiconductor nanowires, *Adv. Mater.*, **13**, 591 (2001).
37. J. Zhang, L. Zhang, X. Peng, and X. Wang, Vapor-solid growth route to single-crystalline indium nitride nanowires, *J. Mater. Chem.*, **12**, 802 (2002).
38. J.A. Haber, P.C. Gibbons, and W.E. Buhro, Morphological control of nanocrystalline aluminum nitride: Aluminum chloride-assisted nanowhisker growth, *J. Am. Chem. Soc.*, **119**, 5455 (1997).
39. J.A. Haber, P.C. Gibbons, and W.E. Buhro, Morphologically selective synthesis of nanocrystalline aluminum nitride, *Chem. Mater.*, **10**, 4062 (1998).
40. K.J. Lee, D.H. Ahn, and Y.S. Kim, Aluminum nitride whisker formation during combustion synthesis, *J. Am. Ceram. Soc.*, **83**, 1117 (2000).
41. H. Chen, Y. Cao, and X. Xiang, Formation of AlN nano-fibers, *J. Cryst.Growth*, **224**, 187 (2001).
42. J.Y. Li, X.L. Chen, Z.Y. Qiao, Y.G. Cao, and Y.C. Lan, Formation of GaN nanorods by a sublimation method, *J. Cryst. Growth*, **212**, 408 (2000).
43. C.C. Yu, C.F. Chu, J.Y. Tsai, H.W. Huang, T.H. Hsueh, C.F. Lin, and S.C. Wang, Gallium nitride nanorods fabricated by inductively coupled plasma reactive ion etching, *Jpn. J. Appl. Phys.*, **41**, L910 (2002).
44. C.K. Kuo, C.W. Hsu, C.T. Wu, Z.H. Lan, C.Y. Mou, K. H. Chen, C.C. Chen, and L.C. Chen, Self-regulating and diameter-selective growth of GaN nanowires, *Nanotechnology*, **17**, S332 (2006).
45. A. Chatterjee, S. Chattopadhyay, C.W. Hsu, C.H. Shen, L.C. Chen, C.C. Chen, K.H. Chen, and H.Y. Lee, Growth and characterization of gallium nitride nanowires produced on different sol-gel derived catalyst dispersed in titania and polyvinyl alcohol matrix, *J. Mater. Res.*, **19**, 1768 (2004).
46. C.C. Tang, S.S. Fan, H.Y. Dang, P. Li, and Y.M. Liu, Simple and high-yield method for synthesizing single-crystal GaN nanowires, *Appl. Phys. Lett.*, **77**, 1961 (2000).
47. W.Q. Han and A. Zettl, Pyrolysis approach to the synthesis of gallium nitride nanorods, *Appl. Phys. Lett.*, **80**, 303 (2002).
48. K.W. Chang and J.J. Wu, Low-temperature catalytic synthesis gallium nitride nanowires, *J. Phys. Chem. B*, **106**, 7796 (2002).
49. Y. Ding, P.X. Gao, and Z.L.Wang, Catalyst-nanostructure interfacial lattice mismatch in determining the shape of VLS grown nanowires and nanobelts: A case of Sn/ZnO, *J. Am. Chem. Soc.*, **126**, 2066 (2004).
50. M.S. Hu, W.M. Wang, T.T. Chen, L.S. Hong, C.W. Chen, C.C. Chen, Y.F. Chen, K.H. Chen, and L.C. Chen, Sharp infrared emission from single-crystalline indium nitride nanobelts prepared using guided-stream thermal chemical vapor deposition, *Adv. Funct. Mater.*, **16**, 537 (2006).
51. Z.H. Lan, W.M. Wang, C.L. Sun, S.C. Shi, C.W. Hsu, T.T. Chen, K.H. Chen, C.C. Chen, Y.F. Chen, and L.C. Chen, Growth mechanism, structure and IR photoluminescence studies of indium nitride nanorods, *J. Cryst. Growth*, **269**, 87 (2004).
52. Z.L. Wang, Z.W. Pan, and Z.R. Dai, Structures of oxide nanobelts and nanowires, *Microsc. Microanal. Microstruct.*, **8**, 467 (2002).
53. S.C. Shi, C.F. Chen, G.M. Hsu, J.S. Hwang, S. Chattopadhyay, Z.H. Lan, K.H. Chen, and L.C. Chen, Reduced temperature-quenching of photoluminescence from indium nitride nanotips grown by metalorganic chemical vapor deposition, *Appl. Phys. Lett.*, **87**, 203103 (2005).
54. S. Chattopadhyay, K.H. Chen, S.C. Shi, C.T.Wu, C.H. Chen, and L.C. Chen, Self-selected apex angle distribution in aluminum nitride and indium nitride nanotips, *Appl. Phys. Lett.*, **89**, 143105 (2006).
55. G. Ehrlich and F.G. Hudda, Atomic view of surface self-diffusion—tungsten on tungsten, *J. Chem. Phys.*, **44**, 1039 (1966).
56. R.L. Schwoebel and E.J. Shipsey, Step Motion On Crystal Surfaces, *J. Appl. Phys.*, **37**, 3682 (1966).
57. L.C. Chen, K.H. Chen, and C.C. Chen, Group III- and Group IV-Nitride Nanorods and Nanowires, in *Nanowires and Nanobelts: Materials, Properties and Devices: Metal and Semiconductor Nanowires*, vol. 1, Z.L. Wang, Ed., Kluwer Academic Publishers, Boston, 257 (2003).
58. T. Kuykendall, P.J. Pauzauskie, Y. Zhang, J. Goldberger, D. Sirbuly, J. Denlinger, and P. Yang, Crystallographic alignment of high-density gallium nitride nanowire arrays, *Nature Mater.*, **3**, 524 (2004).
59. J.Y. Lao, J.Y. Huang, D.Z. Wang, and Z.F. Ren, Hierarchical oxide nanostructures, *J. Mater. Chem.*, **14**, 770 (2004).
60. Z.H. Lan, C.H. Liang, C.W. Hsu, C.T. Wu, H.M. Lin, S. Dhara, K.H. Chen, L.C. Chen, and C.C. Chen, Nanohomojunction (GaN) and nanoheterojunction (InN) nanorods on one-dimensional GaN nanowire substrates, *Adv. Funct. Mater.*, **14**, 233 (2004).
61. H.M. Lin, Y.L. Chen, J. Yang, Y.C. Liu, K.M. Yin, J.J. Kai, F.R. Chen, L.C. Chen, Y.F. Chen, and C.C. Chen, Synthesis and characterization of core-shell GaP@GaN and GaN@GaP nanowires, *Nano Lett.*, **3**, 537 (2003).
62. M.T. Björk, B.J. Ohlsson, T. Sass, A.I. Persson, C. Thelander, M.H. Magnusson, K. Deppert, L.R. Wallenberg, and L. Samuelson, One-dimensional steeplechase for electrons realized, *Nano Lett.*, **2**, 87 (2002).
63. J. Ristić, E. Calleja, M.A. Sánchez García, J.M. Ulloa, J. Sánchez Páramo, J.M. Calleja, U. Jahn, A. Trampert, and K.H. Ploog, Characterization of GaN quantum discs embedded in $Al_xGa_{1-x}N$ nanocolumns grown by molecular beam epitaxy, *Phys. Rev. B*, **68**, 125305 (2003).
64. J. Ristić, E. Calleja, A. Trampert, S. Fernández-Garrido, C. Rivera, U. Jahn, and K.H. Ploog, Columnar AlGaN/GaN nanocavities with AlN/GaN Bragg reflectors grown by molecular beam epitaxy on Si(111), *Phys. Rev. Lett.*, **94**, 146102 (2005).
65. D. Brunner, H. Angerer, E. Bustarret, F. Freudenber, R. Höpler, R. Dimitrov, O. Ambacher, and M. Stutzman, Optical constants of epitaxial AlGaN films and their temperature dependence, *J. Appl. Phys.*, **82**, 5090 (1997).
66. I.P. Smorchkova, C.R. Elsass, J.P. Ibbetson, R. Vetury, B. Heying, P. Fini, E. Haus, S.P. Den Baars, J.S. Speck, and U.K. Mishra, Polarization-induced charge and electron mobility in AlGaN/GaN heterostructures grown by plasma-assisted molecular-beam epitaxy, *J. Appl. Phys.*, **86**, 4520 (1999).
67. J. Su, M. Gherasimova, G. Cui, H. Tsukamoto, J. Han, T. Onuma, M. Kurimoto, S.F. Chichibu, C. Broadbridge, Y. He, and A.V. Nurmikko, Growth of AlGaN nanowires by metalorganic

chemical vapor deposition, *Appl. Phys. Lett.*, **87**, 183108 (2005).
68. P.D. Markowitz, M.P. Zach, P.C. Gibbons, R.M. Penner, and W.E. Buhro, Phase separation in $Al_xGa_{1-x}As$ nanowhiskers grown by the solution-liquid-solid mechanism, *J. Am. Chem. Soc.*, **123**, 4502 (2001).
69. K. Tateno, H. Gotoh, and Y. Watanabe, GaAs/AlGaAs nanowires capped with AlGaAs layers on GaAs(311)B substrates, *Appl. Phys. Lett.*, **85**, 1808 (2004).
70. H. Choi, J.C. Johnson, R. He, S. Lee, F. Kim, P. Pauzauskie, J. Goldberger, R.J. Saykally, and P. Yang, Self-organized GaN quantum wire UV lasers, *J. Phys. Chem.*, **107**, 8721 (2003).
71. I. Ho and G.B. Stringfellow, Solid phase immiscibility in GaInN, *Appl. Phys. Lett.*, **69**, 2701 (1996).
72. N. Yoshimoto, T. Matsuoka, T. Sasaki, and A. Katsui, Photoluminescence of InGaN films grown at high-temperature by metalorganic vapor-phase epitaxy, *Appl. Phys. Lett.*, **59**, 2251 (1991).
73. S. Nakamura and T. Mukai, High-quality InGaN films grown on GaN films, *Jpn. J. Appl. Phys.*, **31**, L1457 (1992).
74. S. Nakamura, T. Mukai, M. Senoh, S. Nagahama, and N. Iwasa, $In_xGa_{(1-x)}N/In_yGa_{(1-y)}N$ superlattices grown on GaN films, *J. Appl. Phys.*, **74**, 3911 (1993).
75. H.M. Kim, W.C. Lee, T.W. Kang, K.S. Chung, C.S. Yoon, and C.K. Kim, InGaN nanorods grown on (111) silicon substrate by hydride vapor phase epitaxy, *Chem. Phys. Lett.*, **380**, 181 (2003).
76. H.M. Kim, T.W. Kang, and K.S. Chung, Growth of indium gallium nitride nanorod arrays by HVPE using indium metal, *J. Ceram. Proc. Res.*, **5**, 241 (2004).
77. H.M. Kim, H. Lee, S.I. Kim, S.R. Ryu, T.W. Kang, and K.S. Chung, Formation of InGaN nanorods with indium mole fractions by hydride vapor phase epitaxy, *Phys. Status Solidi B*, **241**, 2802 (2004).
78. X.M. Cai, Y.H. Leung, K.Y. Cheung, K.H. Tam, A.B. Djurišić, M.H. Xie, H.Y. Chen, and S. Gwo, Straight and helical InGaN core-shell nanowires with a high In core content, *Nanotechnology*, **17**, 2330 (2006).
79. L.W. Ji, T.H. Fang, S.C. Hung, Y.K. Su, S.J. Chang, and R.W. Chuang, Ultra small self-organized nitride nanotips, *J. Vac. Sci. Technol. B*, **23**, 2496 (2005).
80. F. Qian, S. Gradečak, Y. Li, C.Y. Wen, and C.M. Lieber, Core/multishell nanowire heterostructures as multicolor, high-efficiency light-emitting diodes, *Nano Lett.*, **5**, 2287 (2005).
81. C.W. Hsu, A. Ganguly, C.H. Liang, Y.T. Hung, C.T. Wu, G.M. Hsu, Y.F. Chen, C.C. Chen, K.H. Chen, and L.C. Chen, Enhanced emission of (In, Ga) nitride nanowires embedded with self-assembled quantum dots, *Adv. Funct. Mater.*, **18**, 938 (2008).
82. X. Duan and C.M. Lieber, Laser-assisted catalytic growth of single crystal GaN nanowires, *J. Am. Chem. Soc.*, **122**, 188 (2000).
83. C.C. Chen and C.C. Yeh, Large-scale catalytic synthesis of crystalline gallium nitride nanowires, *Adv. Mater.*, **12**, 738 (2000).
84. H.W. Seo, S.Y. Bae, J. Park, H. Yang, K.S. Park, and S. Kim, Strained gallium nitride nanowires, *J. Chem. Phys.*, **116**, 9492 (2002).
85. S. Dhara, A. Datta, C.T. Wu, Z.H. Lan, K.H. Chen, Y.L. Wang, L.C. Chen, C.W. Hsu, H.M. Lin, and C.C. Chen, Enhanced dynamic annealing in $Ga^+$ ion-implanted GaN nanowires, *Appl. Phys. Lett.*, **82**, 451 (2003).
86. S. Dhara, A. Datta, C.T. Wu, Z.H. Lan, K.H. Chen, Y.L. Wang, C.W. Hsu, C.H. Shen, L.C. Chen, and C.C. Chen, Hexagonal-to-cubic phase transformation in GaN nanowires by $Ga^+$ implantation, *Appl. Phys. Lett.*, **84**, 5473 (2004).
87. S. Dhara, A. Datta, C.T. Wu, K.H. Chen, Y.L. Wang, S. Muto, T. Tanabe, C.H. Shen, C.W. Hsu, L.C. Chen, and T. Maruyama, Mechanism of nanoblister formation in $Ga^+$ self-ion implanted GaN nanowires, *Appl. Phys. Lett.*, **86**, 203119 (2005).
88. A. Datta, S. Dhara, S. Muto, C.W. Hsu, C.T. Wu, C.H. Shen, T. Tanabe, T. Maruyama, K.H. Chen, L.C. Chen, and Y.L. Wang, Formation and *in situ* dynamics of metallic nanoblisters in $Ga^+$ implanted GaN nanowires, *Nanotechnology*, **16**, 2764 (2005).
89. C.W. Pao, P.D. Babu, H.M. Tsai, J.W. Chiou, S.C. Ray, S.C. Yang, F.Z. Chien, W.F. Pong, M.H. Tsai, C.W. Hsu, L.C. Chen, C.C. Chen, K.H. Chen, H.J. Lin, J.F. Lee, and J.H. Guo, Electronic structures of group-III-nitride nanorods studied by x-ray absorption, x-ray emission, and Raman spectroscopy, *Appl. Phys. Lett.*, **88**, 223113 (2006).
90. H.L. Liu, C.C. Chen, C.T. Chia, C.C. Yeh, C.H. Chen, M.Y. Yu, S. Keller, and S.P. DenBaars, Infrared and Raman-scattering studies in single-crystalline GaN nanowires, *Chem. Phys. Lett.*, **345**, 245 (2001).
91. S. Dhara, S. Chandra, G. Mangamma, S. Kalavathi, P. Shankar, K.G.M. Nair, A.K. Tyagi, C.W. Hsu, C.C. Kuo, L.C. Chen, K.H. Chen, and K.K. Sriram, Multiphonon Raman scattering in GaN nanowires, *Appl. Phys. Lett.*, **90**, 213104 (2007).
92. S. Sahoo, M.S. Hu, C.W. Hsu, C.T. Wu, K.H. Chen, L.C. Chen, A.K. Arora, and S. Dhara, Surface optical Raman modes in InN nanostructures, *Appl. Phys. Lett.*, **93**, 233116 (2008).
93. G.D. Gilliland, Photoluminescence spectroscopy of crystalline semiconductors, *Mater. Sci. Eng.*, **18**, 99 (1997).
94. B.G. Yacobi and D.B. Holt, *Cathodoluminescence Microscopy of Inorganic Solids*, Plenum Press, New York and London (1990).
95. P.Y. Yu and M. Cardona, *Fundamentals of Semiconductors*, Springer, Berlin, 307 (1996).
96. W. Shan, X.C. Xie, J.J. Song, and B. Goldenberg, Time-resolved exciton luminescence in GaN grown by metalorganic chemical vapor deposition, *Appl. Phys. Lett.*, **67**, 2512 (1995).
97. Y. Xie, Y. Qian, W. Wang, S. Zhang, and Y. Zhang, A benzene-thermal synthetic route to nanocrystalline GaN, *Science*, **272**, 1926 (1996).
98. C.Y. Yeh, S.B. Zhang, and A. Zunger, Confinement, surface, and chemisorption effects on the optical-properties of Si quantum wires, *Phys. Rev. B*, **50**, 14405 (1994).
99. X. Chen, J. Li, Y. Cao, Y. Lan, H. Li, M. He, C. Wang, Z. Zhang, and Z. Qiao, Straight and smooth GaN nanowires, *Adv. Mater.*, **12**, 1432 (2000).
100. H.M. Kim, D.S. Kim, Y.S. Park, D.Y. Kim, T.W. Kang, and K.S. Chung, Growth of GaN nanorods by a hydride vapor phase epitaxy method, *Adv. Mater.*, **14**, 991 (2002).
101. C.W. Chen, K.H. Chen, C.H. Shen, J.J. Wu, J.W. Chiou, W.F. Pong, A. Ganguly, and L.C. Chen, Anomalous blueshift in emission spectra of ZnO nanorods with sizes beyond quantum confinement regime, *Appl. Phys. Lett.*, **88**, 241905 (2006).
102. H.M. Kim, D.S. Kim, D.Y. Kim, T.W. Kang, Y.H. Cho, and K.S. Chung, Growth and characterization of single-crystal GaN nanorods by hydride vapor phase epitaxy, *Appl. Phys. Lett.*, **81**, 2193 (2002).
103. S. Dhara, A. Datta, C.T. Wu, Z.H. Lan, K.H. Chen, Y.L. Wang, Y.F. Chen, C.W. Hsu, L.C. Chen, H.M. Lin, and C.C. Chen,

Blueshift of yellow luminescence band in self-ion-implanted n-GaN nanowire, *Appl. Phys. Lett.*, **84**, 3486 (2004).
104. V.Y. Davydov, A.A. Klochikhin, R.P. Seisyan, V.V. Emtsev, S.V. Ivanov, F. Bechstedt, J. Furthmüller, H. Harima, A.V. Mudryi, J. Aderhold, O. Semchinova, and J. Graul, Absorption and emission of hexagonal InN. Evidence of narrow fundamental band gap, *Phys. Status Solidi B*, **229**, R1 (2002).
105. B.R. Nag, On the band gap of indium nitride, *Phys. Status Solidi B*, **237**, R1 (2003).
106. J. Wu, W. Walukiewicz, W. Shan, K.M. Yu, J.W. Ager III, E.E. Haller, H. Lu, and W.J. Schaff, Effects of the narrow band gap on the properties of InN, *Phys. Rev. B,* **66**, 201403 (2002).
107. T.V. Shubina, S.V. Ivanov, V.N. Jmerik, M.M. Glazov, A.P. Kalvarskii, M.G. Tkachman, A.Vasson, J. Leymarie, A. Kavokin, H. Amano, I. Akasaki, K.S.A. Butcher, Q. Guo, B. Monemar, and P.S. Kop′ev, Optical properties of InN with stoichoimetry violation and indium clustering, *Phys. Status Solidi A*, **202**, 377 (2005).
108. C.H. Shen, H.Y. Chen, H.W. Lin, S. Gwo, A.A. Klochikhin, and V.Y. Davydov, Near-infrared photoluminescence from vertical InN nanorod arrays grown on silicon: Effects of surface electron accumulation layer, *Appl. Phys. Lett.*, **88**, 253104 (2006).
109. P.C. Wei, S. Chattopadhyay, F.S. Lin, C.M. Hsu, S. Jou, J.T. Chen, P.J. Huang, H.C. Hsu, H.C. Shih, K.H. Chen, and L.C. Chen, Origin of the anomalous temperature evolution of photoluminescence peak energy in degenerate InN nanocolumns, *Optic. Express*, **17**, 11690 (2009).
110. S.P. Fu, C.J. Yu, T.T. Chen, G.M. Hsu, M.J. Chen, L.C. Chen, K.H. Chen, and Y.F. Chen, Anomalous optical properties of InN nanobelts: Evidence of surface band bending and photoelastic effects, *Adv. Mater.*, **19**, 4524 (2007).
111. M.S. Hu, G.M. Hsu, K.H. Chen, C.J. Yu, H.C. Hsu, L.C. Chen, J.S. Hwang, L.S. Hong, Y.F. Chen, Infrared lasing in InN nanobelts, *Appl. Phys. Lett.*, **90**, 123109 (2007).
112. S.C. Shi, C.F. Chen, S. Chattopadhyay, K.H. Chen, B.W. Ke, L.C. Chen, L. Trinkler, and B. Berzina, Luminescence properties of wurtzite AlN nanotips, *Appl. Phys. Lett.*, **89**, 163127 (2006).
113. R.A. Youngman, J.H. Harris, and D.A. Chernoff, Cathodoluminescence and Photoluminescence in Aluminum Nitride, in *Ceramic Transactions*, vol. 5, W.S. Young, G.L. McVay, and G.E. Pike, Eds., American Ceramic Society, Westerville, OH 399 (1989).
114. M. Strassburg, J. Senawiratne, N. Dietz, U. Haboeck, A. Hoffmann, V. Noveski, R. Dalmau, R. Schlesser, and Z. Sitar, The growth and optical properties of large, high-quality AlN single crystals, *J. Appl. Phys.*, **96**, 5870 (2004).
115. Y. Sun, Y.H. Cho, H.M. Kim, and T.W. Kang, High efficiency and brightness of blue light emission from dislocation-free InGaN/GaN quantum well nanorod arrays, *Appl. Phys. Lett.*, **87**, 093115 (2005).
116. Y.H. Cho, G.H. Gainer, A.J. Fischer, J.J. Song, S. Keller, U.K. Mishra, and S.P. DenBaars, "S-shaped" temperature-dependent emission shift and carrier dynamics in InGaN/GaN multiple quantum wells, *Appl. Phys. Lett.*, **73**, 1370 (1998).
117. P. Perlin, T. Suski, H. Teisseyre, M. Leszczynski, I. Grzegory, J. Jun, S. Porowski, P. Boguslowski, J. Bernholc, J.C. Chervin, A. Polian, and T.D. Moustakas, Towards the identification of the dominant donor in GaN, *Phys. Rev. Lett.*, **75**, 296 (1995).
118. S. Nakamura, T. Mukai, and M. Senoh, *In-situ* monitoring and Hall measurements of GaN grown with GaN buffer layers, *J. Appl. Phys.*, **71**, 5543 (1992).
119. O. Brandt, H. Yang, H. Kostial, and K.H. Ploog, High p-type conductivity in cubic GaN/GaAs(113)*A* by using Be as the acceptor and O as the codopant, *Appl. Phys. Lett.*, **69**, 2707 (1996).
120. J. Neugebauer and C.G. Van de Walle, Phase stability and electronic structures of $GaAs_{1-x}N_x$ alloys, *Mater. Res. Soc. Symp. Proc.*, **339**, 687 (1994).
121. G. Popovici, H. Morkoc, and S.N. Mohammad, Deposition and properties of III-nitrides by molecular beam epitaxy, in *Group III Nitride Semiconductor Compounds*, B. Gil, Ed., Clarendon, Oxford, 19 (1998).
122. J.J. Song and W. Shan, Optical properties and lasing in GaN, in *Group III Nitride Semiconductor Compounds*, B. Gil, Ed., Clarendon, Oxford, 182 (1998).
123. S. Nakamura, GaN growth using GaN buffer layer, *Jpn. J. Appl. Phys.*, **30**, L1705 (1991).
124. S. Nakamura, T. Mukai, and M. Senoh, Si-doped and Ge-doped GaN films grown with GaN buffer layers, *Jpn. J. Appl. Phys.*, **31**, 2883 (1992).
125. S.C. Jain, M. Willander, J. Narayan, and R. Van Overstraeten, III-nitrides: Growth, characterization, and properties, *J. Appl. Phys.*, **87**, 965 (2000).
126. Y. Irokawa, O. Fujishima, T. Kachi, Y. Nakano, Electrical activation characteristics of silicon-implanted GaN, *J. Appl. Phys.*, **97**, 083505 (2005).
127. W. Gotz, N.M. Johnson, C. Chen, H. Liu, C. Kuo, and W. Imler, Activation energies of Si donors in GaN, *Appl. Phys. Lett.*, **68**, 3144 (1996).
128. H. Amano, M. Kito, K. Hiramatsu, and I. Akasaki, P-type conduction in Mg-doped GaN treated with low-energy electron-beam irradiation (LEEBI), *Jpn. J. Appl. Phys.*, **28**, L2112 (1989).
129. S. Nakamura, M. Senoh, and T. Mukai, Highly p-typed Mg-doped GaN films grown with GaN buffer layers, *Jpn. J. Appl. Phys.*, **30**, L1708 (1991).
130. I. Akasaki, H. Amano, M. Kito, and K. Hiramatsu, Photoluminescence of Mg-doped p-type GaN and electroluminescence of GaN p-n-junction LED, *J. Lumin.*, **48–49**, 666 (1991).
131. W. Gotz, N.M. Johnson, J. Walker, D.P. Bour, and R.A. Street, Activation of acceptors in Mg-doped GaN grown by metalorganic chemical vapor deposition, *Appl. Phys. Lett.*, **68**, 667 (1996).
132. Y. Huang, X. Duan, Y. Cui, and C.M. Lieber, Gallium nitride nanowire nanodevices, *Nano Lett.*, **2**, 101 (2002).
133. Z. Zhong, F. Qian, D. Wang, and C.M. Lieber, Synthesis of p-type gallium nitride nanowires for electronic and photonic nanodevices, *Nano Lett.*, **3**, 343 (2003).
134. C.Y. Chang, G.C. Chi, W.M. Wang, L.C. Chen, K.H. Chen, F. Ren, and S.J. Pearton, Electrical transport properties of single GaN and InN nanowires, *J. Electron. Mater.*, **35**, 738 (2006).
135. T. Kuykendall, P. Pauzauskie, S. Lee, Y. Zhang, J. Goldberger, and P. Yang, Metalorganic chemical vapor deposition route to GaN nanowires with triangular cross sections, *Nano Lett.*, **3**, 1063 (2003).
136. E. Stern, G. Cheng, E. Cimpoiasu, R. Klie, S. Guthrie, J. Klemic, I. Kretzschmar, E. Steinlauf, D.T. Evans, E. Broomfield, J. Hyland, R. Koudelka, T. Boone, M. Young, A. Sanders, R. Munden, T.

Lee, D. Routenberg, and M.A. Reed, Electrical characterization of single GaN nanowires, *Nanotechnology*, **16**, 2941 (2005).
137. M. Razeghi and A. Rogalski, Semiconductor ultraviolet detectors, *J. Appl. Phys.*, **79**, 7433 (1996).
138. C.R. Abernathy, Growth of Group-III Nitrides from Molecular Beams, in *GaN and Related Materials*, Pearton, S. J., Ed., Gordon and Breach, New York, 11 (1997).
139. C.Y. Chang, G.C. Chi, W.M. Wang, L.C. Chen, K.H. Chen, F. Ren, and S.J. Pearton, Transport properties of InN nanowires, *Appl. Phys. Lett.*, **87**, 093112 (2005).
140. S. Yin, Z.Z. Sun, J. Lu, and X.R. Wang, Explanation to the resistance anomaly observed in nanowires, *Appl. Phys. Lett.*, **88**, 233110 (2006).
141. S.C. Shi, C.F. Chen, S. Chattopadhyay, K.H. Chen, and L.C. Chen, Field emission from quasi-aligned aluminum nitride nanotips, *Appl. Phys. Lett.*, **87**, 073109 (2005).
142. C.S. Chang, S. Chattopadhyay, L.C. Chen, K.H. Chen, C.W. Chen, Y.F. Chen, R. Collazo, and Z. Sitar, Band-gap dependence of field emission from one-dimensional nanostructures grown on n-type and p-type silicon substrates, *Phys. Rev. B,* **68**, 125322 (2003).
143. K.R. Wang, S.J. Lin, L.W. Tu, M. Chen, and Q.Y. Chen, InN nanotips as excellent field emitters, *Appl. Phys. Lett.*, **92**, 123105 (2008).
144. X.H. Ji, S.P. Lau, H.Y. Yang, and S.F. Yu, Aligned InN nanofingers prepared by the ion-beam assisted filtered cathodic vacuum arc technique, *Nanotechnology*, **16**, 3069 (2005).
145. C.F. Shih, N.C. Chen, P.H. Chang, and K.S. Liu, Field emission properties of self-assembled InN nano-structures: Effect of Ga incorporation, *J. Cryst. Growth*, **281**, 328 (2005).
146. K.P. Adhi, S. Harchirkar, S.M. Jejurikar, P.M. Koinkar, M.A. More, D.S. Joag, and L.M. Kukreja, Pulsed laser deposited nanostructured InN thin films as field emitters, *Solid State Commun.*, **142**, 110 (2007).
147. S. Han, W. Jin, D. Zhang, T. Tang, C. Li, X. Liu, Z. Liu, B. Lei, and C. Zhou, Photoconduction studies on GaN nanowire transistors under UV and polarized UV illumination, *Chem. Phys. Lett.*, **389**, 176 (2004).
148. M. Kang, J.S. Lee, S.K. Sim, H. Kim, B. Min, K. Cho, G.T. Kim, M.Y. Sung, S. Kim, and H.S. Han, Photocurrent and photoluminescence characteristics of networked GaN nanowires, *Jpn. J. Appl. Phys.*, **43**, 6868 (2004).
149. C.H. Qiu and J.I. Pankove, Deep levels and persistent photoconductivity in GaN thin films, *Appl. Phys. Lett.*, **70**, 1983 (1997).
150. G. Beadie, W.S. Rabinovich, A.E. Wickden, D.D. Koleske, S.C. Binari, and J.A. Freitas, Jr., Persistent photoconductivity in n-type GaN, *Appl. Phys. Lett.*, **71**, 1092 (1997).
151. C. Johnson, J.Y. Lin, H.X. Jiang, M.A. Khan, and C.J. Sun, Metastability and persistent photoconductivity in Mg-doped p-type GaN, *Appl. Phys. Lett.*, **68**, 1808 (1996).
152. I. Ferguson, C.A. Tran, R.F. Karlicek, Jr., Z.C. Feng, R. Stall, S. Liang, Y. Lu, and C. Joseph, GaN and AlGaN metal-semiconductor-metal photodetectors, *Mater. Sci. Eng. B,* **50**, 311 (1997).
153. M. DeVittorio, G. Coli′, R. Rinaldi, G. Gigli, R. Cingolani, D. DeSalvador, M. Berti, A. Drigo, F. Fucilli, T. Ligonzo, V. Augelli, A. Rizzi, R. Lantier, D. Freundt, H. Luth, B. Neubauer, and D. Gerthsen, Photocurrent spectroscopy of GaN and AlGaN epilayers grown on 6H (0001) silicon carbide, *Solid State Electron.*, **44**, 465 (2000).
154. R. Calarco, M. Marso, T. Richter, A.I. Aykanat, R. Meijers, A.v.d. Hart, T. Stoica, and H. Luth, Size-dependent photoconductivity in MBE-grown GaN-nanowires, *Nano Lett.*, **5**, 981 (2005).
155. M. Kočan, A. Rizzi, H. Lüth, S. Keller, and U.K. Mishra, Surface potential at as-grown GaN(0001) MBE layers, *Phys. Status Solidi B*, **234**, 773 (2002).
156. A. Cavallini, L. Polenta, M. Rossi, T. Stoica, R. Calarco, R.J. Meijers, T. Richter, and H. Luth, Franz-Keldysh effect in GaN nanowires, *Nano Lett.*, **7**, 2166 (2007).
157. J.I. Pankove, *Optical Process in Semiconductors*, Dover, New York (1975).
158. W. Franz, Einfluss eines elektrischen feldes auf eine optische absorptionskante, *Zeitschrift Naturforschung Teil A*, **13**, 484 (1958).
159. L.V. Keldysh, The effect of a strong electric field on the optical properties of insulating crystals, *Sov. Phys. JETP*, **7**, 788 (1958).
160. E. Munoz, E. Monroy, J.A. Garrido, I. Izpura, F.J. Sanchez, M.A. Sanchez-Garcia, B. Beaumont, and P. Gibart, Photoconductor gain mechanisms in GaN ultraviolet detectors, *Appl. Phys. Lett.*, **71**, 870 (1997).
161. J.A. Garrido, E. Monroy, I. Izpura, and E. Munoz, Photoconductive gain modelling of GaN photoconductors, *Semicond. Sci. Technol.*, **13**, 563 (1998).
162. K.S. Stevens, M. Kinniburgh, and R. Beresford, Photoconductive ultraviolet sensor using Mg-doped GaN on Si (111), *Appl. Phys. Lett.*, **66**, 3518 (1995).
163. F. Binet, J.Y. Duboz, E. Rosencher, F. Scholz, and V. Harle, Mechanisms of recombination in GaN photodetectors, *Appl. Phys. Lett.*, **69**, 1202 (1996).
164. B. Shen, K. Yang, L. Zang, Z.Z. Chen, Y.G. Zhou, P. Chen, R. Zhang, Z.C. Huang, H.S. Zhou, and Y.D. Zheng, Study of photocurrent properties of GaN ultraviolet photoconductor grown on 6H-SiC substrate, *Jpn. J. Appl. Phys.*, **38**, 767 (1999).
165. R.S. Chen, H.Y. Chen, C.Y. Lu, K.H. Chen, C.P. Chen, L.C. Chen, and Y.J. Yang, Ultrahigh photocurrent gain in m-axial GaN nanowires, *Appl. Phys. Lett.*, **91**, 223106 (2007).
166. C. Soci, A. Zhang, B. Xiang, S.A. Dayeh, D.P.R. Aplin, J. Park, X.Y. Bao, Y.H. Lo, and D. Wang, ZnO nanowire UV photodetectors with high internal gain, *Nano Lett.*, **7**, 1003 (2007).
167. B.S. Simpkins, P.E. Pehrsson, and A.R. Laracuente, Electronic conduction in GaN nanowires, *Appl. Phys. Lett.*, **88**, 072111 (2006).
168. I. Mahboob, T.D. Veal, L.F.J. Piper, C.F. McConville, H. Lu, W.J. Schaff, J. Furthmuller, and F. Bechstedt, Origin of electron accumulation at wurtzite InN surfaces, *Phys. Rev. B,* **69**, 201307 (2004).
169. K.A. Rickert, A.B. Ellis, F.J. Himpsel, H. Lu, W.J. Schaff, J.M. Redwing, F. Dwikusuma, and T.F. Kuech, X-ray photoemission spectroscopic investigation of surface treatments, metal deposition, and electron accumulation on InN, *Appl. Phys. Lett.*, **82**, 3254 (2003).
170. T. Stoica, R.J. Meijers, R. Calarco, T. Richter, E. Sutter, and H. Lüth, Photoluminescence and intrinsic properties of MBE-grown InN nanowires, *Nano Lett.*, **6**, 1541 (2006).
171. T. Tang, S. Han, W. Jin, X. Liu, C. Li, D. Zhang, and C. Zhou, Synthesis and characterization of single-crystal indium nitride nanowires, *J. Mater. Res.*, **19**, 423 (2004).

172. C. Chao, H. Chang, T. Hsu, C. Hsiao, C. Kei, S. Kuo, and J. Chyi, Optical properties of indium nitride nanorods prepared by chemical-beam epitaxy, *Nanotechnology*, **17**, 3930 (2006).
173. J. Chen, G. Cheng, E. Stern, M.A. Reed, and P. Avouris, Electrically excited infrared emission from InN nanowire transistors, *Nano Lett.*, **7**, 2276 (2007).
174. S. Lee, W. Lee, K. Seo, J. Kim, S.H. Han, and B. Kim, Electronic transport mechanism and photocurrent generations of single-crystalline InN nanowires, *Nanotechnology*, **19**, 415202 (2008).
175. I. Yonenaga, A. Nikolaev, Y. Melnik, and V. Dmitriev, High-temperature hardness of bulk single-crystal AlN, *Jpn. J. Appl. Phys.*, **40**, L426 (2001).
176. H. Mehrez and S. Ciraci, Yielding and fracture mechanisms of nanowires, *Phys. Rev. B,* **56**, 12632 (1997).
177. H. Mehrez, S. Ciraci, C.Y. Fong, and S. Erkoc, An atomistic study on the stretching of nanowires, *J. Phys. Condens. Matter*, **9**, 10843 (1997).
178. K. Kim, W.R.L. Lambrecht, and B. Segall, Elastic constants and related properties of tetrahedrally bonded BN, AlN, GaN, and InN, *Phys. Rev. B,* **53**, 16310 (1996).
179. M.M. Treacy, T.W. Ebbesen, and J.M. Gibson, Exceptionally high Young's modulus observed for individual carbon nanotubes, *Nature*, **381**, 678 (1996).
180. Z.L. Wang, Characterizing the structure and properties of individual wire-like nanoentities, *Adv. Mater.*, **12**, 1295 (2000).
181. M. Yu, O. Lourie, M.J. Dyer, K. Moloni, T.F. Kelly, and R.S. Ruoff, Strength and breaking mechanism of multiwalled carbon nanotubes under tensile load, *Science*, **287**, 637 (2000).
182. E.W. Wong, P.E. Sheehan, and C.M. Lieber, Nanobeam mechanics: Elasticity, strength, and toughness of nanorods and nanotubes, *Science*, **277**, 1971 (1997).
183. M. Yu, T. Kowalewski, and R.S. Ruoff, Investigation of the radial deformability of individual carbon nanotubes under controlled indentation force, *Phys. Rev. Lett.*, **85**, 1456 (2000).
184. X. Li, H. Gao, C.J. Murphy, and K.K. Caswell, Nanoindentation of silver nanowires, *Nano Lett.*, **3**, 1495 (2003).
185. G. Feng, W.D. Nix, Y. Yoon, and C.J. Lee, A study of the mechanical properties of nanowires using nanoindentation, *J. Appl. Phys.*, **99**, 74304 (2006).
186. S. Nakamura and G. Fasol, *The Blue Laser Diodes*, Springer, Heidelberg (1997).
187. S. Nakamura, Applications of LEDs and LDs, in *GaN* (Gallium nitride), vol. 1, J.I. Pankove, and T.D. Moustakas, Eds., Academic, New York, 431 (1998).
188. S.C. Binari and H.C. Dietrich, III-V Nitride Electronic Devices, in *GaN and Related Materials*, S.J. Pearton, Ed., Gordon and Breach, New York, 509 (1997).
189. M.A. Khan, Q. Chen, J.W. Yang, and C.J. Sun, Electronics devices based on GaN-AlGaN material system, *Inst. Phys. Conf. Ser.*, **142**, 985 (1996).
190. M.S. Shur and M.A. Khan, GaN/AlGaN heterostructure devices: Photodetectors and field-effect transistors, *Mater. Res. Soc. Bull.*, **22**, 44 (1997).
191. J.Y. Duboz and M.A. Khan, Transistors and detectors based on GaN related materials, in *Group III Nitride Semiconductor Compounds*, B. Gil, Ed., Clarendon, Oxford, 343 (1998).
192. B. Gil, Ed., *Low Dimensional Nitride Semiconductors*, Oxford University Press, New York (2002).
193. Y.J. Kim, Y.S. Yang, S.C. Ha, S.M. Cho, Y.S. Kim, H.Y. Kim, H. Yang, and Y.T. Kim, Mixed-ligand nanoparticles of chlorobenzenemethanethiol and n-octanethiol as chemical sensors, *Sens. Actuators B,* **106**, 189 (2005).
194. A. Star, T.R. Han, V. Joshi, J.C. Gabriel, and G. Gruner, Nanoelectronic carbon dioxide sensors, *Adv. Mater.*, **16**, 2049 (2004).
195. H. Liu, J. Kameoka, D.A. Czaplewski, and H.G. Craighead, Polymeric nanowire chemical sensor, *Nano Lett.*, **4**, 671 (2004).
196. V. Dobrokhotov, D.N. Mcllroy, M.G. Norton, A. Abuzir, W.J. Yeh, I. Stevenson, R. Puoy, J. Bochenek, M. Cartwright, L. Wang, J. Dawson, M. Beaux, and C. Berven, Principles and mechanisms of gas sensing by GaN nanowires functionalized with gold nanoparticles, *J. Appl. Phys.*, **99**, 104302 (2006).
197. L. Voss, B.P. Gila, S.J. Pearton, H.T. Wang, and F. Ren, Characterization of bulk GaN rectifiers for hydrogen gas sensing, *J. Vac. Sci. Technol. B*, **23**, 2373 (2005).
198. F. Yun, S. Chevtchenko, Y.T. Moon, H. Morkoc, T.J. Fawcett, and J.T. Wolan, GaN resistive hydrogen gas sensors, *Appl. Phys. Lett.*, **87**, 073507 (2005).
199. W. Lim, J.S. Wright, B.P. Gila, J.L. Johnson, A. Ural, T. Anderson, F. Ren, and S.J. Pearton, Room temperature hydrogen detection using Pd-coated GaN nanowires, *Appl. Phys. Lett.*, **93**, 072109 (2008).
200. H.T. Wang, B.S. Kang, F. Ren, L.C. Tien, P.W. Sadik, D.P. Norton, S.J. Pearton, and J. Lin, Hydrogen-selective sensing at room temperature with ZnO nanorods, *Appl. Phys. Lett.*, **86**, 243503 (2005).
201. G. Steinhoff, M. Hermann, W.J. Schaff, L.F. Eastman, M. Stutzman, and M. Eickhoff, pH response of GaN surfaces and its application for pH-sensitive field-effect transistors, *Appl. Phys. Lett.*, **83**, 177 (2003).
202. H. Lu, W.J. Schaff, and L.F. Eastman, Surface chemical modification of InN for sensor applications, *J. Appl. Phys.*, **96**, 3577 (2004).
203. O. Kryliouk, H.J. Park, H.T. Wang, B.S. Kang, T.J. Anderson, F. Ren, and S.J. Pearton, Pt-coated InN nanorods for selective detection of hydrogen at room temperature, *J. Vac. Sci. Technol. B,* **23**, 1891 (2005).
204. K.D. Mitzner, J. Sternhagen, and D.W. Galipeau, Development of a micromachined hazardous gas sensor array, *Sens. Actuators B*, **93**, 92 (2003).
205. H.L. Hartnagel, A.L. Dawar, A.K. Jain, and C. Jagadish, *Semiconducting Transparent Thin Films*, IOP, Bristol (1995).
206. J.F. Chang, H.H. Kuo, I.C. Leu, and M.H. Hon, The effects of thickness and operation temperature on ZnO:Al thin film CO gas sensor *Sens. Actuators B*, **84**, 258 (2002).
207. W. Lim, J.S. Wright, B.P. Gila, S.J. Pearton, F. Ren, W.T. Lai, L.C. Chen, and K.H. Chen, Selective-hydrogen sensing at room temperature with Pt-coated InN nanobelts, *Appl. Phys. Lett.*, **93**, 202109 (2008).
208. J.S. Wright, W. Lim, B.P. Gila, S.J. Pearton, F. Ren, W.T. Lai, L.C. Chen, M.S. Hu, and K.H. Chen, Pd-catalyzed hydrogen sensing with InN nanobelts, *J. Vac. Sci. Technol. B,***27**, L8 (2009).
209. P. Alivisatos, The use of nanocrystals in biological detection, *Nature Biotechnol.*, **22**, 47 (2004).
210. E. Katz and I. Willner, Integrated nanoparticle-biomolecule hybrid systems: Synthesis, properties, and applications, *Angew. Chem. Int. Ed.*, **43**, 6042 (2004).

211. E. Katz and I. Willner, Probing biomolecular interactions at conductive and semiconductive surfaces by impedance spectroscopy: Routes to impedimetric immunosensors, DNA-Sensors, and enzyme biosensors, *Electroanalysis*, **15**, 913 (2003).
212. Y. Cui, Q. Wei, H. Park, and C.M. Lieber, Nanowire nanosensors for highly sensitive and selective detection of biological and chemical species, *Science*, **293**, 1289 (2001).
213. M. Uhlen, Magnetic separation of DNA, *Nature*, **340**, 733 (1989).
214. R. Mahtab, J.P. Rogers, and C.J. Murphy, Protein-sized quantum-dot luminescence can distinguish between straight, bent, and kinked oligonucleotides, *J. Am. Chem. Soc.*, **117**, 9099 (1995).
215. R. Elghanian, J.J. Storhoff, R.C. Mucic, R.L. Letsinger, and C.A. Mirkin, Selective colorimetric detection of polynucleotides based on the distance-dependent optical properties of gold nanoparticles, *Science*, **277**, 1078 (1997).
216. M. Jr. Bruchez, M. Moronne, P. Gin, S. Weiss, and A.P. Alivisatos, Semiconductor nanocrystals as fluorescent biological labels, *Science*, **281**, 2013 (1998).
217. W.C.W. Chan and S. Nie, Quantum dot bioconjugates for ultrasensitive nonisotopic detection, *Science*, **281**, 2016 (1998).
218. C.V. Nguyen, L. Delzeit, A.M. Cassell, J. Li, J. Han, and M. Meyyappan, Preparation of nucleic acid functionalized carbon nanotube Arrays, *Nano Lett.*, **2**, 1079 (2002).
219. D.S. Grubisha, R.J. Lipert, H.Y. Park, J. Driskell, and M.D. Porter, Femtomolar detection of prostate-specific antigen: An immunoassay based on surface-enhanced Raman scattering and immunogold labels, *Anal. Chem.*, **75**, 5936 (2003).
220. F. Patolsky, Y. Weizmann, E. Katz, and I. Willner, Magnetically amplified DNA assays (MADA): Sensing of viral DNA and single-base mismatches by using nucleic acid modified magnetic particles, *Angew. Chem. Int. Ed.*, **42**, 2372 (2003).
221. S. Chattopadhyay, H.C. Lo, C.H. Hsu, L.C. Chen, and K.H. Chen, Surface-enhanced Raman spectroscopy using self-assembled silver nanoparticles on silicon nanotips, *Chem. Mater.*, **17**, 553 (2005).
222. G. Steinhoff, O. Purrucker, M. Tanaka, M. Stutzmann, and M. Eickhoff, $Al_xGa_{1-x}N$- A new material system for biosensors, *Adv. Funct. Mater.*, **13**, 841 (2003).
223. T.H. Young and C.R. Chen, Assessment of GaN chips for culturing cerebellar granule neurons, *Biomaterials*, **27**, 3361 (2006).
224. M. Stutzmann, J.A. Garrido, M. Eickhoff, and M.S. Brandt, Direct biofunctionalization of semiconductors: A survey, *Phys. Status Solidi A*, **203**, 3424 (2006).
225. B.S. Kang, H.T. Wang, F. Ren, and S.J. Pearton, Electrical detection of biomaterials using AlGaN/GaN high electron mobility transistors, *J. Appl. Phys.*, **104**, 031101 (2008).
226. N. Chaniotakis and N. Sofikiti, Novel semiconductor materials for the development of chemical sensors and biosensors: A review, *Anal. Chim. Acta*, **615**, 1 (2008).
227. S.J. Pearton, B.S. Kang, S. Kim, F. Ren, B.P. Gila, C.R. Abernathy, J. Lin, and S.N.G. Chu, GaN-based diodes and transistors for chemical, gas, biological and pressure sensing, *J. Phys. Condens. Matter*, **16**, R961 (2004).
228. B. Baur, J. Howgate, H.G. von Ribbeck, Y. Gawlina, V. Bandalo, G. Steinhoff, M. Stutzmann, and M. Eickhoff, Catalytic activity of enzymes immobilized on AlGaN/GaN solution gate field-effect transistors, *Appl. Phys. Lett.*, **89**, 183901 (2006).
229. B.S. Kang, F. Ren, L. Wang, C. Lofton, W.W. Tan, S.J. Pearton, A. Dabiran, A. Osinsky, and P.P. Chow, Electrical detection of immobilized proteins with ungated AlGaN/GaN high-electron-mobility transistors, *Appl. Phys. Lett.*, **87**, 023508 (2005).
230. B.S. Kang, S.J. Pearton, J.J. Chen, F. Ren, J.W. Johnson, R.J. Therrien, P. Rajagopal, J.C. Roberts, E.L. Piner, and K.J. Linthicum, Electrical detection of deoxyribonucleic acid hybridization with AlGaN/GaN high electron mobility transistors, *Appl. Phys. Lett.*, **89**, 122102 (2006).
231. B.S. Kang, H.T. Wang, T.P. Lele, Y. Tseng, F. Ren, S.J. Pearton, J.W. Johnson, P. Rajagopal, J.C. Roberts, E.L. Piner, and K.J. Linthicum, Prostate specific antigen detection using AlGaN/GaN high electron mobility transistors, *Appl. Phys. Lett.*, **91**, 112106 (2007).
232. H.T. Wang, B.S. Kang, F. Ren, S.J. Pearton, J.W. Johnson, P. Rajagopal, J.C. Roberts, E.L. Piner, and K.J. Linthicum, Electrical detection of kidney injury molecule-1 with AlGaN/GaN high electron mobility transistors, *Appl. Phys. Lett.*, **91**, 222101 (2007).
233. K. Tonisch, V. Cimalla, F. Will, F. Weise, M. Stubenrauch, A. Albrecht, M. Hoffmann, and O. Ambacher, Nanowire-based electromechanical biomimetic sensor, *Physica*, *E* **37**, 208 (2007).
234. B.S. Kang, H.T. Wang, F. Ren, S.J. Pearton, T.E. Morey, D.M. Dennis, J.W. Johnson, P. Rajagopal, J.C. Roberts, E.L. Piner, and K.J. Linthicum, Enzymatic glucose detection using ZnO nanorods on the gate region of AlGaN/GaN high electron mobility transistors, *Appl. Phys. Lett.*, **91**, 252103 (2007).
235. B.H. Chu, B.S. Kang, F. Ren, C.Y. Chang, Y.L. Wang, S.J. Pearton, A.V. Glushakov, D.M. Dennis, J.W. Johnson, P. Rajagopal, J.C. Roberts, E. L. Piner, and K.J. Linthicum, Enzyme-based lactic acid detection using AlGaN/GaN high electron mobility transistors with ZnO nanorods grown on the gate region, *Appl. Phys. Lett.*, **93**, 042114 (2008).
236. B.S. Simpkins, K.M. McCoy, L.J. Whitman, and P.E. Pehrsson, Fabrication and characterization of DNA-functionalized GaN nanowires, *Nanotechnology*, **18**, 355301 (2007).
237. C.P. Chen, A. Ganguly, C.H. Wang, C.W. Hsu, S. Chattopadhyay, Y.K. Hsu, Y.C. Chang, K.H. Chen, and L.C. Chen, Label-Free Dual Sensing of DNA Molecules Using GaN Nanowires, *Anal. Chem.*, **81**, 36 (2009).
238. A. Ganguly, C.P. Chen, Y.T. Lai, C.C. Kuo, C.W. Hsu, K.H. Chen, and L.C. Chen, Functionalized GaN nanowire-based electrode for direct label-free voltammetric detection of DNA hybridization, *J. Mater. Chem.*, **19**, 928 (2009).
239. T. Yano, D.A. Tryk, K. Hashimoto, and A. Fujishima, Electrochemical behavior of highly conductive boron-doped diamond electrodes for oxygen reduction in alkaline solution, *J. Electrochem. Soc.*, **145**, 1870 (1998).
240. M.C. Granger, M. Witek, J. Xu, J. Wang, M. Hupert, A. Hanks, M.D. Koppang, J.E. Butler, G. Lucazeau, M. Mermoux, J.W. Strojek, and G.M. Swain, Standard electrochemical behavior of high-quality, boron-doped polycrystalline diamond thin-film electrodes, *Anal. Chem.*, **72**, 3793 (2000).
241. W.C. Poh, K.P. Loh, W.D. Zhang, S. Triparthy, J.S. Ye, and F.S. Sheu, Biosensing properties of diamond and carbon nanotubes, *Langmuir*, **20**, 5484 (2004).
242. C. Prado, G.U. Flechsig, P. Grundler, J.S. Foord, F. Marken, and R.G. Compton, Electrochemical analysis of nucleic acids at boron-doped diamond electrodes, *Analyst*, **127**, 329 (2002).
243. T.A. Ivandini, B.V. Sarada, T.N. Rao, and A. Fujishima, Electrochemical oxidation of underivatized-nucleic acids at

highly boron-doped diamond electrodes, *Analyst*, **128**, 924 (2003).
244. Y. Takagaki, P.V. Santos, E.Wiebicke, O. Brandt, H.P. Schönherr, and K. H. Ploog, Superhigh-frequency surface-acoustic-wave transducers using AlN layers grown on SiC substrates, *Appl. Phys. Lett.*, **81**, 2538 (2002).
245. C. Caliendo and P. Imperatori, High-frequency, high-sensitivity acoustic sensor implemented on AlN/Si substrate, *Appl. Phys. Lett.*, **83**, 1641 (2003).
246. J. Xu, J.S. Thakur, F. Zhong, H. Ying, and G.W. Auner, Propagation of a shear-horizontal surface acoustic mode in a periodically grooved $AlN/Al_2O_3$ microstructure, *J. Appl. Phys.*, **96**, 212 (2004).
247. C.S. Chiu and S. Gwo, Quantitative surface acoustic wave detection based on colloidal gold nanoparticles and their bioconjugates, *Anal. Chem.*, **80**, 3318 (2008).
248. C.S. Chiu, H.M. Lee, C.T. Kuo, and S. Gwo, Immobilization of DNA-Au nanoparticles on aminosilane-functionalized aluminum nitride epitaxial films for surface acoustic wave sensing, *Appl. Phys. Lett.*, **93**, 163106 (2008).
249. S. Chattopadhyay, S.C. Shi, Z.H. Lan, C.F. Chen, K.H. Chen, and L.C. Chen, Molecular sensing with ultrafine silver crystals on hexagonal aluminum nitride nanorod templates, *J. Am. Chem. Soc.*, **127**, 2820 (2005).
250. X. Duan, Y. Huang, Y. Cui, J. Wang, and C.M. Lieber, Indium phosphide nanowires as building blocks for nanoscale electronic and optoelectronic devices, *Nature*, **409**, 66 (2001).
251. Y. Huang, X. Duan, and C.M. Lieber, Nanowires for integrated multicolor nanophotonics, *Small*, **1**, 142 (2005).
252. H.M. Kim, Y.H. Cho, H. Lee, S.I. Kim, S.R. Ryu, D.Y. Kim, T.W. Kang, and K.S. Chung, High-brightness light emitting diodes using dislocation-free indium gallium nitride/gallium nitride multiquantum-well nanorod arrays, *Nano Lett.*, **4**, 1059 (2004).
253. H.J. Chang, Y.P. Hsieh, T.T. Chen, Y.F. Chen, C.T. Liang, T.Y. Lin, S.C. Tseng, L.C. Chen, Strong luminescence from strain relaxed InGaN/GaN nanotips for highly efficient light emitters, *Opt. Express*, **15**, 9357 (2007).
254. S. Nakamura, S. Pearton, and G. Fasol, *The Blue Laser Diode: The Complete Story*, Springer-Verlag, Berlin (2000).
255. T. Mukai, Recent progress in group-III nitride light-emitting diodes, *IEEE J. Sel. Top. Quantum Electron.*, **8**, 264 (2002).
256. R.S. Chen, S.W. Wang, Z.H. Lan, J.T.H. Tsai, C.T. Wu, L.C. Chen, K.H. Chen, Y.S. Huang, and C.C. Chen, On-chip fabrication of well-aligned and contact-barrier-free GaN nanobridge devices with ultrahigh photocurrent responsivity, *Small*, **4**, 925 (2008).
257. K. Haraguchi, K. Hiruma, T. Katsuyama, K. Tominaga, M. Shirai, and T. Shimada, Self-organized fabrication of planar GaAs nanowhisker arrays, *Appl. Phys. Lett.*, **69**, 386 (1996).
258. K. Kim, T. Henry, G. Cui, J. Han, Y.K. Song, A.V. Nurmikko, and H. Tang, Epitaxial growth of aligned GaN nanowires and nanobridges, *Phys. Status Solidi B*, **244**, 1810 (2007).
259. T. Henry, K. Kim, Z. Ren, C. Yerino, J. Han, and H.X. Tang, Directed growth of horizontally aligned gallium nitride nanowires for nanoelectromechanical resonator Arrays, *Nano Lett.*, **7**, 3315 (2007).
260. M.A. Khan, J.N. Kuznia, D.T. Olson, J.M. Van Hove, M. Blasingame, and L.F. Reitz, High-responsivity photoconductive ultraviolet sensors based on insulating single-crystal GaN epilayers, *Appl. Phys. Lett.*, **60**, 2917 (1992).
261. D. Walker, X. Zhang, P. Kung, A. Saxler, S. Javadpour, J. Xu, and M. Razeghi, AlGaN ultraviolet photoconductors grown on sapphire, *Appl. Phys. Lett.*, **68**, 2100 (1996).
262. B.W. Lim, Q.C. Chen, J.Y. Yang, and M.A. Khan, High responsitivity intrinsic photoconductors based on $Al_xGa_{1-x}N$, *Appl. Phys. Lett.*, **68**, 3761 (1996).
263. C. Pernot, A. Hirano, M. Iwaya, T. Detchprohm, H. Amano, and I. Akasaki, Low-intensity ultraviolet photodetectors based on AlGaN, *Jpn. J. Appl. Phys.*, **38**, L487 (1999).
264. P. Bhattacharya, *Semiconductor Optoelectronic Devices*, Prentice-Hall, New Jersey, USA, chap. 8, 346 (1997).
265. Z.M. Zhao, R.L. Jiang, P. Chen, D.J. Xi, Z.Y. Luo, R. Zhang, B. Shen, Z.Z. Chen, and Y.D. Zheng, Metal-semiconductor-metal GaN ultraviolet photodetectors on Si(111), *Appl. Phys. Lett.*, **77**, 444 (2000).
266. Z.C. Huang, D.B. Mott, P.K. Shu, R. Zhang, J.C. Chen, and D.K. Wickenden, Optical quenching of photoconductivity in GaN photoconductors, *J. Appl. Phys.*, **82**, 2707 (1997).
267. H. Wu, Y. Sun, D. Lin, R. Zhang, C. Zhang, and W. Pan, GaN nanofibers based on electrospinning: Facile synthesis, controlled assembly, precise doping, and application as high performance UV photodetector, *Adv. Mater.*, **21**, 227 (2009).
268. A.B.F. Martinson, J.W. Elam, J.T. Hupp, and M.J. Pellin, ZnO nanotube based dye-sensitized solar cells ZnO nanotube based dye-sensitized solar cells, *Nano Lett.*, **7**, 2183 (2007).
269. C.Y. Jiang, X.W. Sun, G.Q. Lo, D.L. Kwong, and J.X. Wang, Improved dye-sensitized solar cells with a ZnO-nanoflower photoanode, *Appl. Phys. Lett.*, **90**, 263501 (2007).
270. L.E. Greene, M. Law, B.D. Yuhas, and P. Yang, $ZnO\text{-}TiO_2$ core-shell nanorod/P3HT solar cells, *J. Phys. Chem. C*, **111**, 18451 (2007).
271. Y.B. Tang, Z.H. Chen, H.S. Song, C.S. Lee, H.T. Cong, H.M. Cheng, W.J. Zhang, I. Bello, and S.T. Lee, Vertically aligned p-type single-crystalline GaN nanorod arrays on n-type Si for heterojunction photovoltaic cells, *Nano Lett.*, **8**, 4191 (2008).